

UNIVERSITY OF CALGARY

Development of 3D MOF Nanocomposites with Semiconducting Behavior for Resistive Gas  
Sensors and Photodetectors Applications

by

Setareh Homayoonnia

A THESIS

SUBMITTED TO THE FACULTY OF GRADUATE STUDIES  
IN PARTIAL FULFILMENT OF THE REQUIREMENTS FOR THE  
DEGREE OF DOCTOR OF PHILOSOPHY

GRADUATE PROGRAM IN MECHANICAL AND MANUFACTURING ENGINEERING

CALGARY, ALBERTA

DECEMBER, 2023

© Setareh Homayoonnia 2023

## Abstract

This thesis presents a comprehensive exploration of three distinct projects involving novel nanocomposites consisting of metal-organic frameworks (MOFs) combined with multiwall carbon nanotubes (MWCNTs) and carbon nanofibers (CNFs). These projects encompass methane ( $\text{CH}_4$ ) detection, the application of MOF composites for diabetes diagnosis through acetone detection, and their utilization as advanced photodetectors.

In the first project, addressing the critical issue of  $\text{CH}_4$  detection, an innovative MOF/MWCNTs-based resistive sensor was developed.  $\text{CH}_4$  detection is crucial due to its environmental and safety implications. Existing detection methods often struggle with low concentrations of  $\text{CH}_4$  at room temperature (RT), typically within the range of a few parts per million (ppm). The developed sensor offers cost-efficiency, reliability, high sensitivity, and selectivity, presenting a breakthrough technology with the potential to significantly enhance environmental monitoring and industrial safety.

The second project focuses on diabetes management, a global health concern. Traditional invasive blood glucose measurements can be cumbersome. To simplify and improve diabetes monitoring, the research investigates non-invasive nanomaterial-based gas sensors for detecting acetone, a diabetes biomarker. The developed MOF/MWCNTs nanocomposite resistive sensor offers selective detection of acetone at RT and atmospheric pressure, exhibiting remarkable sensitivity. The limit of detection is three orders of magnitude lower than the concentration of acetone in the exhaled breath of diabetic patients.

The third project explores the application of MOF/CNF nanocomposites in photodetectors, crucial components in various technological domains. Traditional photodetectors face limitations, such as broadband absorption and the need for costly optical filters in narrowband applications.

The introduced MOF/CNF nanocomposites address these challenges, combining the strengths of MOFs and CNFs while mitigating their weaknesses. This research not only overcomes limitations in traditional and recent nanomaterials-based photodetectors but also extends the capabilities of three-dimensional (3D) MOFs in narrowband photodetection applications, potentially revolutionizing photodetection technology.

Overall, this thesis explores the potential of MOF-based nanocomposites in addressing critical challenges in CH<sub>4</sub> detection, diabetes management, and photodetection, holding promise for environmental preservation, healthcare, and technological advancements.

## Preface

This thesis is an original work by the author. Chapter 3, 4 and 5 of this thesis has been based on peer-reviewed: ACS Sensor, and Sensors and Actuators B: Chemical articles, for which I have been the first author. Chapter 6 is based on a manuscript under preparation. All chapters of this thesis are based on the following peer reviewed publications:

- **S. Homayoonnia**, A. Phani, S. Kim, MOF/MWCNTs-Nanocomposite Manipulates High Selectivity to Gas via Different Adsorption-Sites with Varying Electron Affinity: A Study in Methane Detection in Parts-Per-Billion, ACS sensor, 7 (2022) 3846-3856.
- **S. Homayoonnia**, S. Kim, ZIF-8/MWCNT-Nanocomposite Based-Resistive Sensor for Highly Selective Detection of Acetone in Parts-Per-Billion: Potential Noninvasive Diagnosis of Diabetes, Sensors and Actuators B: Chemical, 393 (2023) 134197.
- **S. Homayoonnia**, S. Kim, Eco-friendly and High-Performance Photodetector based on Bandgap-Engineered MOFs/CNFs Nanocomposites for Violet Light Detection, Advanced Optical Materials, Submitted.

## **Acknowledgments**

In the culmination of this academic journey, I stand humbled and profoundly grateful for the invaluable support, encouragement, and guidance that have carried me to this moment. I extend my heartfelt thanks to all those who have been instrumental in this endeavor.

First and foremost, I extend my heartfelt appreciation to my esteemed supervisor, Dr. Sam Kim, whose unwavering support, expert guidance, and mentorship have been instrumental throughout my research. Your dedication to excellence and your belief in my potential have been a constant source of inspiration.

I am profoundly thankful to my committee members for their valuable insights, feedback, and contributions to the refinement of this work. Your expertise has enriched the quality of this thesis, and I am grateful for your time and commitment.

I want to dedicate this work to my late father. Losing you was a profound loss that words cannot adequately express. Your wisdom, love, and unwavering support have been a constant source of inspiration throughout my life. I know you would have been immensely proud of this achievement.

To my mother, who has not only been my teacher but also my eternal source of wisdom and strength, I owe an immeasurable debt of gratitude. Her endless patience, profound knowledge, and unwavering support have been the bedrock of my educational journey.

To my loving husband, your patience, understanding, and unwavering belief in me have been my pillars of strength. Your belief in me never wavered, and I am grateful to have you by my side.

My heartfelt thanks go to my sisters and brother, your encouragement and belief in my abilities have been a source of motivation. Thank you for always cheering me on and being there when I needed you.

To all my friends, and colleagues who have contributed to my academic and personal growth, thank you for your friendship, encouragement, and inspiration.

Last but not least, I want to express my gratitude to the countless individuals who have played a role, no matter how small, in this academic endeavor.

This thesis stands as a testament to the collective support, encouragement, and belief in my abilities. It is a reflection of the love and guidance that have illuminated my path. Thank you all for being a part of this remarkable journey.

## Table of Contents

<b>Abstract</b> .....	ii
<b>Preface</b> .....	iv
<b>Acknowledgments</b> .....	v
<b>List of Figures</b> .....	xi
<b>List of Tables</b> .....	xvii
<b>List of Symbols &amp; Abbreviations</b> .....	xviii
<b>Chapter 1 : Introduction</b> .....	1
<b>1.1 Research Background</b> .....	1
<b>1.2 Goal and Objectives</b> .....	11
<b>1.3 Thesis Overview</b> .....	13
<b>Chapter 2 : Literature Review</b> .....	14
<b>2.1 Nanomaterials for Detection of Methane</b> .....	14
<b>2.2 Nanomaterials for Detection of Acetone for Diabetes</b> .....	18
<b>2.3 Nanomaterials for Photodetection</b> .....	22
<b>2.4 Synthesis Strategies</b> .....	25
<b>2.4.1 MOFs Nanoparticles Synthesis Strategies</b> .....	25
<b>2.4.2 MOFs/MWCNTs and MOF/CNFs Nanocomposites Fabrication Strategies</b> .....	26
<b>2.5 MOFs Thin Film Fabrication Methods</b> .....	28

2.6 MOF-based Chemiresistive Sensors for Methane and Acetone Detection and their Mechanism .....	30
2.7 Light Detection Mechanisms in Photodetectors .....	31
2.7.1 Types of Photoconductivity.....	34
<b>Chapter 3 : Experimental Method .....</b>	<b>37</b>
<b>3.1 Material Synthesis .....</b>	<b>37</b>
3.1.1 Synthesis of ZIF-8.....	37
3.1.2 Synthesis of ZIF-8/MWCNTs Nanocomposites .....	38
3.1.3 Synthesis of ZIF-8/CNFs Nanocomposites .....	38
<b>3.2 Materials Characterization .....</b>	<b>39</b>
3.2.1 ZIF-8/MWCNTs Characterization .....	40
3.2.2 ZIF-8/CNFs Characterization .....	50
<b>3.3 Thin Film Fabrication.....</b>	<b>56</b>
<b>3.4 Experimental Test Setup .....</b>	<b>57</b>
3.4.1 IDE and QCM Based Gas Sensor Test Setup and Sensing Experiment: .....	57
3.4.2 Photodetector Test Setup and Sensing Experiment:.....	61
<b>Chapter 4 : Application of ZIF-8/MWCNTs as a Resistive Based Sensor for CH<sub>4</sub> Detection .....</b>	<b>62</b>
<b>4.1 Introduction.....</b>	<b>62</b>
<b>4.2 Results and Discussion .....</b>	<b>66</b>

<b>4.2.1 Structural and Morphological Characterization of ZIF-8, MWCNTs and ZIF-8/MWCNTs Nanocomposite</b> .....	66
<b>4.2.2 Sensor Performance Evaluation:</b> .....	70
<b>4.2.3 Response Mechanism Based on Structural and Electrical Properties of ZIF-8 and MWCNTs:</b> .....	82
<b>4.3 Conclusions</b> .....	85
<b>Chapter 5 : Application of ZIF-8/MWCNTs for Detection of VOCs Based QCM Sensor and as a Resistive Based Sensor for Detection of Acetone</b> .....	87
<b>5.1 Introduction</b> .....	87
<b>5.2 Results and Discussion</b> .....	90
<b>5.2.1 Characterization of ZIF-8, MWCNTs and ZIF-8/MWCNT Nanocomposite</b> .....	90
<b>5.2.2 Sensor Performance Evaluation</b> .....	91
<b>5.2.3 Sensing Mechanisms</b> .....	97
<b>5.3 Conclusions</b> .....	101
<b>Chapter 6 : Application of ZIF-8/CNFs Nanocomposite as a Spectrally Selective Photodetector</b> .....	103
<b>6.1 Introduction</b> .....	103
<b>6.2 Results and Discussion</b> .....	107
<b>6.2.1 Structural and Morphological Characterization of the ZIF-8, CNFs, and ZIF-8/CNFs Nanocomposite:</b> .....	107

<b>6.2.2 Sensor Performance Evaluation:</b> .....	108
<b>6.3 Conclusions</b> .....	114
<b>Chapter 7 : Conclusions and Further Works</b> .....	116
<b>7.1 Conclusions</b> .....	116
<b>7.2 Future Works</b> .....	118
<b>Appendix A: List of publications</b> .....	121
<b>Appendix B: Reuse Permission Letters</b> .....	123
<b>References</b> .....	135

## List of Figures

<b>Figure 2.1</b> Sensing based on different properties of MOFs (reproduced with permission from ref [139], Copyright (2023) Royal Society of Chemistry).....	31
<b>Figure 2.2</b> Schematic illustrations of a typical (a) photoconductor, (b) photodiode, and (c) phototransistor (reproduced with permission from ref [207], Copyright (2023) Royal Society of Chemistry).....	32
<b>Figure 2.3</b> Transition level in intrinsic and extrinsic photoconductivity process (reproduced with permission from ref [210], Copyright (2023) Elsevier Books).....	35
<b>Figure 3.1</b> FT-IR spectra of MWCNTs (black), ZIF-8 (green) and ZIF-8/MWCNTs nanocomposite (orange) in the wavenumber range of 4000–400 $\text{cm}^{-1}$ with a spectral resolution of 4 $\text{cm}^{-1}$ . .....	41
<b>Figure 3.2</b> Raman spectra of MWCNTs (black), ZIF-8 (green) and ZIF-8/MWCNTs nanocomposite (orange) in the wavenumber range of 1600 to 180 $\text{cm}^{-1}$ . .....	43
<b>Figure 3.3</b> XRD patterns of MWCNTs (black), ZIF-8 (green) and ZIF-8/MWCNTs nanocomposite (orange).....	44
<b>Figure 3.4</b> UV–Vis absorption spectra of MWCNTs (black), ZIF-8 (green) and ZIF-8/MWCNTs nanocomposite (orange).....	45
<b>Figure 3.5</b> Nitrogen adsorption and desorption isotherms at 77 K for (a) ZIF-8 and (b) ZIF-8/MWCNT nanocomposite.....	47
<b>Figure 3.6</b> a) FE-SEM image of ZIF-8 film with particle sizes ~50 nm. b) Medium magnification, and c) high magnification FE-SEM images of ZIF-8/MWCNTs film. ....	48
<b>Figure 3.7</b> EDX spectrum of ZIF-8/MWCNTs film on the surface of a silicon wafer with platinum coating: elements of carbons (C), nitrogen (N), oxygen (O), Zinc (Zn), silicon (Si) and platinum	

(Pt) come from ZIF-8's Hmim ligands and MWCNTs, ZIF-8's Hmim ligands, ZIF-8's metal node, the silicon wafer as substrate, and platinum coating on the surface of ZIF-8/MWCNTs, respectively. .... 48

**Figure 3.8** TEM analysis of the MWCNTs shows the layered structure. For the location shown here, the number of layers measured are 45 that accounts for a mean diameter of 28.8 nm with the distance between 2 layers in the order of ~0.64 nm. For different MWCNTs at different locations higher resolution imaging shows the lattice planes. Autocorrelation function (ACF) analysis of the lattice-plane structure reveals the mixed metallic and non-metallic nature of the MWCNTs as highlighted in the vector lengths in arbitrary units (au) (insets). .... 50

**Figure 3.9** FT-IR spectra of CNFs (black), ZIF-8 (red) and ZIF-8/CNFs nanocomposite (blue), respectively. .... 51

**Figure 3.10** XRD patterns of CNFs (black), ZIF-8 (red) and ZIF-8/CNFs nanocomposite (blue), respectively. .... 52

**Figure 3.11** UV–Vis absorption spectra of CNFs (black), ZIF-8 (red) and ZIF-8/CNFs nanocomposite (blue), respectively. .... 54

**Figure 3.12 a)** Medium magnification, and **b)** high magnification FE-SEM images of ZIF-8/CNFs film. .... 55

**Figure 3.13** EDX spectrum of ZIF-8/CNFs film on the surface of a silicon wafer with platinum coating: elements of carbons (C), nitrogen (N), oxygen (O), Zinc (Zn), silicon (Si) and gold (Au) come from ZIF-8's Hmim ligands and CNFs, ZIF-8's Hmim ligands, ZIF-8's metal node, the silicon wafer as substrate, and gold coating on the surface of ZIF-8/CNFs, respectively. .... 55

**Figure 3.14** Schematics of the spray-coating set-up with a dual action airbrush, an IDE, and QCM chips. .... 57

<b>Figure 3.15</b> Picture of the in-house fabricated flow chamber with electrode interface. ....	58
<b>Figure 3.16</b> Experimental setup for gas/vapour sensing experiments. ....	59
<b>Figure 4.1 a)</b> Schematic illustration of the material preparation process of the ZIF-8/MWCNTs nanocomposite and its spray-coated thin film on the surface of an IDE chip. <b>b)</b> Zeta Optical profilometer is used to measure thickness of the ZIF-8/MWCNTs film (~8 $\mu\text{m}$ thick) and to inspect the uniformity of the spray-coated film. ....	67
<b>Figure 4.2 a)</b> Tauc's plots for the band gap energy determination of MWCNTs (black), ZIF-8 (green) and ZIF-8/MWCNTs nanocomposite (orange), respectively. <b>b)</b> Schematic illustration of the band diagram for a visual representation of band gaps ( $E_g$ ), Fermi level ( $EF$ ), activation energy ( $\Delta E$ ) and acceptor level ( $E_a$ ) in intrinsic (ZIF-8) and p-type semiconductive bare MWCNTs and ZIF-8/MWCNTs nanocomposite. The synergic effect of compositing MWCNTs with ZIF-8 is evident in the lowering of the band gap and activation energy in the nanocomposite. ....	70
<b>Figure 4.3</b> Schematic illustration of $\text{CH}_4$ , $\text{CO}_2$ , alcohols vapours and $\text{H}_2\text{O}$ molecules physisorption into the pores and surfaces of ZIF-8 via electron accepting from or donating to ZIF-8/MWCNTs layer and the net exchanged electrons ( $\Delta e^-$ ) from the sensing layer to them, respectively. ....	71
<b>Figure 4.4</b> The sensor responses by exposing to desired $\text{CH}_4$ concentrations (1.5 - 100 ppm) at the total flow rate of 200 sccm until sensor response reached steady state. ....	72
<b>Figure 4.5</b> The dynamic response/recovery signals of the sensor with 5wt% MWCNTs for $\text{CH}_4$ at total flow rate of 200 sccm: As it is evident our sensor shows good response in this range of concentrations, even as low concentration of 1.5 ppm. ....	73
<b>Figure 4.6 a)</b> The sensor's comparative responses to 100 ppm of $\text{CH}_4$ , 100 ppm of $\text{CO}_2$ , 5060 ppm of IPA, 6843 ppm of ethanol, and 14803 ppm of methanol at a total flow rate of 200 sccm. <b>b)</b> Selectivity tests of the sensor toward 100 ppm $\text{CH}_4$ in a mixture in presence of 100 ppm of $\text{CO}_2$ ,	

5060 ppm of IPA, 6843 ppm of ethanol, 14803 ppm of methanol and 24327 ppm of water vapour at a total flow rate of 200 sccm, respectively. **c)** The sensor's comparative responses to 10 ppm of CH<sub>4</sub>, CO, NO<sub>2</sub>, NH<sub>3</sub>, benzene, toluene at a total flow rate of 200 sccm. **d)** Selectivity tests of the sensor toward 10 ppm of CH<sub>4</sub> in a mixture in presence of 10 ppm of CO, NO<sub>2</sub>, NH<sub>3</sub>, benzene and toluene vapour at a total flow rate of 200 sccm, respectively..... 74

**Figure 4.7 a)** Humidity response of our sensor in compared to CH<sub>4</sub> response at a total flow rate of 200 sccm. **b)** The sensor responses to 100 ppm of CH<sub>4</sub> at the total flow rate of 200 sccm over a period of 8 months. Overlapping of these data sets reflects high sensor stability. .... 76

**Figure 4.8** The sensor responses to CH<sub>4</sub>' random shuffling concentration range of 1.5-100 ppm with different total flow rate range of 12.5-200 sccm. Error bars represent standard deviations of 7 measurements. Error bars for each data point are in the order of 1-10%. Red lines are a guide to the eyes..... 77

**Figure 4.9** Calibration curves showing linearity of the sensor responses to CH<sub>4</sub>' random shuffling concentration range of 8-100 ppm at different total flow rate of 12.5-200 sccm. Red lines are linear fitting of data..... 78

**Figure 4.10 a)** Sensor sensitivity for 8-100 ppm of CH<sub>4</sub> at different total flow rates of 12.5-200 sccm. **b)** The effect of variation of total flow rate on our sensor's normalized resistance change. .... 79

**Figure 4.11** The effect of variation of thickness on the response of the fabricated sensor to CH<sub>4</sub> in concentration range of 1.5-600 ppm for total flow rates of **a)** 12.5 sccm, and **b)** 200 sccm. Red and black lines are a guide to the eyes..... 80

**Figure 4.12 a)** The dynamic response/recovery signals of the sensor with ZIF-8/10wt%MWCNTs for CH<sub>4</sub> at a total flow rate of 200 sccm: As it is evident our sensor shows very good response in

this range of concentrations, even as low as 10 ppb. **b)** Negative normalized resistance changes as a function of CH<sub>4</sub> concentration depicting the LOD from power law fit of obtained response data. **c)** Comparative normalized resistance change responses, and **d)** response and recovery times of CH<sub>4</sub> for the sensor with 5 and 10wt% of MWCNTs. All error bars represent standard deviations of 7 measurements. .... 81

**Figure 4.13 a)** Schematic illustration of ZIF-8 crystal structure with different adsorption sites, **b)** The adsorption sites for each of CH<sub>4</sub>, CO<sub>2</sub>, alcohols, and water vapours' physisorption into the ZIF-8 pores and surface via electron accepting or donating. .... 84

**Figure 5.1** Sensing responses of **a)** ZIF-8-coated QCM sensor, **b)** ZIF-8/MWCNT-coated QCM sensor, and **c)** ZIF-8/MWCNT-coated IDE chemiresistive sensor to varying concentrations (0.62-20 ppm) of acetone, IPA, ethanol, and methanol at RT (25 C°), respectively. All error bars represent standard deviations of seven measurements. .... 93

**Figure 5.2 a)** Normalized resistance changes of the ZIF-8/MWCNT-coated chemiresistive sensor toward 20 ppm of IPA, 20 ppm of ethanol, 20 ppm of methanol, 20 ppm of acetone, 900 ppm of CO<sub>2</sub>, and varying RH levels (30-90% RH), and selectivity tests of 20 ppm acetone in a binary mixture in presence of 20 ppm of IPA, 20 ppm of ethanol, 20 ppm of methanol, 900 ppm of CO<sub>2</sub>, and varying RH levels (30-90% RH) at a total flow rate of 100 sccm, respectively. **b)** The dynamic response/recovery signals of the chemiresistive sensor for acetone at a total flow rate of 100 sccm: as it is evident the chemiresistive sensor shows complete reversibility and good response in this range of concentrations, even as low concentration as 0.62 ppm. **c)** Acetone response and recovery times for the ZIF-8/MWCNT-coated chemiresistive sensor as a function of acetone concentration. **d)** Normalized resistance changes as a function of acetone concentration depicting the LOD from power law fit of obtained response data. All error bars represent standard deviations of seven

measurements. **e)** Normalized resistance changes of the ZIF-8/MWCNT-coated chemiresistive sensor toward 20 ppm of IPA, 20 ppm of ethanol, 20 ppm of methanol, 0.62 ppm of acetone, 900 ppm of CO<sub>2</sub>, and varying RH levels (30-90% RH), and selectivity tests of 0.62 ppm of acetone in a binary mixture in presence of 20 ppm of IPA, 20 ppm of ethanol, 20 ppm of methanol, 900 ppm of CO<sub>2</sub>, and varying RH levels (30-90% RH) at a total flow rate of 100 sccm, respectively..... 96

**Figure 5.3** a) Schematic illustration of water, acetone, IPA, ethanol, methanol, and CO<sub>2</sub> molecules physisorption into the pores and surfaces of ZIF-8/MWCNT via electron accepting from or donating to ZIF-8/MWCNT layer and the net exchanged electrons ( $\Delta e^-$ ) from the sensing layer to them. .... 100

**Figure 6.1** Schematic of the photodetector device based on 8  $\mu\text{m}$  thick ZIF-8/CNFs spray-coated thin film on the surface of an IDE chip..... 107

**Figure 6.2** Tauc's plots for the optical band gap energy determination of CNFs (black), ZIF-8 (red) and ZIF-8/CNFs nanocomposite (blue), respectively. .... 108

**Figure 6.3** Photoelectric properties of ZIF-8/CNFs photodetector at RT. **a)** I–V characteristics ZIF-8/CNFs under -3 to 3 V bias voltage in a dark environment. **b)** Response of the PD under dark and laser illuminated of 404, 532, and 535 nm to show selectivity. **c)** I–V curves for different power intensities of 404 nm wavelength. **d)** The power-dependent responsivity, **e)** the light density-dependent detectivity, and **f)** External quantum efficiency (EQE) of the PD versus optical power intensity at different bias voltage. Photoresponse of the PD as a function of time at bias voltage of **g)** 0.0005 V and **h)** 3 V. **i)** Rising and falling edges for estimating rise time ( $T_r$ ) and the fall time ( $T_f$ ) the PD under 404 nm laser illumination at bias voltage of 3V. .... 111

## List of Tables

<b>Table 2.1</b> Summary of CH <sub>4</sub> sensing performance of different materials (reproduced with permission from ref [1], copyright (2023) Elsevier).....	15
<b>Table 2.2</b> Metal Oxides based resistive breath acetone sensors for diabetes detection [57].....	20
<b>Table 2.3</b> Comparative Evaluation of Photodetectors (PDs) Utilizing Various Low-Dimensional Nanomaterials (reproduced with permission from ref [70], Copyright (2023) Wiley). ....	24
<b>Table 3.1</b> Surface properties and porosity data of ZIF-8 and ZIF-8/MWCNTs nanocomposite.	46
<b>Table 3.2</b> Descriptions of the parameters in equations (3-1)–(3-4) .....	60
<b>Table 3.3</b> Summary of VOCs properties.....	61
<b>Table 4.1</b> Comparison table of different materials’ sensing performance for CH <sub>4</sub> detection. Reproduced with permission from ref 1. Copyright (2020) Elsevier. ....	85
<b>Table 5.1</b> Summary of VOCs’ properties.....	99
<b>Table 5.2</b> Comparison of Sensing Performance for Acetone Detection at RT with previous works. ....	101
<b>Table 6.1</b> Comparison of this work with earlier reported MOFs based photodetector.....	114

## List of Symbols & Abbreviations

CH <sub>4</sub> :	Methane
RT:	Room Temperature
MOFs:	Metal organic frameworks
CNTs:	Carbon nanotubes
MWCNTs:	Multiwall carbon nanotubes
CNFs:	Carbon nanofiber
ppm:	Parts per million
ppb:	parts per billion
QDs:	Quantum dots
NPs:	Nanoparticles
ZIF-8:	Zeolitic Imidazolate Framework-8
VOCs:	Volatile Organic Compounds
CB	Conduction Band
VB	Valance Band
FT-IR:	Fourier Transform Infrared spectroscopy
XRD:	X-ray Diffraction
UV-Vis:	Ultraviolet–Visible

FE-SEM:	Field Emission-Scanning electron microscopy
IDE:	Interdigitated electrodes
PANI:	Polyaniline
PPy:	Polypyrrole
PTh:	Polythiophene
QCMs:	Quartz crystal microbalance
SAW:	Surface acoustic wave
EC-MOFs:	Electro conductive MOFs
LBL:	Layer-by-layer
DMF:	N, N Dimethylformamide
Hmim:	2-Methylimidazole
sccm:	Standard cubic centimeter per minute
MFC:	Mass flow controller.
LOD:	Limit of detection
RH:	Relative humidity
DDW:	Double distilled water
PD:	Photodetector
CMOS:	Complementary metal oxide semiconductors

TMDs: Transition metal dichalcogenides

2D: Two-dimensional

3D: Three-dimensional

# Chapter 1 : Introduction

## 1.1 Research Background

In this section, we provide an in-depth exploration of the research backgrounds for three distinct projects involving metal organic framework (MOFs) nanocomposites with multiwall carbon nanotubes (MWCNTs) and carbon nanofibers (CNFs). These projects encompass methane (CH<sub>4</sub>) detection, the potential application of MOFs composites for diabetes diagnosis through acetone detection, and their utilization as advanced photodetectors.

**First project:** Methane ranks as the second most prevalent greenhouse gas, possessing a global warming potential nearly 21 times that of CO<sub>2</sub> per molecule [1]. It can persist in the atmosphere for up to 12 years, gradually diminishing through reactions with entities like ·-OH radicals. CH<sub>4</sub> represents a significant environmental concern, as highlighted by the World Health Organization [2], [3]. With responsibility for 15 percent of Canada's total greenhouse gas emissions, Canadian carbon policies and regulations now demand substantial reductions (45%) in methane emissions by 2025 to safeguard the environment [4]. Additionally, CH<sub>4</sub>, highly flammable and prone to causing explosive events at concentrations between 5-15% by volume (50,000-150,000 ppm), poses a substantial risk, frequently resulting in human and economic casualties. Consequently, the inadvertent release of CH<sub>4</sub> during coal extraction, natural gas pipeline leaks, or outbursts can lead to catastrophic outcomes if not promptly detected and mitigated [1]. Therefore, the detection of CH<sub>4</sub> assumes paramount importance, particularly in the context of environmental preservation and industrial safety related to gas production, transportation, and utilization. Presently, prevailing CH<sub>4</sub> detection techniques encompass infrared spectroscopy [5], Raman spectroscopy [6], chemiresistive sensors [7] and gas chromatography [8], each harboring its own set of advantages

and limitations. Unfortunately, these technologies face challenges in achieving the detection of methane at levels relevant to leaks, typically within the range of a few parts per million (ppm), using miniaturized, and cost-effective devices. Thus, an unmet need persists for the development of innovative, cost-efficient, and dependable miniaturized sensors, characterized by high sensitivity and selectivity, and capable of detecting methane at low concentrations.

In recent years, the progress in micro/nano-fabrication technology and the utilization of newly engineered nanomaterials have paved the way for the development of cost-effective, miniaturized integrated gas sensors. These sensors exhibit heightened sensitivity and selectivity toward various target gases [7]. Among the emerging materials, metal oxides, graphene-based composites, carbon nanotubes (CNTs), and polymers have undergone thorough investigation for their potential as gas sensing materials [1]. However, detecting low concentrations of CH<sub>4</sub> remains a challenge due to the typically weak interaction between this gas and these materials [1], [3], [9]. To confront this challenge, the application of nanoporous framework materials, such as MOFs, holds great promise. MOFs are distinguished by their permanent porosity and expansive surface area. Consequently, they enable the detection of trace levels of CH<sub>4</sub> in a wider range of environments, while delivering superior selectivity and sensitivity.

MOFs represent a distinct class of crystalline and porous solid materials formed through self-assembly processes involving metal nodes (comprising metal ions or clusters) and organic ligands, coordinated by chemical bonds [10]. In recent years, they have garnered significant attention for their potential utility as high-performance sensors for detecting various gases. This interest arises from their unique attributes, which encompass a vast surface area, tunable pore dimensions, functionalizable sites, and intriguing physical properties, including optical absorbance [11]–[13], luminescence [14]–[17], magnetism [18]–[20], resistance [21], [22], conductivity [23]–[25], and

ferroelectricity [26], [27], derived from the constituent metal nodes, organic ligands, guest chemical species, pores, or combinations thereof. Additionally, MOFs hold particular promise for chemical sensing due to several inherent advantages:

1. **Permanent Porosity:** MOFs offer extensive surface areas and numerous active sites conducive to enhancing surface host–guest reactions. Confined pores enable the pre-concentration of target gases, potentially enhancing sensitivity.
2. **Reversibility:** MOFs exhibit excellent reversibility in absorbing and desorbing guest molecules, rendering them highly regenerable and recyclable.
3. **Tunability:** MOFs provide the flexibility to tailor pore size, shape, and surface characteristics, potentially enhancing selectivity and sensitivity. Functional groups, such as Lewis acid or base sites, can also be incorporated into the framework to modify chemical specificity and sensitivity [28], [29].

Based on these principles, diverse MOFs have been developed for deployment as chemiresistive sensors, magnetic sensors, ferroelectric sensors, colorimetric sensors, and luminescent sensors [30]–[39]. However, one well-recognized limitation is the inherently low electrical conductivity of most MOFs, which has constrained their comprehensive adoption in electrical sensor devices. Consequently, the majority of reports in this domain emphasize optical responses, such as luminescence quenching or enhancement [36], [40], [41], or employ complex resonance device architectures like MOF-coated microcantilevers [42] and quartz crystal microbalances(QCM) [43]–[45].

Numerous experimental and theoretical investigations have been conducted to delve into the conductivity properties of various MOFs [45]. The findings from these inquiries have consistently pinpointed the inadequate mobility of charge carriers as the fundamental cause behind MOFs'

subpar conductivity, often registering values below  $10^{-10}$  S  $\text{cm}^{-1}$ . This deficiency primarily arises from the sluggish electron transfer occurring between non-redox-active metal centers and the organic linkers [46], [47]. However, these inherent limitations of MOFs offer avenues for enhancement through several strategies, including composite formation, post-synthetic modification, or the introduction of guest molecules [46], [48]–[50]. One promising approach involves the incorporation of MOFs with other conductive or semiconductive nanomaterials, such as quantum dots (QDs), metal or metal oxide nanoparticles (NPs), 2D-graphene, and CNTs [51]. While there have been a handful of reports detailing the utilization of MOF/MWCNTs for the detection of volatile organic compounds (VOCs) [52], [53], to the best of our knowledge, there exists no prior investigation regarding the application of this composite for  $\text{CH}_4$  detection.

In the context of MOFs, Zeolitic imidazolate framework-8 (ZIF-8) stands out due to its notable characteristics, including low water affinity and stability under ambient conditions. Consequently, ZIF-8 was specifically chosen for this project aimed at  $\text{CH}_4$  detection through the creation of a resistive sensor. However, like many MOFs, ZIF-8 possesses insulating properties and limited electrical conductivity, necessitating a transformation into a conductive material suitable for sensor applications. To achieve this transformation, we developed a composite comprising ZIF-8 nanoparticles and bare MWCNTs. This innovative approach not only enhanced the composite's conductivity but also enabled the highly sensitive detection of low concentrations of  $\text{CH}_4$  under normal atmospheric pressure. Our approach is centered on the concept of reducing the electronic bandgap of the composite through the random incorporation of MWCNTs into the ZIF-8 framework. We employed an in-situ sonochemical method to synthesize the ZIF-8/MWCNT nanocomposite. This strategy holds the potential to confer distinct transport properties to various MOFs. Comprehensive characterization of the synthesized nanocomposite was conducted using

techniques such as Fourier Transform Infrared (FT-IR) spectroscopy, Raman spectroscopy, X-ray diffraction (XRD) analysis, Ultraviolet–visible (UV-VIS) spectroscopy, and Field emission scanning electron microscopy (FE-SEM). Subsequently, a thin film of the ZIF-8@MWCNT nanocomposite was deposited onto interdigitated electrodes (IDE) chips using a spray-coating method, thus creating a resistive sensor layer for the IDE device. Notably, this represents the inaugural utilization of the ZIF-8/MWCNTs nanocomposite as a sensing layer in a chemiresistive sensor designed for the selective detection of CH<sub>4</sub>. This composite not only exhibited augmented electrical conductivity but also demonstrated increased hydrophobicity. Furthermore, we harnessed its unique electrical transport enhancements to achieve the detection of CH<sub>4</sub> at remarkably low concentrations, as low as 10 parts per billion (ppb) under normal atmospheric conditions, with a limit of detection (LOD) of approximately 0.22 ppb, a level of sensitivity unprecedented in the field. We systematically evaluated our sensor's performance, examining responsivity, reversibility, selectivity, response and recovery time, sensitivity, repeatability, and linearity. Notably, the sensor exhibited a minimal response to humidity, positioning it as an excellent candidate for specialized applications in humid environments. Importantly, we offer a novel explanation for the selective response to CH<sub>4</sub> over CO<sub>2</sub>, alcohols, and moisture, which is rooted in the distinct adsorption sites within ZIF-8 with varying electron affinity for different molecules. This novel explanation represents a significant advancement in the field of gas sensing, opening new possibilities for precise and selective gas detection in various environmental conditions.

**Second project:** Diabetes, a chronic health condition characterized by insufficient insulin production or improper insulin utilization, results in elevated blood sugar levels [54], [55]. Its prevalence is steadily increasing, with data from the World Health Organization (WHO) and other sources indicating that 422 million adults worldwide are affected, and it accounts for 1.6 million deaths annually (WHO, 2023) [56], [57]. This trend underscores the pressing need for effective strategies to manage and monitor diabetes, thereby reducing the risk of complications such as diabetic coma and fatality. The conventional approach involves finger pricking to obtain a blood drop for electronic reading, a process that can be painful, invasive, and unsafe for certain individuals. Additionally, diabetes management often necessitates frequent blood glucose monitoring, rendering this method cumbersome [55]. As a result, the exploration of non-invasive and simpler diagnostic techniques, such as human breath analysis, holds significant potential for diabetes detection and monitoring. Several sensitive and selective breath analysis techniques have been proposed, including gas chromatography coupled to mass spectrometry, high-performance liquid chromatography, proton transfer reaction with mass spectrometry, gas chromatography equipped with a flame ionization detector, ion mobility spectrometry, and selected ion flow tube-mass spectrometry, as means of non-invasive acetone detection [55], [58]–[62]. Nonetheless, these techniques are often expensive, non-portable, and sophisticated, which limits their practicality for daily point-of-care diabetes management [63].

Recent research has been increasingly directed towards the development of non-invasive gas sensors based on nanomaterials capable of detecting acetone at room temperature (RT) and atmospheric pressure. This pursuit aims to enable the creation of cost-effective, portable, and user-friendly devices for diabetes management. Numerous endeavors have been made to explore diverse nanomaterials, such as metal oxides, graphene-based composites, carbon nanotubes, and

polymers, for the precise detection of acetone [57], [64]–[66]. The typical concentration levels of acetone in exhaled breath fall within the range of 0.2–1.8 ppm for healthy individuals and 1.25–2.5 ppm for individuals with diabetes [57], [67]. However, in some cases, particularly among individuals with type 1 diabetes, acetone concentration levels can soar as high as 25 ppm [57], [59], [67]. Despite these extensive efforts, it's notable that the majority of nanomaterials have thus far demonstrated the ability to detect acetone only at concentrations exceeding 10 ppm at room temperature (25°C), a range that exceeds the levels typically found in exhaled breath [55], [57], [64]–[66].

To enhance the sensitivity of gas/vapor detection, it is imperative to maximize both the specific surface area and porosity of the sensing materials, as gas reactions predominantly occur on material surfaces. Nanoporous materials, such as MOFs, offer considerable promise in this regard due to their exceptional surface area and permanent porosity [10], [28], [29]. Previous research has explored the utility of MOFs in improving chemical sensitivity for detecting compounds like acetone and other VOCs [68], [69]. Despite these encouraging attributes, there remains a pressing need to enhance the sensitivity, selectivity, and resistance to moisture for MOFs to make them widely applicable in acetone breath sensors. Achieving a reliable response at parts-per-billion (ppb) levels of acetone while mitigating cross-sensitivity, given the significant moisture and CO<sub>2</sub> levels in exhaled breath, presents a considerable challenge. In addressing this challenge, our focus turned to ZIF-8 due to its low water affinity and stability under ambient conditions. However, ZIF-8 alone suffers from a limited VOC sorption capacity at atmospheric pressure and RT. To surmount this limitation, we developed a nanocomposite of ZIF-8 and bare multi-walled MWCNTs, substantially augmenting its sorption capacity for alcohols and acetone. Leveraging a ZIF-8/MWCNT-coated QCM sensor, we successfully detected these VOCs at concentrations as low as

0.62 parts-per-million (ppm) under ambient conditions, marking a significant improvement over ZIF-8 alone. Nevertheless, a crucial requirement in medical diagnostics is the ability to selectively detect acetone, a vital biomarker for diabetes, in the presence of other VOCs. For the first time, our study delves into the impact of different sensing platforms with varying response mechanisms in achieving exceptional selectivity for acetone. Utilizing a ZIF-8/MWCNT-coated QCM and a chemiresistive sensor, the latter demonstrated outstanding acetone detection performance, characterized by high selectivity, minimal humidity interference, robust repeatability, full reversibility, and rapid response times. Most notably, it attained a remarkable limit of detection of 1.7 parts-per-billion (ppb) under ambient conditions—three orders of magnitude lower than the concentration of acetone in the exhaled breath of diabetic patients (1.8 ppm). This groundbreaking achievement underscores the enormous potential of this sensor for diabetes diagnosis and monitoring through breath analysis.

**Third Project:** Photodetectors have emerged as essential components in various technological domains, including optical communication, imaging, sensing, security, environmental monitoring, and medical diagnostics [70]. Despite the considerable progress made in photodetection technologies, significant challenges persist. Conventional photodetectors, predominantly based on inorganic semiconductors like silicon and complementary metal oxide semiconductors (CMOS), have been widely used due to their great compatibility, which guarantees their application in miniaturized photodetectors and other featured devices [70]–[74]. Nonetheless, given the intrinsic drawbacks, e.g., high brittleness and complicated manufacturing process, these traditional photodetectors (PDs) are limited in flexible applications and cost-saving. Besides, due to the broadband absorption of inorganic semiconductors, spectrally selective detection of these PDs is unavailable without attached optical filters [74]. Traditional spectrometers typically utilize

diffraction gratings or dichroic prisms within broad-spectrum photodetectors to achieve spectral selectivity. However, the intricate manufacturing processes and associated high expenses have posed significant obstacles to their widespread commercial adoption [74]. Therefore, nanomaterials have emerged as promising candidates for next-generation photodetectors to overcome the shortcomings of conventional photodetectors [70].

Nanomaterials in nonconventional device architectures have been extensively researched due to their size-dependent optical and electronic properties. Various nanomaterials, such as semiconducting nanoparticles, QDs, graphene, transition metal dichalcogenides (TMDs), perovskite nanocrystals, and organic molecules have demonstrated intriguing optoelectronic properties and impressive photodetection performance [75]–[89]. However, each of these nanomaterials is accompanied by limitations such as toxicity, low responsivity, low quantum efficiency, slow response time, limited tunability, low stability, scalability, inadequate sensitivity in certain wavelength ranges, high cost, fabrication complexities, challenges in large-scale synthesis, challenges in device integration and compatibility with existing fabrication techniques, which hinder their widespread implementation [70], [74], [90], [91].

The distinctive attributes of MOFs, characterized by their ultra-high surface area, tunable structures and properties, diverse chemical functionality, and diverse optical properties, have propelled them to the forefront of nanomaterial research [92], [93]. The versatility of these crystalline networks, composed of metal ions coordinated with organic ligands, has allowed researchers to tailor MOFs for various applications, including gas storage, separation, catalysis, and sensing [68], [69], [92]–[98]. Their intrinsic light-harvesting abilities and potential for modification make them attractive candidates for photodetection. Incorporating MOFs into photodetectors can lead to enhanced light absorption, charge separation, selectivity and tailored

photoresponse. While two-dimensional (2D) MOFs and single crystal MOFs have demonstrated promising photodetection capabilities [94], [99]–[103], their three-dimensional (3D) counterparts have faced inherent limitations in terms of limited carrier mobility and slow charge transport dynamics, hindering their ability to swiftly respond to photogenerated carriers [46], [47], [50]. Nonetheless, challenges associated with the synthesis of single crystal MOFs, high-quality and large area 2D MOF films, and their integration into device architectures hinder their widespread adoption. These constraints have motivated us to explore composite systems to leverage the strengths of 3D MOFs while addressing their weaknesses.

This study focuses on synergizing MOFs and CNFs in a new class of nanocomposite for the very first time to address their individual limitations and create an enhanced nanocomposite material. By capitalizing on the strengths of both MOFs and CNFs and mitigating their individual limitations, this novel approach not only seeks to address the shortcomings of traditional photodetectors but also extends the capabilities of 3D MOFs in photodetection applications. From the extensive array of MOFs, ZIF-8 was selected due to its exceptional stability and minimal water affinity. By combining ZIF-8's ultrahigh surface area and CNFs' superior conductivity, the resultant nanocomposite demonstrates significant enhancements in light absorption, photoresponse, charge transport, and charge separation. This composite strategy facilitates precise control over optoelectronic properties and offers a platform for selectivity modulation via band gap manipulation, obviating the need for external optical filters. This unique attribute simplifies the fabrication of spectrally selective photodetectors, ultimately reducing manufacturing costs. This innovative synergy between MOFs and CNFs holds promise in revolutionizing photodetection technology and catalyzing advancements in diverse areas of optoelectronics.

## 1.2 Goal and Objectives

As sensing materials hold a pivotal role in shaping the performance of gas sensors and photodetectors, an effective strategy involves enhancing sensor properties through the modification of these materials. This thesis centers on the augmentation of MOFs for various applications by crafting nanocomposites with MWCNTs and CNFs across three distinct projects. These projects encompass methane detection, the application of MOFs composites for diabetes diagnosis via acetone detection, and their utilization as advanced photodetectors, each pursued with the following objectives in mind:

**Objective of First and Second project:** Within the scope of the first and second projects, centered on CH<sub>4</sub> and acetone detection, respectively, certain challenges persist in the realm of sensing materials as elaborated upon in the subsequent chapter. Despite substantial research efforts aimed at enhancing sensing performance in these domains, enduring obstacles continue to be of concern, and are outlined as follows:

1. **Lowering Operating Temperature:** One of the primary drawbacks afflicting many resistive sensors is their requisite high operating temperatures, often exceeding 100°C. An imperative query arises: What strategies can be employed to mitigate this drawback and reduce the dependence on elevated temperatures for sensor functionality?
2. **Moisture Mitigation:** The affinity of sensing materials for moisture remains a substantial concern. How can we effectively diminish this susceptibility to moisture, ensuring consistent and reliable sensor performance even in humid environments?
3. **Lowering Limit of Detection (LOD):** Whether applied in environmental monitoring or as a breath analyzer, there is a pressing need to lower the LOD. How can we achieve greater sensitivity, allowing for the detection of trace quantities of target gases?

4. **Enhancing Selectivity:** In real-world applications, target gases often coexist with a multitude of other gases. Ensuring high selectivity for the target analyte is crucial. What strategies can be employed to enhance selectivity in the presence of potentially interfering gases?

These questions underscore the complexity of the challenges at hand and serve as a driving force, compelling us to tackle these issues head-on in the pursuit of achieving highly effective CH<sub>4</sub> and acetone detection. Our approach involves the creation of an innovative nanocomposite comprising ZIF-8 and MWCNTs as the sensing material, with the overarching goal of realizing lower operating temperatures, improved LOD, reduced sensitivity to water interference, and enhanced selectivity.

**Objective of Third project:** The innate light-harvesting capabilities and versatility of MOFs position them as highly attractive candidates for photodetection applications. Integrating MOFs into photodetectors offers the potential to significantly enhance light absorption, enable efficient charge separation, improve selectivity, and tailor the photoresponse. Although 2D MOFs and single crystal MOFs have shown substantial promise in photodetection, their 3D counterparts have encountered inherent limitations. These challenges primarily revolve around limited carrier mobility and sluggish charge transport kinetics, impeding their ability to promptly respond to photogenerated carriers.

However, the synthesis complexities associated with single crystal MOFs, the production of high-quality large-area 2D MOF films, and their integration into device architectures have impeded their widespread adoption. These constraints have fueled our exploration of composite systems, with the aim of harnessing the strengths of 3D MOFs while mitigating their weaknesses. In this groundbreaking study, we embark on a pioneering investigation into nanophotodetectors,

capitalizing on the novel MOF nanocomposites incorporating CNFs. This innovative approach promises to revolutionize the field of photodetection by unlocking the full potential of 3D MOFs in combination with CNFs.

### **1.3 Thesis Overview**

This thesis consists of seven chapters, which are listed as follows.

**Chapter 1** introduces the research background, research questions, and research objectives.

**Chapter 2** overviews different nanomaterials for detection of methane, acetone and as photodetectors, MOFs nanoparticles Synthesis Strategies, MOFs composites Synthesis Strategies, MOFs Thin Film fabrication methods, and MOF-based gas sensing methods.

**Chapter 3** describes the experimental method, including materials synthesis, materials Characterization, Thin film and sensor fabrication, experimental test setup and sensing experiment.

**Chapter 4** focuses on ZIF-8-MWCNTs based resistive sensor for detection of methane.

**Chapter 5** focuses on ZIF-8-MWCNTs based QCM sensor for detection of VOCs, and ZIF-8-MWCNTs based resistive sensor for detection of acetone for diabetes diagnosis.

**Chapter 6** focuses on ZIF-8/CNTs nanocomposite as a spectrally selective photodetector.

**Chapter 7** gives the conclusions of this research and recommendations for future studies.

## Chapter 2 : Literature Review

In sensor design, a significant role is played by sensing materials in their interaction with target gases or light sources. The selectivity, reversibility, and repeatability of the sensors are determined by the properties of these materials, and they can also be influenced by the sensitivity and response kinetics. The nanoscale dimensions of these sensing materials imbue them with a range of characteristics, including expansive surface-to-volume ratios and distinct chemical, optical, and electrical properties. This substantial surface area offered by the nanomaterials creates exceptionally active interfaces, ultimately enhancing sensitivity and reducing both response and recovery times [55]. In recent years, the development of cost-effective miniaturized integrated gas sensors and photodetectors with improved performance has been facilitated by advancements in nano-fabrication technology and the utilization of newly designed nanomaterials [7]. In this chapter, we present an overview of the nanomaterials utilized in the detection of CH<sub>4</sub> and acetone, along with those applied in photodetection, highlighting the challenges associated with them. Additionally, we discuss strategies for synthesizing MOFs nanoparticles, fabricating MOFs composites, producing MOFs thin films, and employing MOF-based methods for gas sensing.

### 2.1 Nanomaterials for Detection of Methane

Various nanomaterials have been employed in the detection of CH<sub>4</sub>. Among the newly developed nanomaterials, extensive research efforts have been dedicated to investigating metal oxides, graphene-based composites, CNTs, and polymers as potential sensing materials for CH<sub>4</sub> [1]. **Table 2.1** summarizes a summary of CH<sub>4</sub> sensing performance of different materials. In contrast to a range of other gas sensors designed for gases like NH<sub>3</sub>, H<sub>2</sub>, etc., the quest for highly reversible and selectively sensitive CH<sub>4</sub> detection materials, capable of detecting it at low concentrations, remains

an ongoing endeavor. Thus, the evaluation of Sensing Reversibility, Selectivity and LOD is generally “Low” or “Medium” in **Table 2.1** [1].

**Table 2.1** Summary of CH<sub>4</sub> sensing performance of different materials (reproduced with permission from ref [1], copyright (2023) Elsevier).

Materials	Operating Temperature	Response Time (s)	Sensing Reversibility	Selectivity	Limit of Detection (ppm)
Metal oxides	25°C-900°C (typically >150°C)	10 <sup>0</sup> -10 <sup>2</sup>	Low-Medium	Low-Medium	10 <sup>0</sup> -10 <sup>3</sup>
Carbon	Room Temperature (RT) -450°C	10 <sup>1</sup> -10 <sup>2</sup>	Low-Medium	Low-Medium	10 <sup>1</sup> -10 <sup>4</sup>
Conducting Polymers	RT	10 <sup>1</sup> -10 <sup>2</sup>	Low-Medium	Low-Medium	10 <sup>2</sup> -10 <sup>3</sup>
MOFs	RT	10 <sup>1</sup> -10 <sup>2</sup>	Medium-High	Medium	10 <sup>4</sup> -10 <sup>5</sup>

**Metal oxides materials:** The most frequently employed sensing materials for the chemical detection of CH<sub>4</sub>, as extensively documented in scientific literature, include semiconducting metal oxides [104], [105], such as Tin oxide/stannic oxide (SnO<sub>2</sub>) [106], [107], Zinc Oxide (ZnO) [108], [109], Vanadium oxide (VO<sub>x</sub>) [110], [111], Ga<sub>2</sub>O<sub>3</sub> [112], Molybdenum oxide (MoO<sub>3</sub>) [113], Cobalt oxide (Co<sub>3</sub>O<sub>4</sub>) [114], among others. These materials can detect CH<sub>4</sub> by monitoring changes in their electrical or optical properties. Nevertheless, in order to attain a methane sensitivity that is deemed suitable and achieve a reversible sensing response, metal oxide-based sensing layers typically necessitate operation at elevated temperatures, and are associated with high LOD [1].

**Carbon materials:** As opposed to metal oxide-based sensors that require elevated temperatures for operation, an alternative category of sensing materials, exemplified by carbon nanomaterials (such as CNTs and graphene-related materials), offers the potential for excellent detection sensitivity even at RT, coupled with intriguing transduction properties [115], [116]. These materials present a compelling option for gas sensors owing to their considerable specific surface area, relatively high electrical conductivity, and distinctive electronic band-structure

characteristics [117]–[119]. Carbon-based materials detect CH<sub>4</sub> through changes in their electrical or optical properties, exhibiting significant conductivity alterations in response to minute quantities of adsorbed gas molecules [120]. Typically, the electrical resistance of carbon nanostructures undergoes modification due to electron transfer between these structures and gas molecules, either oxidizing or reducing, adsorbed on their surface, with this electron exchange constituting the predominant sensing mechanism [121]. For instance, CNTs demonstrate p-type semiconductor characteristics, wherein oxidizing gases abstract electrons from CNTs, resulting in hole production and a subsequent decrease in resistance following the interaction. Conversely, reducing gases contribute electrons, leading to their recombination with holes, thereby increasing the resistance of CNTs after interaction [122]. However, both theoretical and experimental studies have revealed that sensors relying on pristine CNTs exhibit poor sensitivity when detecting non-polar gases such as CH<sub>4</sub>. This limitation primarily stems from the chemical stability conferred by strong sp<sup>2</sup> bonds and weak sp<sup>3</sup> bonds at the tube ends of CNTs, rendering CH<sub>4</sub> molecules incapable of either accepting or donating electrons and thus unable to induce changes in the conductance of CNTs [123], [124]. The same challenge extends to graphene-based materials. Consequently, carbon-based materials are frequently subject to modification through the introduction of functional groups [125], [126], metallic NPs [127], [128], metal-oxide NPs [129]–[131] and polymers [132], [133] to overcome the constraints associated with CH<sub>4</sub> detection [1].

**Conducting polymers composites:** Another category of sensing materials comprises conducting polymers, which encompasses substances like polyaniline (PANI), polypyrrole (PPy), polythiophene (PTh), and more. These polymers exhibit the capability to detect CH<sub>4</sub> through alterations in their electrical, mass, or optical properties. When compared to extensively studied metal oxides, conducting polymers offer superior sensitivity, shorter response times, and the ability

to operate effectively at RT. Additionally, conducting polymers possess commendable mechanical properties, simplifying the sensor fabrication process. Unlike conventional polymers, which are typically dielectric or insulating in nature, conducting polymers feature alternating single and double bonds in their backbones, resulting in broad  $\pi$ -electron conjugation [134]. Current CH<sub>4</sub> sensors based on conducting polymers utilize chemiresistor and QCM platforms. Examples include PANI/PdO composite film [135], PANI/MWCNT [136], Cu-BTC/PANI [137], and PANI/ZnO [138], all of which have demonstrated room temperature CH<sub>4</sub> sensing capabilities. However, it is worth noting, as depicted in **Table 2.1**, that these sensors exhibit LOD in the range of 100-1000 ppm, with moderate selectivity and reversibility [1].

**Metal-organic frameworks (MOFs):** A novel class of porous materials has gained attention for its superior performance when compared to the previously mentioned sensing materials. MOFs, characterized by their exceptionally large surface areas and functional groups, enable robust interactions with guest molecules. These interactions can result in alterations of MOF properties, affecting optical, electrical, and mechanical signals [139]. Despite their demonstrated prowess in detecting polar molecules, organic compounds, and ions, the number of reported MOF-based CH<sub>4</sub> sensors remains limited.

A series of simulation studies have investigated the selection of MOF materials for CH<sub>4</sub> sensing [140]–[142]. Regarding experimental CH<sub>4</sub> sensors, there have been limited instances of MOF-based CH<sub>4</sub> sensors. Notable examples include a luminescent sensor based on UNMF-0 [143], ZIF-8-based surface acoustic wave devices (SAW) devices, and a QCM sensor [144]. The SAW sensor operated effectively at RT, demonstrating a low LOD of 10-20 vol% for CH<sub>4</sub>. Researchers noted complete reversibility and repeatability, attributed to the physisorption of gases into the MOF pores and the high stability of the devices. These sensors exhibited linear responses to

changes in binary gas compositions, facilitating the construction of calibration curves. In addition to pure MOF-based CH<sub>4</sub> sensors, a ZIF-8/silicone polymer optical fiber sensor was also developed, capable of detecting 1% CH<sub>4</sub> [145].

However, as indicated in **Table 2.1**, despite the superior selectivity and reversibility of MOF-based CH<sub>4</sub> sensors compared to other sensing materials, there remains a need for improving the LOD before MOFs can be widely deployed for CH<sub>4</sub> sensing in field conditions. The generally weak interaction between MOFs and CH<sub>4</sub> contributes to the low LOD in MOF-based sensors. For sensing layers constructed from other materials, the LOD is significantly affected by the low polarizability of CH<sub>4</sub> [1]. Therefore, addressing this challenge in CH<sub>4</sub> sensing is one of the key objectives of this study, aiming to enhance the interaction between CH<sub>4</sub> molecules and the ZIF-8 surface by manipulating the band gap energy of the fabricated sensing layer.

## **2.2 Nanomaterials for Detection of Acetone for Diabetes**

While blood glucose measurements are commonly employed for diagnosis, breath analysis has been demonstrated to offer more precise control over a patient's diabetic condition by allowing real-time measurements of acetone concentration, which is strongly correlated with ketone levels in the bloodstream [146]. Recent studies have seen a shift towards the development of non-invasive nanomaterial-based gas sensors that are capable of detecting acetone at RT and atmospheric pressure. Substantial efforts have been devoted to the development of various nanomaterials, including metal oxides and composites of metal oxides with graphene, CNTs, and conductive polymers, for the detection of acetone at RT [57], [64]–[66]. Typically, acetone concentration levels in exhaled breath fall within the range of 0.2–1.8 ppm for healthy individuals and 1.25–2.5 ppm for those with diabetes [57], [67]. Despite the concerted efforts made thus far, the majority of

nanomaterials have only demonstrated the capability to detect acetone at concentrations exceeding 10 ppm at RT (25°C), which lies outside the range of exhaled acetone levels [55], [57], [64]–[66]. Furthermore, these nanomaterials frequently lack the necessary selectivity to accurately identify acetone in the presence of other gases or vapors. This limitation restricts their applicability in the realm of acetone breath sensors. Consequently, the pursuit of selective acetone detection at low concentrations and under RT conditions remains an ongoing development.

**Metal oxides and metal oxide composite nanomaterials:** Chemoresistive sensors, primarily utilizing various semiconducting metal oxides like  $\text{WO}_3$ , Tin oxide/stannic oxide ( $\text{SnO}_2$ ),  $\text{Fe}_x\text{O}_y$ ,  $\text{TiO}_2$ ,  $\text{CuO}$ , Zinc Oxide ( $\text{ZnO}$ ), and Indium oxide ( $\text{In}_2\text{O}_3$ ), among others, have predominantly been employed for the noninvasive detection and screening of diabetes [57]. Depending on the conduction type, these metal oxide semiconductors can be categorized into n-type and p-type [147], each exhibiting distinct sensing behaviors towards the same detecting gas. The alteration in conductivity of the semiconducting metal oxide material when exposed to the target gas is contingent upon the type of majority carriers within the semiconducting metal oxide material (n-type: electrons and p-type: holes), as well as the nature of gas molecules (either oxidizing or reducing) at RT [57]. One of the challenges encountered in metal oxide-based chemiresistive gas sensors is the enhancement of stability. The limited stability of metal oxide gas sensors results in issues such as false alarms, uncertain outcomes, and ultimately necessitates sensor replacement. The stability of metal oxide gas sensors can be enhanced through processes like calcination during preparation and film annealing as post-processing treatments [55]. Another approach to bolster the stability of breath acetone sensors based on metal oxides involves synthesizing mixed metal oxides and/or doping metal oxides with carbon nanotubes. **Table 2.2** presents recent examples of metal oxides and their composite-based chemiresistive breath acetone sensors for diabetes detection [57].

**Table 2.2** Metal Oxides based resistive breath acetone sensors for diabetes detection [57].

Sensing Materials	LOD (ppm)	Operating Temperature (°C)
TiO <sub>2</sub> functionalized In <sub>2</sub> O <sub>3</sub>	0.8	250
NiO/ZnO hollow spheres	100	275
ZnO decorated with Pt and Nb	50	450/400
TiO <sub>2</sub> nanoporous	500	370
Au modified $\alpha$ -Fe <sub>2</sub> O <sub>3</sub>	50	150
SnO <sub>2</sub> /MWCNT	1	250
PPy-WO <sub>3</sub> Hybrid	37	90
Pt-loaded $\alpha$ -Fe <sub>2</sub> O <sub>3</sub>	0.8	220
Ca-doped YbFeO <sub>3</sub>	0.1	250
C-doped WO <sub>3</sub>	0.9	350
CdMoO <sub>4</sub>	0.5	625
ZnO:Ni	116	340
Pd-ZnO/ZnCo <sub>2</sub> O <sub>4</sub>	0.4	250
C <sub>3</sub> N <sub>4</sub> -SnO <sub>2</sub>	0.067	380
In loaded WO <sub>3</sub> /SnO <sub>2</sub>	50	200
SnO <sub>2</sub> /SiO <sub>2</sub>	1	170
CdNb <sub>2</sub> O <sub>6</sub>	0.2	600
Mesoporous $\alpha$ -Fe <sub>2</sub> O <sub>3</sub> nanospheres	0.1	170
Cuboid WO <sub>3</sub>	0.5	300
ZnO-Fe <sub>3</sub> O <sub>4</sub>	0.1	485
ZnO/TiO <sub>2</sub> nanofibers	5	350
NiO/SnO <sub>2</sub>	0.01	300
PANI/Cellulose/WO <sub>3</sub>	10	RT (25)
NiFe <sub>2</sub> O <sub>4</sub>	0.52	160
Ru-loaded WO <sub>3</sub>	0.5	300
Co <sub>1-x</sub> Zn <sub>x</sub> Fe <sub>2</sub> O <sub>4</sub>	0.3	650
Fe and C codoped WO <sub>3</sub>	0.9	300
Pt functionalized SnO <sub>2</sub>	0.0036	300
MgFe <sub>2</sub> O <sub>4</sub> /g-C <sub>3</sub> N <sub>4</sub>	500	320
Apo-Pt@HP_WO <sub>3</sub>	1	350
Sm <sub>2</sub> O <sub>3</sub> /SnO <sub>2</sub>	0.1	250
WO <sub>3</sub> /Pt-GNs	10	200
Rh/WO <sub>3</sub>	0.5	250
Sb-doped In <sub>2</sub> O <sub>3</sub>	50	240
Cr-doped CuO	0.32	450
Go-SnO <sub>2</sub> -TiO <sub>2</sub>	0.25	200
Pt@In <sub>2</sub> O <sub>3</sub>	0.01	320
g-C <sub>3</sub> N <sub>4</sub> /WO <sub>3</sub>	100	340
N-SnO <sub>2</sub>	0.007	300

The limitation related to operational temperature is another significant factor affecting sensing applications of metal oxides. As indicated in **Table 2.2**, the majority of these metal oxides are only capable of detecting acetone when exposed to elevated temperatures. Despite extensive efforts aimed at enhancing the sensitivity and selectivity of breath acetone sensors, the primary drawback

remains the requirement for high operational temperatures. Associated disadvantages include limited flexibility, increased power consumption, safety risks, reduced device lifespan [148], impracticality for accommodating flammable substances, and other environmental concerns [149]. Numerous research endeavors have been undertaken to develop acetone sensors capable of operating at RT. Conducting polymers offer a promising solution due to their potential for high sensitivity, rapid response times, and RT operation. For instance, a conductive polymeric matrix comprised of PANI-WO<sub>3</sub> nanomaterial doped with cellulose was employed for acetone detection at RT and low concentrations. The sensor demonstrated a limit of detection of 10 ppm after repeated exposure to acetone, highlighting its suitability for RT acetone sensing without the significant drawbacks associated with systems requiring high operating temperatures [150]. However, despite these considerable efforts, achieving a limit of detection of 10 ppm at RT still falls outside the range of exhaled acetone levels.

**Metal-organic frameworks (MOFs):** To enhance sensitivity and achieve a lower LOD, the maximization of specific surface area and porosity is deemed crucial, as gas reactions predominantly take place on the surface of materials. Nanoporous materials, exemplified by MOFs, are being considered as a promising choice due to their high surface area, permanent porosity, adjustable pore dimensions, and modifiable internal pore surfaces, which afford active sites featuring diverse electron affinities [10], [28], [29]. Previous research has delved into MOFs' potential for enhancing chemical sensitivity and selectivity in the detection of acetone and other VOCs [68], [69]. However, despite these encouraging attributes, it is still challenging to achieve a reliable response at parts-per-billion (ppb) levels of acetone while avoiding cross-sensitivity due to the presence of large amounts of moisture and CO<sub>2</sub> in exhaled breath.

Hence, to address the LOD challenge in acetone sensing, one of the objectives of this study is the manipulation of the band gap energy of the fabricated sensing layer to enhance the interaction between acetone molecules and the surface of ZIF-8. Furthermore, in pursuit of selectivity towards acetone, a critical biomarker for diabetes, we conducted an investigation involving different sensing platforms with distinct sensing mechanisms in our quest to achieve the desired selectivity.

### **2.3 Nanomaterials for Photodetection**

In materials at the nanometer scale, the electronic properties and capabilities are heavily influenced by their atomic structural arrangement and how they interact with other materials [151]. Substantial progress has been made in creating different low-dimensional nanomaterials, including zero-dimensional (0D) [152], [153], one-dimensional (1D) [154], and two-dimensional (2D) [155], [156] structures, with the aim of enhancing the optoelectronic properties and functions of PDs. This section will provide an overview of recent research in the use of low-dimensional materials for photodetection applications:

**2D nanostructure materials:** 2D layered materials confine carrier movement to a single spatial dimension at the nanoscale. In-plane atoms form covalent bonds, while van der Waals forces bind the 2D layers, resulting in an ultrathin atomic-level thickness [70]. 2D materials like graphene [157]–[159], transition metal dichalcogenides (TMDCs) [160], [161], perovskite [162]–[164], and black phosphorus (BP) [165], [166] have been explored to improve the optoelectronic performances of PDs. They can be produced through simpler solution-based methods compared to conventional epitaxial semiconductors. They exhibit distinctive photonic characteristics, including high optical transparency and excellent absorption across a wide range of wavelengths [70].

**1D nanostructure materials:** 1D nanostructure materials including nanowires (NWs) [167], [168], nanorods (NRs) [169], [170], and nanotubes (NTs) [170], [171] with 1D limited nanoscale occupy additional 2D confined spatial dimension within the nanoscale, leading to abundant novel phenomena and unique properties. In addition, high surface-to-volume ratio and small diameter make them specifically attractive for potential optoelectronic applications.

**0D nanostructure materials:** 0D nanostructured materials, such as NPs [172] and QDs [173]–[175], confine excitons in all three spatial dimensions. Additionally, 0D materials exhibit the quantum confinement effect when their particle size is smaller than the de Broglie wavelength, resulting in an increased density of states that can be tuned by varying the particle size and shape [176]. Consequently, they display unique and exceptional photosensitive properties with three-dimensional adjustability. This characteristic enables the creation of more compact and versatile photodetection systems by reducing device size and enhancing sensor resolution [70].

The performance of recent photodetectors based on low-dimensional nanomaterials is summarized in **Table 2.3**. However, each of these nanomaterials comes with inherent limitations, such as toxicity, low responsivity, limited quantum efficiency, slow response times, restricted tunability, low stability, scalability challenges, inadequate sensitivity within specific wavelength ranges, high fabrication costs, complex manufacturing processes, difficulties in large-scale synthesis, and compatibility issues with existing fabrication techniques. These limitations have impeded their widespread adoption [70], [74], [90], [91]. To overcome these challenges, a composite or hybrid approach that combines multiple nanomaterials has been explored. This hybridized synergistic combination of heterostructure optoelectronics and photodetector devices has been demonstrated to expand their applications and enhance photonic performance and functionalities [177]–[179].

**Table 2.3** Comparative Evaluation of Photodetectors (PDs) Utilizing Various Low-Dimensional Nanomaterials (reproduced with permission from ref [70], Copyright (2023) Wiley).

Dimension	Materials	$\lambda$ [ $\mu\text{m}$ ]	Responsivity [A W <sup>-1</sup> ]	EQE [%]	Response time [ms]	Detectivity [Jones]
2D	Graphene	0.78–1.5	9197	11.5	0.275	–
	Graphene	1.5	0.1	64	< 0.1	–
	Graphene	10.6	$\approx 5$	ss	< 4.2	$3.6 \times 10^5$
	Graphene	1.55	240	–	–	$3.4 \times 10^{12}$
	Graphene	0.47–27.12	5.36	–	68	$1.57 \times 10^9$
	Graphene/tellurium	<2	$1.04 \times 10^9$	6	0.028	$3.69 \times 10^8$
	Graphene/PTCDA/pentacene	0.5~0.67	$\approx 10^4$	9	< 0.028	–
	NPMLgraphene-FeCl <sub>3</sub>	1.3–12	$6.15 \times 10^3$ (V/W)	–	0.0001	$2.3 \times 10^9$
	MoS <sub>2</sub>	0.45–0.97	29	7.8	300	$\approx 10^9$
	MoSe <sub>2</sub> -WSe <sub>2</sub>	0.52	110	23.4	–	$10^9$
	Cs <sub>3</sub> Cu <sub>2</sub> I <sub>5</sub>	0.27	3.78	$\approx 2$	163	–
	Cs <sub>2</sub> Pb(SCN) <sub>2</sub> Br <sub>2</sub> /MoS <sub>2</sub>	0.3–0.8	$1.22 \times 10^5$	8.99	165	$1.16 \times 10^{14}$
	BP/Bi <sub>2</sub> O <sub>2</sub> Se	1.3	0.89	84	0.118	$1.14 \times 10^{10}$
	BP/MoS <sub>2</sub>	0.365	77.16	200	–	$6.5 \times 10^9$
	CsPbCl <sub>3</sub>	0.44, 0.98	1.96, 0.12	–	–	$5 \times 10^{12}, 2.15 \times 10^9$
	(CH <sub>3</sub> (CH <sub>2</sub> ) <sub>3</sub> NH <sub>3</sub> ) <sub>2</sub> (CH <sub>3</sub> NH <sub>3</sub> ) <sub>3</sub> Pb <sub>4</sub> I <sub>13</sub>	0.63	0.53	103	17	$3.24 \times 10^{13}$
	CsPb <sub>2</sub> Br <sub>5</sub>	0.405	75.4	–	43	$\approx 10^{10}$
	PbS nanoplatelets	0.35–0.65	0.02	–	160	$3.96 \times 10^{10}$
Silicon/BP	1.95	125	–	–	–	
1D	Sb <sub>2</sub> Se <sub>3</sub> nanowires	0.52	270	984	<8	$1.27 \times 10^{11}$
	V-WO <sub>3</sub> nanorods	0.25–0.9	$4.5 \times 10^3$	70	2	$5.15 \times 10^{11}$
	ZnO:B/Sb <sub>2</sub> Se <sub>3</sub> nanorods	0.46	0.137	$\approx 40$	–	$1.33 \times 10^{11}$
	InN/In <sub>2</sub> S <sub>3</sub> nanorods	0.365	0.14	–	0.022	$4 \times 10^{10}$
	InGaN nanorods	0.385	$\approx 10^5$	$10^7$	0.05	–
	GaAsSb	0.532	11.7	$2.74 \times 10^3$	0.05	$1.64 \times 10^{11}$
	PbSe nanorods	0.405–10.64	0.78	–	0.0175	$5.1 \times 10^{10}$
	Tellurium nanorods	0.633	6.1	40.9	–	$1.2 \times 10^{11}$
	CsCu <sub>2</sub> I <sub>3</sub>	0.265	0.022	10.3	24	$1.2 \times 10^{11}$
0D	PbS QDs	0.97	0.46	60	$0.49 \times 10^{-3}$	$2.1 \times 10^{12}$
	PbS QD/MoS <sub>2</sub> /WSe <sub>2</sub>	0.785	0.76	$\approx 100$	0.05	$5.15 \times 10^{11}$
	PbS QD/Si	1.28	–	31	0.0025	$8.8 \times 10^{10}$
	CdSe QDs	0.36~1.31	$8.3 \times 10^3$	$\approx 60$	90	$4.2 \times 10^{17}$
	CsPbBr <sub>3</sub> QDs	0.514	0.14	–	12	$7.0 \times 10^{11}$
	CsPbBr <sub>3</sub> QDs	0.405	10.1	$6.4 \times 10^3$	–	$9.35 \times 10^{13}$
	CsPbI <sub>3</sub> QDs	0.450	0.105	–	–	$5 \times 10^{13}$
	Si:PbS QDs	1.540	0.264	21.4	0.002	$1.47 \times 10^{11}$

**Metal-organic frameworks (MOFs):** MOFs' inherent light-harvesting capabilities and potential for customization render them compelling contenders for photodetection applications. The incorporation of MOFs into photodetectors holds the promise of augmenting light absorption, facilitating charge separation, enhancing selectivity, and tailoring the photoresponse. While 2D MOFs and single crystal MOFs have demonstrated considerable potential in photodetection [94],

[99]–[103], their 3D counterparts have encountered inherent limitations. These limitations primarily involve restricted carrier mobility and sluggish charge transport dynamics, impeding their ability to swiftly respond to photogenerated carriers [46], [47], [50]. However, the synthesis challenges associated with single crystal MOFs, the production of high-quality large-area 2D MOF films, and their incorporation into device architectures have hindered their widespread adoption. These constraints have motivated us to explore composite systems to leverage the strengths of 3D MOFs while addressing their weaknesses. In this study, for the first time, we delve into a groundbreaking exploration of photodetectors based on innovative MOF nanocomposites with CNFs.

## **2.4 Synthesis Strategies**

### **2.4.1 MOFs Nanoparticles Synthesis Strategies**

MOF crystalline particles can be produced across various scales, ranging from macro to micro and even down to the nanoscale. When MOF particles are synthesized at the nanoscale, they exhibit markedly improved properties compared to their larger counterparts. These enhancements include controllable diffusion kinetics, a higher proportion of exposed active sites, and effective confinement of redox centers [180]. In most instances, MOFs are typically created through solvo(hydro)thermal processes conducted at elevated temperatures and pressures [180], [181]. This traditional approach represents the primary method for MOF synthesis. However, alternative synthetic techniques, including microwave-assisted, sonochemical, mechanochemical, microfluidic, and continuous flow methods, have emerged in recent years to synthesize MOFs in nano-scale [180]–[183].

In contrast to conventional heating methods, microwave-assisted synthesis allows for significantly reduced heating times (mere minutes) by applying more concentrated and localized energy, leading to enhanced nucleation and consequently smaller particle sizes [184]. Similarly, ultrasound-assisted synthesis harnesses acoustic cavitation to generate localized high temperature and pressure, resulting in improved nucleation, controlled particle morphology, and phase selectivity [184]. However, to date, microwave- and ultrasound-assisted methods are only applicable for a limited number of MOFs.

Mechanochemical synthesis involves the use of mechanical grinding (mechanical force) to supply the necessary energy for MOF formation. This solvent-free approach offers an environmentally friendly and scalable alternative to MOF preparation. However, achieving precise control over crystal size and shape proves challenging, and irreproducibility remains a significant drawback of mechanochemical routes [185].

Continuous flow processes for MOF synthesis hold promise for scaling up production and improving efficiency [186]. Nevertheless, substantial limitations and challenges persist in obtaining MOFs with ideal properties, and successful synthesis examples remain limited for certain MOF types. Achieving success in this endeavor necessitates collaborative efforts between chemists and engineers, and ongoing research is dedicated to this objective [180].

For our research, we will utilize a sonochemical method to synthesize ZIF-8. There is limited number of studies that have explored the synthesis of ZIF-8 nanoparticles through sonochemical methods, as evidenced by the existing literature [187], [188].

#### **2.4.2 MOFs/MWCNTs and MOF/CNFs Nanocomposites Fabrication Strategies**

A composite is formed by combining a minimum of two elements that collectively contribute to the overall system while maintaining their distinct identities [48]. Carbon-based materials have

garnered extensive applications due to their remarkable attributes, including high mechanical and elastic strength, exceptional chemical and thermal resistance, distinctive electronic and optical properties, low weight, minimal toxicity, and, in some cases, affordability (low cost) [189]–[191]. Consequently, the integration of MOFs with carbon-based materials holds significant significance, not only for addressing the limitations of MOFs and transforming them into user-friendly configurations but also for ushering in a host of innovative functionalities. These functionalities encompass improved stabilities, enhanced electrical conductivities, superior optoelectric properties, and template effects, among others [192].

In reality, MOFs have the capability to either form on surface of carbonaceous frameworks, become integrated into carbon matrices during their synthesis process, or directly blend with carbon materials, and vice versa. Consequently, we categorize the preparation methods into two groups: in situ synthesis approaches (MOFs synthesized in the presence of carbon-based materials, following the same strategies explained in section 2.4.1 for MOF nanoparticle synthesis) and ex situ synthesis approaches (involving the integration of the pre-synthesized MOFs, following the same strategies explained in section 2.4.1 for MOF nanoparticle synthesis, with carbon-based materials through direct mixing). In situ synthesis represents a time- and resource-efficient strategy suitable for the fabrication of nearly all types of MOF–carbon composites. Typically, carbon-based materials are introduced into a solution containing thoroughly dissolved MOF precursors, followed by carrying out hydrothermal reactions under the same conditions as those used for pure MOF synthesis [192], [193].

In much of the existing literature, the fabrication of MOFs/MWCNTs composites has typically involved the use of functionalized CNTs, featuring functional groups like carboxyl groups on their surfaces. This approach serves to enhance their dispersibility in polar solvents and facilitate the

anchoring of metal nodes [194], [195]. However, it should be mentioned that functionalization can lead to significant alterations in the properties of MWCNTs, including the loss of their original hydrophobic characteristics, which may not be desirable for certain applications. Consequently, the utilization of bare MWCNTs, known for their exceptional hydrophobicity, presents a promising avenue for enhancing the overall hydrophobicity of MOFs/MWCNTs composites. Therefore, in our first and second project, our focus shifts to the synergistic integration of MOFs and bare MWCNTs in a novel class of nanocomposites for gas sensing application.

While there have been previous investigations into the development of composites involving MOFs and MWCNTs, the synthesis of MOFs with CNFs remains unreported. In our third project, our focus shifts towards the synergistic integration of MOFs and CNFs, pioneering a groundbreaking nanocomposite category for the very first time. This endeavor aims to address the individual limitations of MOFs and CNFs, ultimately leading to the creation of an enhanced nanocomposite material for optoelectronic applications.

## **2.5 MOFs Thin Film Fabrication Methods**

Various approaches have been documented in the literature for the production of thin films or membranes composed of MOFs. These methodologies can be classified into the following categories: (1) direct growth, (2) layer-by-layer growth, (3) secondary growth, and (4) chemical solution deposition [196].

**Direct growth** techniques rely on the substrate's immersion in reaction solutions containing metal salts and linkers, either through the application of microwave-assisted heating or by using a preheated reaction mixture. In both approaches, it has been noted that the creation of continuous

thin films on bare substrates is hindered by poor heterogeneous nucleation. As a result, chemical modifications of the supports are deemed essential to achieve high-quality films [196].

**The layer-by-layer (LBL) approach** for the growth of MOF thin films at RT entails a series of cycles in which the substrate is immersed successively in solutions of the metal salt and solutions of the organic linker. Following each deposition step, the substrate is rinsed with an appropriate solvent to eliminate any unreacted or physisorbed reaction components. In comparison to direct growth, the LBL method results in the formation of homogeneous, nanoscale films with precise control over orientation and thickness at each individual step. However, it should be noted that the LBL route necessitates the pre-functionalization of substrates with self-assembled monolayers, a task that is nontrivial. Furthermore, the repetitive immersion and washing cycles constitute a time-consuming process [196].

**Secondary or seeded growth** offers improved control over the thickness and orientation of the film, compared to direct growth. In the process of secondary growth, a seed layer is applied to the substrate, and the seeding technique that offers the greatest versatility is typically spin- or dip-coating. Subsequently, the seeded substrate is submerged in a reaction solution containing the specific MOF, and thin films or membranes are generated on the seeded surface using a procedure akin to direct growth. The presence of pre-existing nuclei on the supporting surface serves to eliminate the impact of surface chemistry. Secondary growth is more commonly employed for the fabrication of membranes, as direct growth tends to result in inadequate coverage of crystallites on uncoated substrates [196].

**The chemical solution deposition route** involves the utilization of stable dispersions of nanocrystals, which are applied to substrates through techniques such as spin-coating, dip-coating, drop-casting, or spraying. Films of varying thickness can be generated through multiple deposition

steps. This approach is characterized by its simplicity, speed, and cost-effectiveness. Due to its affordability and potential for large-area processing, this technique is also employed within the industrial sector [196]. Hence, in this study, the spray coating method is being considered for use. For the fabrication of ZIF-8 thin films, various methods including direct growth [197], [198], secondary growth [197], [199], and chemical solution deposition route such as dip-coating [200], [201] have been reported in the literature. However, the utilization of the spray method for the fabrication of ZIF-8 thin films has not been reported.

## **2.6 MOF-based Chemiresistive Sensors for Methane and Acetone Detection and their Mechanism**

In general, gas sensing methods based on MOFs encompass optical techniques (e.g., Chromism and luminescence), mechanical approaches (including QCM, SAW, and microcantilevers), magnetism, and electrical sensing (such as impedance, capacitive, and resistive techniques) as depicted in **Figure 2.1**[139]. Among these, chemiresistive sensors stand out as the simplest and most sought-after devices due to their cost-effectiveness and ease of miniaturization. They have been extensively explored with nanomaterials like metal oxides [202]. However, the utilization of MOFs as the sensing material in chemiresistive sensors has only recently garnered attention, primarily owing to the limited availability of MOFs with adequate electrical conductivity. The development of novel synthetic methods for electroconductive MOFs (EC-MOFs) and electroconductive MOF composites, which exhibit both porosity and electrical conductivity, has paved the way for the initial applications of these materials in chemiresistive sensors [203]–[206]. Nevertheless, there have been no reports on the use of MOF resistive-based sensors for the detection of CH<sub>4</sub> and acetone.

The mechanism of chemiresistive MOF-based sensors is primarily ascribed to the adsorption of gas molecules by the functional material, leading to electron and hole transfer, or surface reactions of gas molecules with the functional material, culminating in alterations in the resistance (or conductance) of the sensing materials [139]. Despite this, there is a lack of studies explaining the selectivity mechanism in MOFs-based resistive sensors. In this study, we provide the first comprehensive explanation of the sensing mechanism for MOFs/MWCNTs nanocomposite-based resistive gas sensors, particularly in their selective response to different analytes, as detailed in Chapter 4.

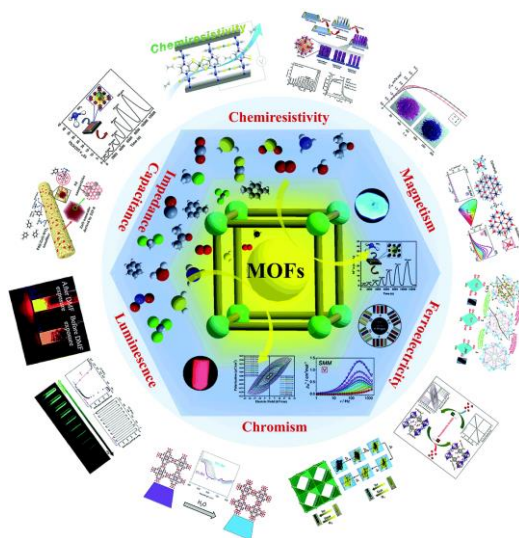


**Figure 2.1** Sensing based on different properties of MOFs (reproduced with permission from ref [139], Copyright (2023) Royal Society of Chemistry).

## 2.7 Light Detection Mechanisms in Photodetectors

Photodetectors can be classified into three types based on device structure and working mechanism: photoconductors, photodiodes, and phototransistors. The schematics of these device architectures are illustrated in Fig. 2a–c [207]. In this study we used the photoresistor device structure.

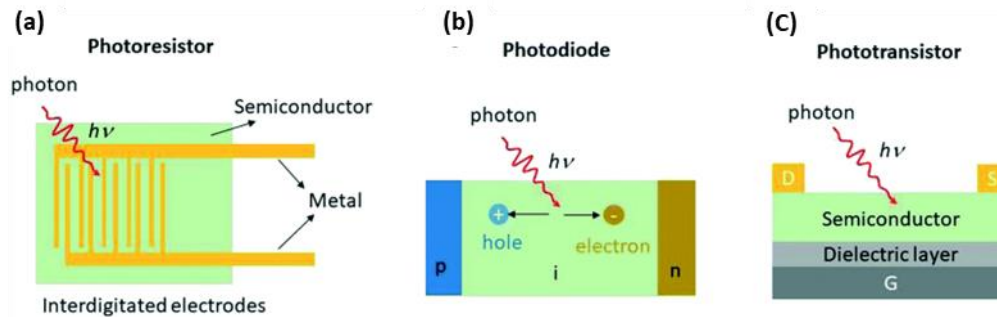


**Figure 2.2** Schematic illustrations of a typical (a) photoconductor, (b) photodiode, and (c) phototransistor (reproduced with permission from ref [207], Copyright (2023) Royal Society of Chemistry).

However, we can categorize photodetectors based on their mechanisms for light detection (working mechanism) [208]:

1. **Photoconductive effect:** Photoconductivity is a well-known optical and electrical phenomenon observed in semiconductors, characterized by an increase in electrical conductivity upon the absorption of light radiation. This effect involves several mechanisms, including the absorption of incident light, the generation of electron-hole pairs, and carrier transport, occurring successively or simultaneously. To induce excitation, the incident light must possess energy greater than the bandgap of the semiconductor, lifting electrons to the conduction band or exciting impurities within the bandgap, leading to the formation of electron-hole pairs. Photoconductivity serves as the foundation for photodetection operations, with photoconductive detectors commonly crafted from semiconductors [208], [209].
2. **Photovoltaic effect:** In semiconductor solar cells, the photovoltaic effect is harnessed by utilizing a p-n junction rather than a pure semiconductor. The presence of a potential barrier within the p-n junction is essential for this process. When exposed to light with energy

higher than the energy gap ( $E_g$ ) of the semiconductor, electron-hole pairs are generated. These pairs are then separated by the potential barrier, causing electrons and holes to move in opposite directions. This separation results in a potential difference at the two terminals, leading to the creation of electrical power from the incident light. The photovoltaic effect serves as the fundamental mechanism driving the operation of semiconductor solar cells [208], [209].

3. **Photoemission or photoelectric effect:** Photons induce the transition of electrons from a material's conduction band to free electrons in a vacuum or gas. Photoelectric effects occur when photons of higher frequencies, such as X-rays and gamma rays, are radiated. These high-energy photons can release electrons near the atomic nucleus, leading to the ejection of an inner electron. Subsequently, a higher-energy outer electron rapidly fills the vacancy, emitting excess energy and causing the emission of one or more additional electrons—a phenomenon known as the Auger effect. This effect serves as a powerful tool for studying atoms and solid surfaces [209].

Another phenomenon observed at high photon energies is the Compton effect. When photons with energy significantly greater than the binding energy of electrons strike a semiconductor, they undergo scattering. In this elastic collision between the photon and electron, energy and momentum are conserved. The photon loses energy to the excited electron, resulting in a decrease in the photon's energy and an increase in wavelength according to Einstein's relation  $E=hc/\lambda$ . Consequently, the scattered radiation is observed to consist of two wavelengths: the original wavelength and an increased wavelength [208], [209].

4. **Thermal effect:** Photons cause the transition of electrons to mid-gap states, followed by their return to lower bands, initiating the generation of phonons and subsequently leading to the production of heat.
5. **Polarization effect:** Photons can alter the polarization states of compatible materials, potentially causing shifts in the index of refraction or triggering other polarization-related effects.
6. **Photochemical effect:** Photons initiate a chemical transformation within a material.

### 2.7.1 Types of Photoconductivity

Photoconductivity characteristics can be categorized into intrinsic and extrinsic photoconductivity based on the mechanism. Intrinsic photoconductivity originates from the generation of mobile charge carriers due to the absorption of electromagnetic radiation in pure materials. This transition occurs across the primary band gap ( $E_g$ ), creating electrons and holes as photocarriers [210]. In extrinsic semiconductors, the existence of impurity creates energy levels within the band gap very close to the valence band, which are called acceptor level ( $E_a$ ). This shifts the effective Fermi level to a point about halfway between the acceptor levels and the valence band to show a p-type semiconductor behavior [211]. Extrinsic photoconductivity involves absorption from (or to) impurity sites within the band gap. Electrons from impurity atoms are excited to the conduction band (CB), leaving ionized atoms behind and generating photocarriers in the CB or valence band (VB). These excited electrons, or photocarriers, are mobile and contribute to the conduction process. The schematic illustration in Fig. 2.3 depicts the transition levels of intrinsic and extrinsic photoconductivity processes, indicating the transition from donor level to the CB and from the VB to acceptor level as 1 and 2, respectively [210].

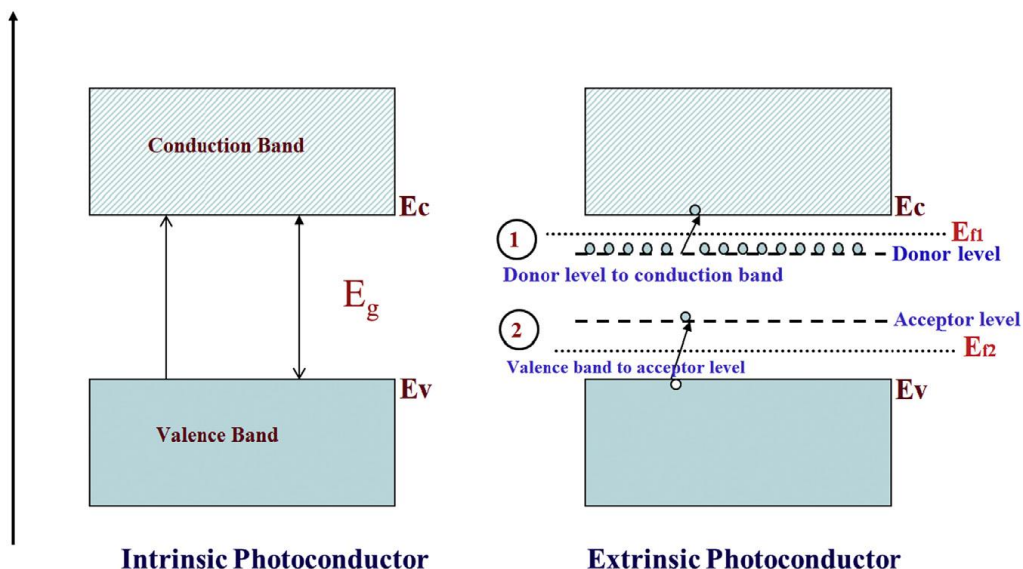


**Figure 2.3** Transition level in intrinsic and extrinsic photoconductivity process (reproduced with permission from ref [210], Copyright (2023) Elsevier Books).

In this chapter, we have provided an overview of nanomaterials used in  $\text{CH}_4$  and acetone detection, as well as photodetection, emphasizing associated challenges. In the following chapters, we address these challenges by selecting ZIF-8 (within the MOF class) as our sensing layer of chemiresistive sensor due to its low water affinity and stability in ambient conditions. For the first time, we enhanced its chemical interaction, electrical conductivity, and photoelectric properties by creating nanocomposites with bare MWCNTs and CNFs, for use in gas sensing and photodetector applications, respectively. Our composite approach aims to reduce the electronic bandgap and activation energy of ZIF-8 through the random incorporation of MWCNTs and CNFs.

Moreover, among the discussed strategies for fabricating MOFs composites and producing MOFs thin films, we opt for the in-situ sonochemical synthesis method to create ZIF-8, ZIF-8/MWCNTs and ZIF-8/CNFs nanocomposites. To fabricate thin films of these nanomaterials on IDE and QCM

chips for resistive sensor, photoresistor-based PD, and QCM-based sensors, we employ the spray coating method, which are explained in detail in the following chapter.

## Chapter 3 : Experimental Method

The contents of this chapter have been published in the experimental section of entitled papers:

- “MOF/MWCNT–Nanocomposite Manipulates High Selectivity to Gas via Different Adsorption Sites with Varying Electron Affinity: A Study in Methane Detection in Parts-per-Billion”, ACS sensors, 7, 3846-3856, <https://doi.org/10.1021/acssensors.2c01796>.
- “ZIF-8/MWCNT-Nanocomposite Based-Resistive Sensor for Highly Selective Detection of Acetone in Parts-Per-Billion: Potential Noninvasive Diagnosis of Diabetes”. Sensors and Actuators B: Chemical, 2023, 393, 134197, <https://doi.org/10.1016/j.snb.2023.134197>.
- “Eco-friendly and High-Performance Photodetector based on Bandgap-Engineered MOFs/CNFs Nanocomposites for Violet Light Detection”, Advanced optical material, submitted.

### 3.1 Material Synthesis

#### 3.1.1 Synthesis of ZIF-8

To synthesize pure ZIF-8 nanoparticles, 83 mg of 2-Methylimidazole (Hmim) ( $C_4H_6N_2$ , Sigma Aldrich,  $\geq 99\%$ ), and 93 mg of zinc acetate dihydrate (98% VWR) were separately dissolved in 16 mL and 5 mL of N, N dimethylformamide (DMF, 99.8%, VWR), respectively. The precursor solutions were mixed, and the vial was set to the probe of an ultra-sonic generator (100 W, QSonica Q500, USA) at RT (around 25 °C) for 7 minutes till we get a white suspension. Subsequently, the ZIF-8 is separated from the reaction mixture by centrifugation (6000 rpm, Corning C6755) and washed with ethanol (30 mL).

### 3.1.2 Synthesis of ZIF-8/MWCNTs Nanocomposites

The ZIF-8/MWCNTs composite was prepared under the same conditions of ZIF-8 synthesis procedure with the addition 10 mg of bare MWCNTs (30-50 nm outer diameter, 10-20  $\mu\text{m}$  long and purity > 95wt%, Cheap Tubes) in 10 ml DMF into the precursor solutions. Instead of following the reported studied in using functionalized-MWCNTs for making MOF/MWCNTs nanocomposite, for the first time, bare MWCNTs have been used in making ZIF-8/MWCNTs nanocomposite to engineer our nanocomposite selectivity and render an enhancement in overall hydrophobicity.

Composites of ZIF-8 with 2.5, 5, 10, and 15 wt% of MWCNTs were synthesized. However, at 2.5 wt%, the IDE chip coated with this composite showed no conductivity, rendering it unsuitable as a sensing layer for a resistive sensor. Conversely, at 15 wt% of MWCNTs, the quantity exceeded the composite's capacity, leaving excess MWCNTs in the solution after centrifugation. As a result, this formulation was excluded from our sensing experiments. Therefore, we focused our experiments on composites containing 5 and 10 wt% of MWCNTs.

### 3.1.3 Synthesis of ZIF-8/CNFs Nanocomposites

To synthesize pure ZIF-8/CNFs nanoparticles, 200 mg of Hmim ( $\text{C}_4\text{H}_6\text{N}_2$ , Sigma Aldrich,  $\geq 99\%$ ), 100 mg of zinc acetate dihydrate (98% VWR), 33 mg of bare CNFs (PR-19-XT-PS, tubular fiber, average diameter of about 150 nm,  $\geq 98\text{wt}\%$ , Pyrograf Products, Inc.), were separately dissolved in 25 mL and 7 mL of DMF (99.8%, VWR), and 10 mL ethanol (99.9%, VWR) respectively. The precursor solutions were mixed, and the vial was set to the probe of an ultrasonic generator (100 W, QSonica Q500, USA) at RT (around 25  $^\circ\text{C}$ ) for 1 minute. Then, the black mixture was transferred to a 50 ml stainless steel autoclave lined with Teflon and heated at 130 $^\circ\text{C}$

for 19 hours. At the end of the reaction time, the reactor left to cool at ambient temperature, and black solution collected. After that, the black solution is separated from the reaction mixture by centrifugation (6000 rpm, Corning C6755) and washed with ethanol (30 mL).

Composites of ZIF-8 with 5, 10, and 15 wt% of CNFs were synthesized. However, at 5 wt%, the IDE chip coated with this composite showed no conductivity and photo responsivity, rendering it unsuitable as a sensing layer for a photodetector. Conversely, at 15 wt% of CNFs, the quantity exceeded the composite's capacity, leaving excess CNFs in the solution after centrifugation. As a result, this formulation was excluded from our sensing experiments. Therefore, we focused our experiments on composites containing 10 wt% of CNFs.

### **3.2 Materials Characterization**

Fourier Transform Infrared Spectroscopy (FTIR, Nicolet Nexus 470, USA) was utilized to identify and analyze the functional groups present in the synthesized materials and investigate their chemical bond vibrations. Raman spectroscopy (Horiba XploRA PLUS, Diode-Pumped Solid-State laser (532 nm), Power 14 mW, USA) was employed to confirm the molecular structures of the samples, providing complementary information to FTIR. X-ray diffraction (XRD, Rigaku Multiflex with X-ray source of Cu K $\alpha$ ) was used to characterize the crystalline structure of the materials. UV-Vis spectrophotometer (Ocean Optics, Flame-S, USA) was used to determine the optical band gap of the materials, providing information on the materials' electronic properties. Field emission scanning electron microscopy (FE-SEM, Quanta 250) was employed to determine the morphology of the materials, providing information on the size of the samples. Nitrogen adsorption/desorption isotherms of the materials were obtained at 77 K by a Micromeritics Tristar II Plus surface area and porosity analyzer instrument equipped with MicroActive for TriStar II Plus Version 2.03 software for calculation and analysis. The Brunauer–Emmett–Teller (BET)

method was used to determine the specific surface area of the samples. Total pore volume was calculated by N<sub>2</sub> uptake at the relative pressure P/P<sub>0</sub> = 0.99. The micropore volume was obtained using the t-plot method of Lippens and de Boer with the adsorption data. Transmission electron microscopy (TEM, Hitachi H7650) was employed to characterize bare MWCNTs.

### 3.2.1 ZIF-8/MWCNTs Characterization

#### 3.2.1.1 FT-IR

The FT-IR spectrum of the synthesized ZIF-8 displayed prominent peaks at 3455, 3135, 2929, 1683, 1589, 1460-1300, 1145, 1300-900, 800-600, and 426 cm<sup>-1</sup> (**Figure 3.1**), which were consistent with previous studies [26–29]. These peaks corresponded to various molecular vibrations, including Hmim's N–H stretching (or the O–H stretching vibration of physically adsorbed water), aromatic C–H asymmetric stretches, the rings aliphatic C–H asymmetric stretches, the C=C stretching mode, the C=N stretching, the entire ring stretching, aromatic C–N stretching mode, the rings in-plane bending, the ring out-of-plane bending, and Zn–N stretching, respectively [27–29]. The inherent hydrophobicity of ZIF-8 can be evident from its FT-IR spectrum band at 3455 cm<sup>-1</sup> (attributing to the N–H stretching vibration of the residual Hmim on the outer surface of ZIF-8 and the O–H stretching vibration of physically adsorbed water) which is weak in compare to other kinds of MOFs [52]. The ZIF-8/MWCNT nanocomposite displayed the same FT-IR peaks as ZIF-8, indicating that there were no significant chemical interactions between the ZIF-8 crystals and the MWCNTs (**Figure 3.1**) [213]. However, the intensity of peaks for ZIF-8/MWCNTs has reduced in FT-IR spectrum suggesting the existence of MWCNTs in the nanocomposite. Bare MWCNTs only exhibited a weak peak at 1638 cm<sup>-1</sup>, which was associated with the presence of aromatic C=C groups, as previously reported [30–32]. Additionally, the

absence of any other peaks in the MWCNTs confirms that they do not have any functional groups, confirming their bare nature. The FT-IR diagram of the MWCNTs and ZIF-8 MWCNTs nanocomposite reveals a rise in transmittance with an increase in wavenumber. This phenomenon is attributed to their black color, which has a high degree of light absorption, and possesses light-blocking characteristics. As wavenumber increases, the energy of the infrared radiation decreases. The rise in transmittance could be indicative of the material's ability to allow more infrared radiation to pass through at higher wavenumbers.

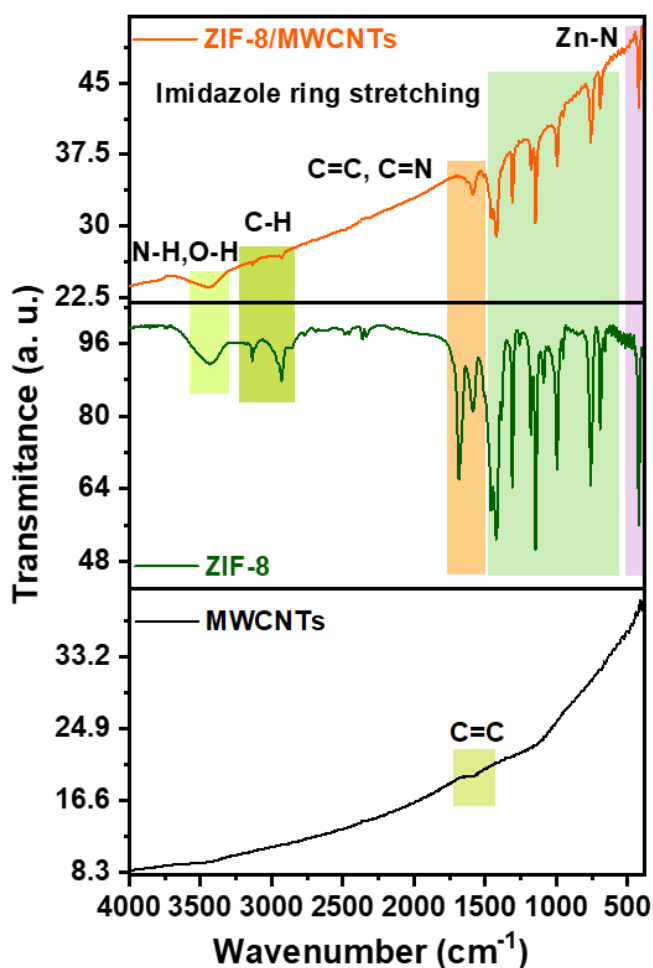


**Figure 3.1** FT-IR spectra of MWCNTs (black), ZIF-8 (green) and ZIF-8/MWCNTs nanocomposite (orange) in the wavenumber range of 4000–400  $\text{cm}^{-1}$  with a spectral resolution of 4  $\text{cm}^{-1}$ .

### 3.2.1.2 Raman

The major Raman peaks of ZIF-8 were observed at 684, 835, 949, 1023, 1146, 1186, 1312, 1385, 1459, and 1509  $\text{cm}^{-1}$ , corresponding to  $\delta$  H (out of plane), bending C–H (out of plane) (C4–C5), bending C–H (out of plane) (C2–H), C5–N stretching vibration, C5–N stretching vibration, N–H wag,  $-\text{CH}_3$  symmetry deformation vibration, C–H bending of methyl, stretching vibration of C2–N1 and C5–N1, respectively (**Figure 3.2**) [33–35]. These Raman peaks agree with the literature [33–37]. MWCNTs exhibited Raman peaks at 1575  $\text{cm}^{-1}$  (G band) and 1343  $\text{cm}^{-1}$  (D band), corresponding to the in-plane vibration of the C–C bond and disorder in the carbon crystal structure or other structural damage, respectively [36,37]. In the ZIF-8/MWCNT nanocomposite, all the characteristic Raman peaks of ZIF-8 and MWCNTs were observed, confirming no chemical interaction during composite formation. The G band of the nanocomposite was shifted compared to pure MWCNTs, suggesting the formation of the ZIF-8/MWCNT nanocomposite. Typically,  $I_D/I_G$  ratio in the Raman spectrum represents defect density in MWCNTs structures; in our case we obtained 0.87 for bare MWCNTs and 0.92 for ZIF-8/MWCNTs, respectively (**Figure 3.2**). These obtained values of  $I_D/I_G$  suggest the presence of defect sites in our bare MWCNTs. Such defects are expected to induce metallic to semiconducting transitions resulting in complex conductance variations.

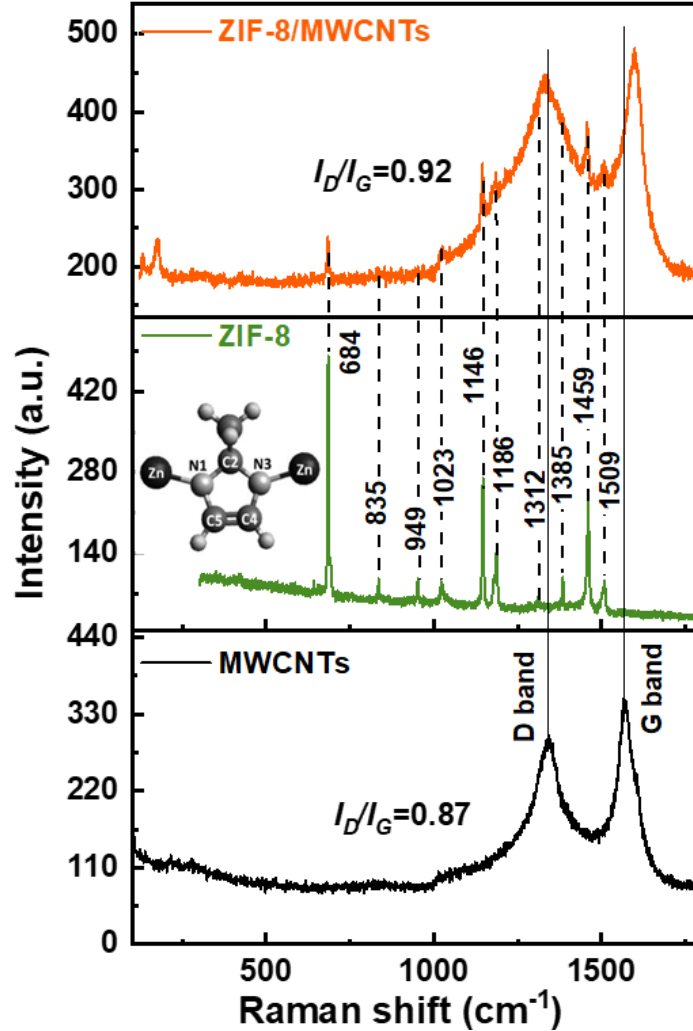


**Figure 3.2** Raman spectra of MWCNTs (black), ZIF-8 (green) and ZIF-8/MWCNTs nanocomposite (orange) in the wavenumber range of 1600 to 180  $\text{cm}^{-1}$ .

### 3.2.1.3 XRD

The XRD pattern of ZIF-8 is consistent with previous literature [26–29], with the main peaks observed at  $2\theta = 7.74, 10.63, 13, 15, 16.8, 18.5, 22.5, 24.9, 27, 30, 31, 32, 32.9$  and  $35.4^\circ$ , corresponding to the (110), (200), (211), (220), (310), (222), (411), (332), (422), (431), (440), (433), (442), and (532) planes, respectively (**Figure 3.3**) [53]. Notably, upon the introduction of MWCNTs into the ZIF-8, the XRD pattern remains comparable to that of pure ZIF-8, indicating that the crystalline structure of the ZIF-8 is successfully maintained. However, the intensity of

peaks for ZIF-8/MWCNTs has increased in XRD pattern suggesting an enhancement in the crystallinity in the nanocomposite. The XRD pattern of MWCNTs displays insignificant peaks at  $2\theta = 26.32$  and  $44.77^\circ$  when compared to the prominent peaks of ZIF-8.

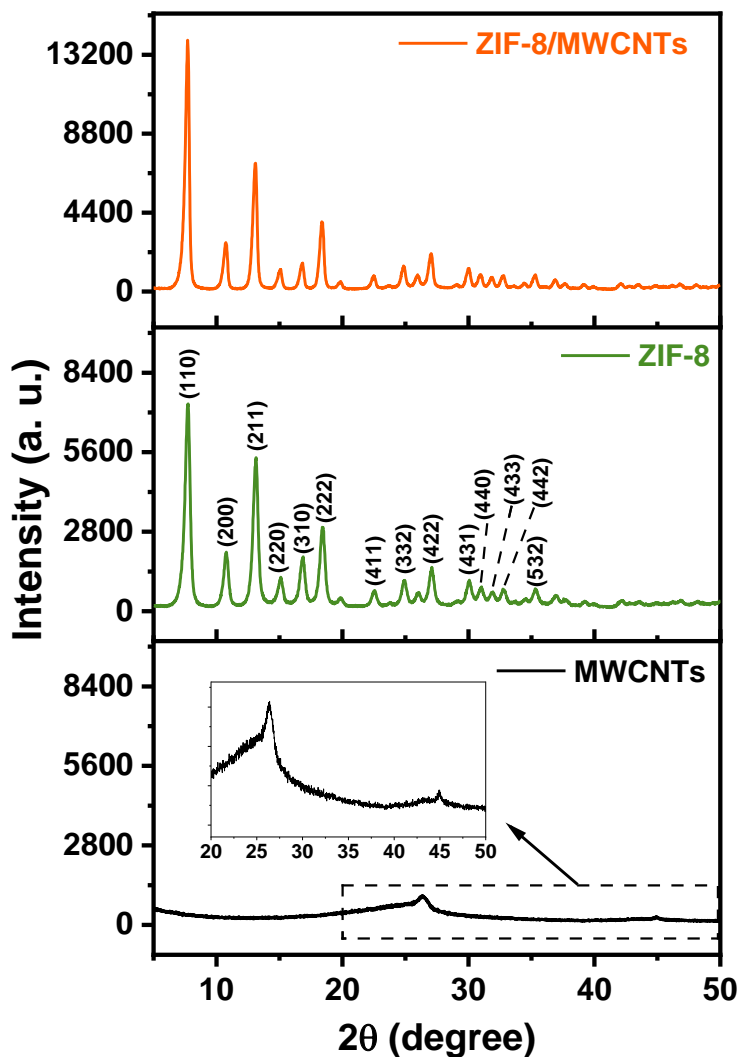


**Figure 3.3** XRD patterns of MWCNTs (black), ZIF-8 (green) and ZIF-8/MWCNTs nanocomposite (orange).

### 3.2.1.4 UV-vis

The UV-Vis absorption spectra of bare MWCNTs, ZIF-8 and ZIF-8/MWCNTs nanocomposite (**Figure 3.4**) reveal a strong peak at  $\sim 274$  nm due to the presence of conjugated bonding electron

systems ( $\pi$ - $\pi^*$  and  $\sigma$ - $\sigma^*$  transition), and a relatively weak characteristic peak at 380 nm related to nonbonding electron system ( $n$ - $\pi^*$  and  $n$ - $\sigma^*$  transition) [222]. For ZIF-8/MWCNTs nanocomposite, the peak at 274 nm is slightly shifted to 270 nm indicating the presence of  $\pi$ - $\pi^*$  transition in the composite after the incorporation of MWCNTs with ZIF-8 to form ZIF-8/MWCNTs nanocomposite via  $\pi$ - $\pi$  interaction. This interaction essentially originated between the Hmim ligands in ZIF-8 and the benzene ring structure in MWCNTs, causing charge transfer from ZIF-8 to the MWCNTs [223].

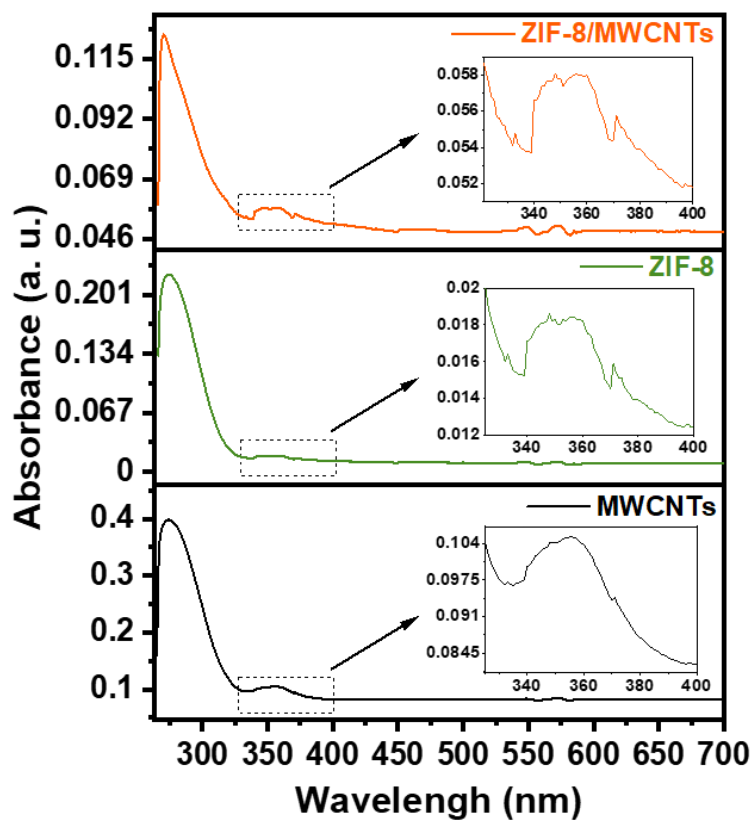


**Figure 3.4** UV-Vis absorption spectra of MWCNTs (black), ZIF-8 (green) and ZIF-8/MWCNTs nanocomposite (orange).

### 3.2.1.5 BET

Prior to the adsorption analysis, ZIF-8 and ZIF-8/MWCNT nanocomposite materials underwent degassing at a temperature of 90°C for a duration of 24 hours. Subsequently, the porous structure of the materials was assessed by conducting N<sub>2</sub> adsorption and desorption experiments within the range of  $P/P_0 = 0.01-0.99$ . The N<sub>2</sub> sorption isotherms of the samples are presented in **Figure 3.5**. According to the IUPAC classifications [224], both samples exhibited a combination of type I and type IV isotherm behaviors, accompanied by a small hysteresis loop at relatively high pressures (**Figure 3.5**). This observation indicates the predominance of microporous characteristics with minor mesopores. The BET surface area, total pore volume, t-plot micropore volume, and average pore width for ZIF-8 and ZIF-8/MWCNT composite are calculated by using the obtained adsorption data and presented in **Table 3.1**. After incorporation of bare-MWCNTs with ZIF-8, all surface properties and porosity data of the ZIF-8/MWCNTs nanocomposite increased compared to the pure ZIF-8.

**Table 3.1** Surface properties and porosity data of ZIF-8 and ZIF-8/MWCNTs nanocomposite.

	<b>BET surface area (m<sup>2</sup>/g)</b>	<b>Single-point total pore volume at <math>P/P_0 = 0.99</math> (cm<sup>3</sup>/g)</b>	<b>t-plot micropore volume (cm<sup>3</sup>/g)</b>	<b>Average pore width (4V/A by BET) (Å)</b>
<b>ZIF-8</b>	925	0.54	0.42	23.53
<b>ZIF-8/MWCNTs</b>	1175	0.85	0.55	28.76

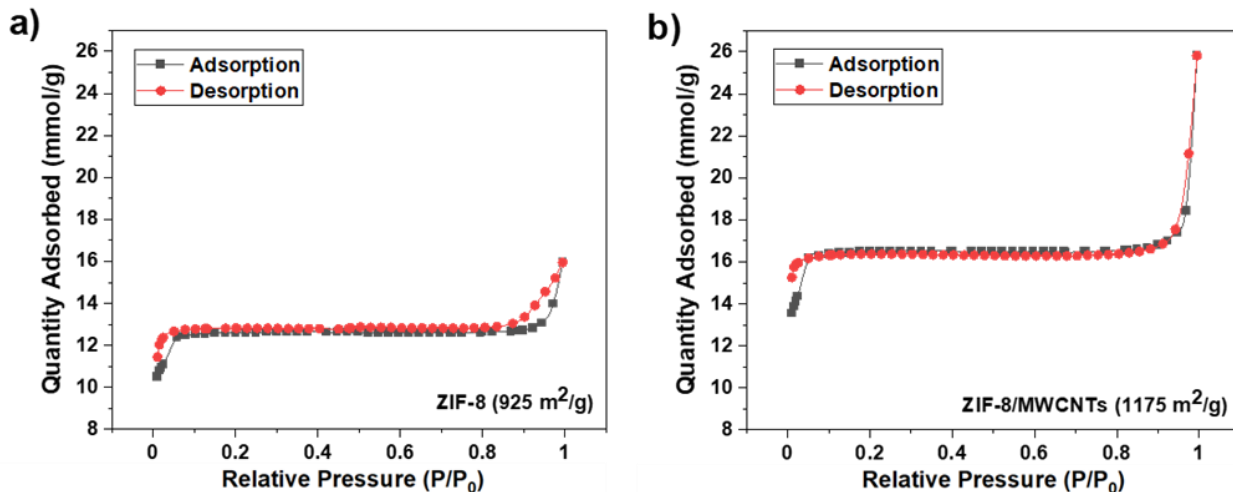


**Figure 3.5** Nitrogen adsorption and desorption isotherms at 77 K for (a) ZIF-8 and (b) ZIF-8/MWCNT nanocomposite.

### 3.2.1.6 SEM/EDX

The morphology of the synthesized ZIF-8/MWCNTs nanocomposite and its elements are investigated by FE-SEM/EDX analysis (**Figure 3.6**, and **Figure 3.7**). FE-SEM images of ZIF-8 and ZIF-8/MWCNTs films show ZIF-8's narrow size distribution with particle sizes ~50 nm (**Figure 3.6a** and **c**) and the existence of MWCNTs strands among ZIF-8 crystals (**Figure 3.6c**). These strands link the crystals to each other and make paths for electron transfer, which gives a semiconductive property to the nanocomposite. Alternatively, we can describe that the MWCNTs could act as nucleation sites for the crystallization of the ZIF-8 forming a dense beaded-network.

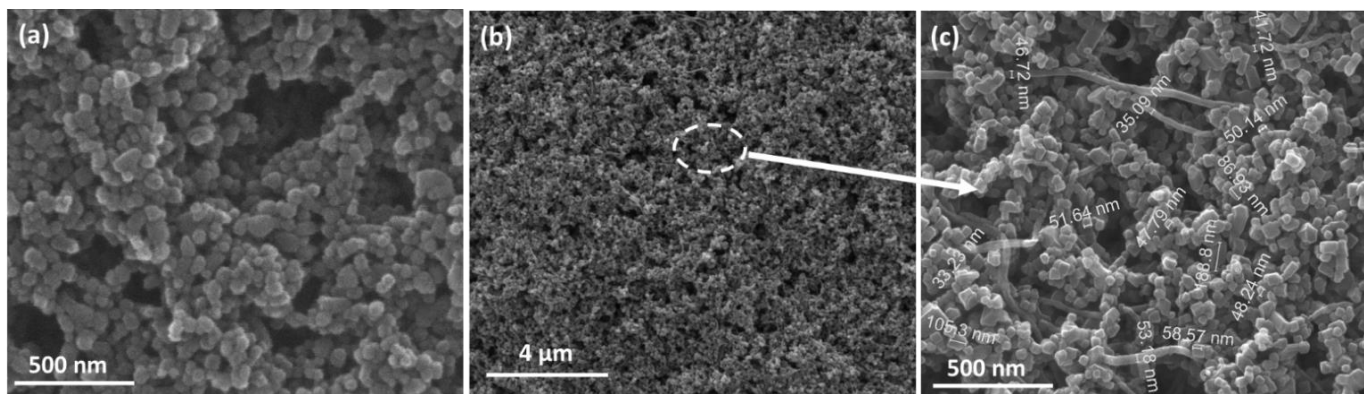


**Figure 3.6** a) FE-SEM image of ZIF-8 film with particle sizes ~50 nm. b) Medium magnification, and c) high magnification FE-SEM images of ZIF-8/MWCNTs film.

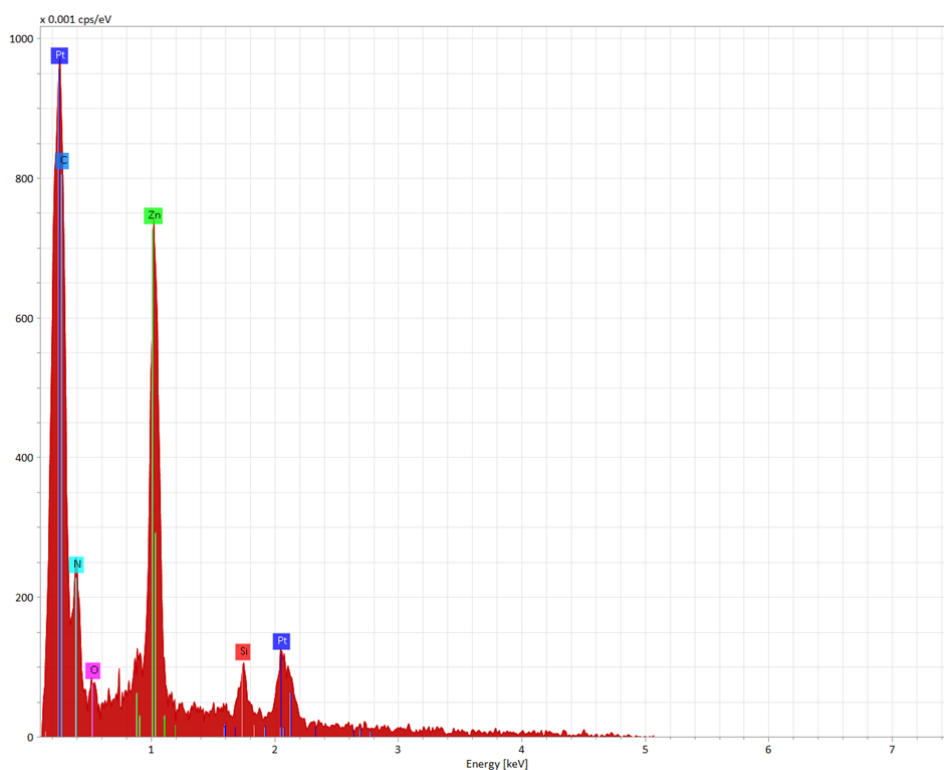


**Figure 3.7** EDX spectrum of ZIF-8/MWCNTs film on the surface of a silicon wafer with platinum coating: elements of carbons (C), nitrogen (N), oxygen (O), Zinc (Zn), silicon (Si) and platinum (Pt) come from ZIF-8's Hmim ligands and MWCNTs, ZIF-8's Hmim ligands, ZIF-8's metal node, the silicon wafer as substrate, and platinum coating on the surface of ZIF-

8/MWCNTs, respectively.

### 3.2.1.6 TEM

MWCNTs are not well-defined electrically due to their structural complexity and variety when compared to SWCNTs. So, conductivity in MWCNTs is quite complex. As was shown and suggested in prior literature [225], [226], intrinsic defects within nanotubes can induce strong modifications in their electronic band structure, provoking metallic to semiconducting transitions. Typically,  $I_D/I_G$  ratio in the Raman spectrum represents defect density in MWCNTs structures; in our case we obtain a value of 0.87 which we report in **Figure 3.2**. This obtained value in our case suggests the presence of defect sites in our used MWCNTs. Such defects are expected to induce metallic to semiconducting transitions resulting in complex conductance variations. As an added proof: TEM-selected area electron diffraction (SAED) and autocorrelation function (ACF) analysis (**Figure 3.8**) of the lattice-plane structures clearly shows the mixed metallic and semiconductive nature of the used MWCNTs in our experiments. So, the semiconducting behavior of the used MWCNTs here can be understood by the fact that our measurement is a result of the overall electrical properties of MWCNTs, which has been further supported by referring to the value of the band gap (2.95 eV) for the used MWCNTs obtained from the Tauc's plots (**Figure 4.2**). Considering our experimental data, heuristically we conclude that the resulting semiconducting behavior of the used MWCNTs plays a significant role in the modulation of electronic bandgap and in turn the complex conductance of our composite resulting in an equivalent series resistance change which we use as a measurand for sensing.

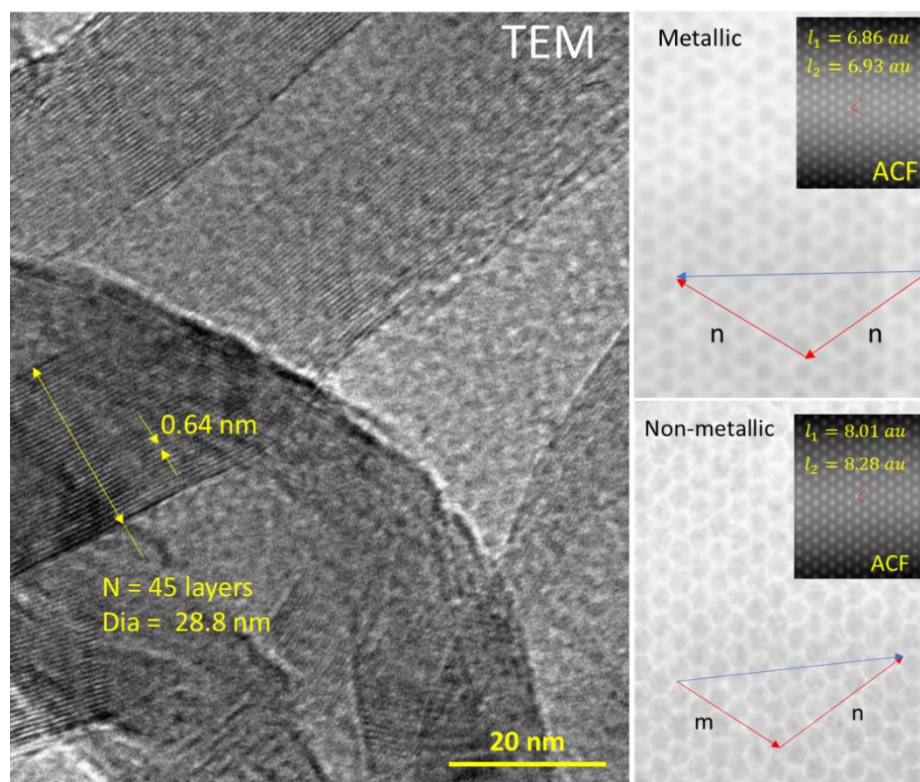


**Figure 3.8** TEM analysis of the MWCNTs shows the layered structure. For the location shown here, the number of layers measured are 45 that accounts for a mean diameter of 28.8 nm with the distance between 2 layers in the order of  $\sim 0.64$  nm. For different MWCNTs at different locations higher resolution imaging shows the lattice planes. Autocorrelation function (ACF) analysis of the lattice-plane structure reveals the mixed metallic and non-metallic nature of the MWCNTs as highlighted in the vector lengths in arbitrary units (au) (insets).

## 3.2.2 ZIF-8/CNFs Characterization

### 3.2.2.1 FT-IR

The FT-IR analysis of the synthesized ZIF-8 revealed distinct peaks at 3455, 3135, 2929, 1683, 1589, 1460-1300, 1145, 1300-900, 800-600, and  $426\text{ cm}^{-1}$  (**Figure 3.9**), aligning with findings from earlier investigations [52], [53], [212], [213]. These peaks corresponded to a range of

molecular vibrations, encompassing Hmim's N–H stretching (or the O–H stretching vibration of physically adsorbed water), asymmetric stretches of aromatic C–H bonds, asymmetric stretches of aliphatic C–H bonds in the rings, the C=C stretching mode, C=N stretching, entire ring stretching, aromatic C–N stretching mode, in-plane bending of the rings, out-of-plane bending of the rings, and Zn–N stretching, respectively [53], [212], [213]. Conversely, bare CNFs exhibited a weak peak at  $1583\text{ cm}^{-1}$ , indicative of the presence of aromatic C=C groups, as reported in prior studies [227]. The FT-IR spectrum of the ZIF-8/CNF nanocomposite mirrored that of ZIF-8, suggesting no chemical interactions between ZIF-8 crystals and CNFs [213].

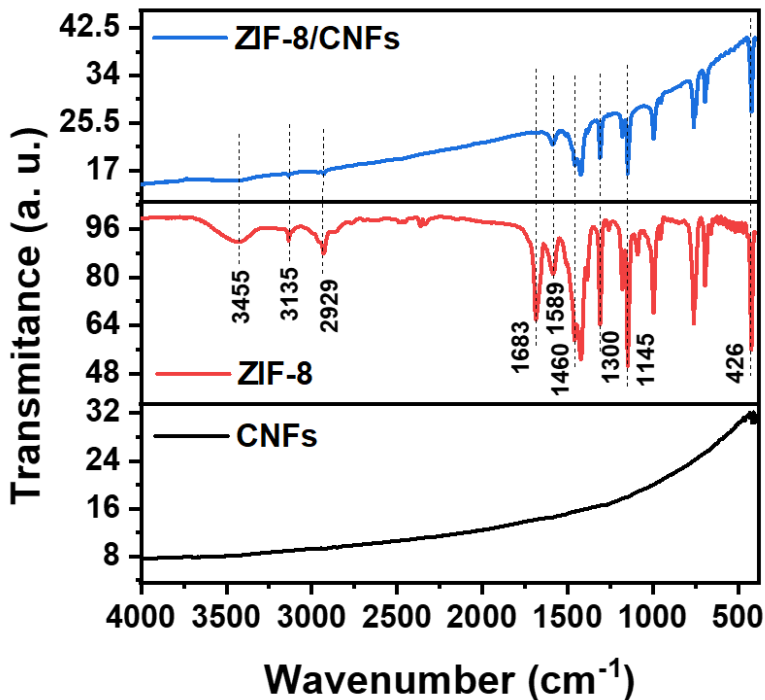


**Figure 3.9** FT-IR spectra of CNFs (black), ZIF-8 (red) and ZIF-8/CNFs nanocomposite (blue), respectively.

### 3.2.2.2 XRD

The XRD pattern of ZIF-8 agrees with prior literature reports [52], [53], [212], [213], revealing prominent peaks at  $2\theta = 7.74, 10.63, 13, 15, 16.8, 18.5, 22.5, 24.9, 27, 30, 31, 32, 32.9,$  and  $35.4^\circ$ ,

corresponding to crystallographic planes (110), (200), (211), (220), (310), (222), (411), (332), (422), (431), (440), (433), (442), and (532) (**Figure 3.10**) [53]. In contrast to the dominant peaks of ZIF-8, the XRD pattern of CNFs presents insignificant peaks at  $2\theta = 26.17$  and  $43.8^\circ$  [228], [229]. The peak at around  $26.17^\circ$  is often associated with the (002) plane, which represents the alignment and ordering of graphene layers within the nanofiber. The peak at  $43.8^\circ$  corresponds to another crystallographic plane, often identified as the (101) plane associated with the stacking arrangement of graphene layers in the nanofiber structure. Upon incorporating CNFs into the ZIF-8 structure, there are weak  $\pi$ - $\pi$  interactions between the ZIF-8 and CNFs resulting in minimal strain or distortion in the ZIF-8 lattice, leading to small shifts in XRD peaks of ZIF-8/CNFs in compared to ZIF-8 alone.

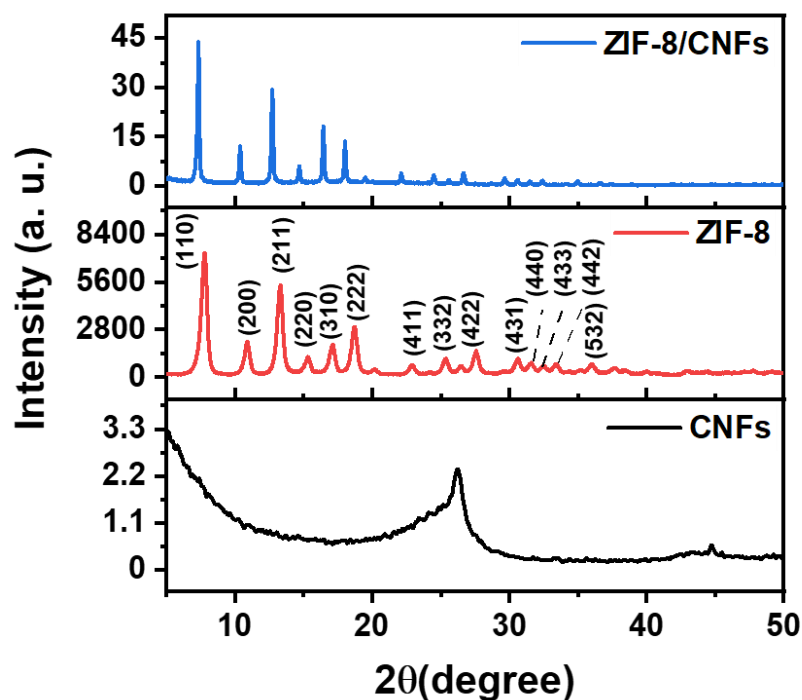


**Figure 3.10** XRD patterns of CNFs (black), ZIF-8 (red) and ZIF-8/CNFs nanocomposite (blue), respectively.

### 3.2.2.3 UV-vis

The UV–Vis absorption spectra of ZIF-8 nanoparticles (**Figure 3.11**) reveal a strong peak at ~274 nm due to the presence of conjugated bonding electron systems ( $\pi$ - $\pi^*$  and  $\sigma$ - $\sigma^*$  transition), and a relatively weak characteristic peak at 380 nm related to nonbonding electron system ( $n$ - $\pi^*$  and  $n$ - $\sigma^*$  transition). [93], [222] For CNFs, an absorption peak at 230 nm corresponds to the  $\pi$ - $\pi^*$  transition of aromatic C=C bonds and a shoulder at 273 nm agrees to the  $n$ - $\pi^*$  transition related to nonbonding electron system.[230] CNFs can also exhibit plasmon resonance broad peaks in the UV-vis spectrum in the range of 300-700 nm. These peaks result from the collective oscillation of free electrons in the conduction band in the CNFs, leading to enhanced light absorption and scattering. In the case of the ZIF-8/CNFs nanocomposite, the characteristic peak of ZIF-8 observed at 274 nm undergoes a notable shift towards 220 nm, which serves as a clear indicator of the emergence of  $\pi$ - $\pi^*$  transitions within the composite. This intriguing transformation is a direct consequence of the incorporation of CNFs into the ZIF-8 framework, facilitated by  $\pi$ - $\pi$  interactions. This interaction is primarily instigated between Hmim ligands within ZIF-8 and the benzene ring structure inherent to CNFs, resulting in a discernible charge transfer from ZIF-8 to CNFs [223].

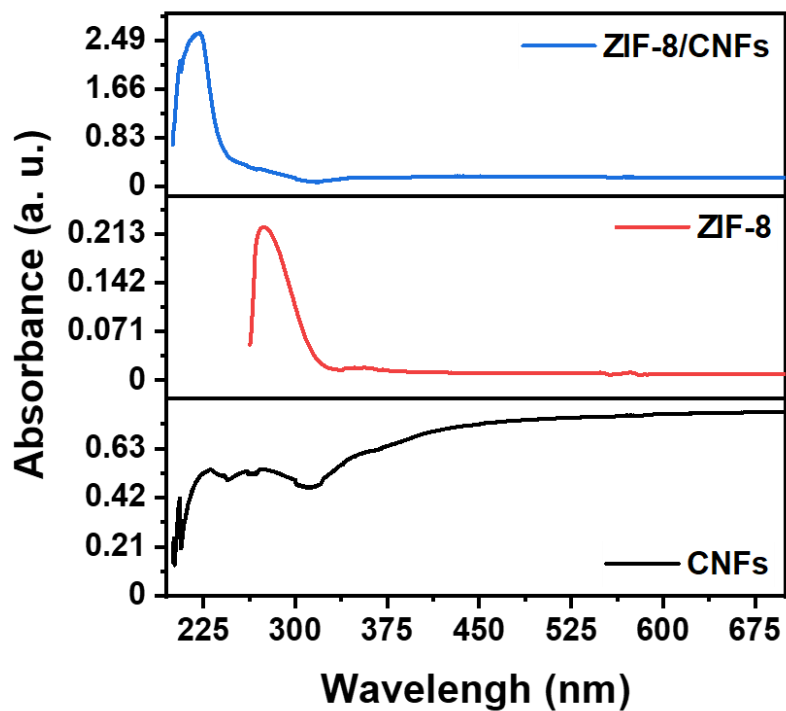


**Figure 3.11** UV–Vis absorption spectra of CNFs (black), ZIF-8 (red) and ZIF-8/CNFs nanocomposite (blue), respectively.

### 3.2.2.4 FE-SEM

The morphological analysis of the synthesized ZIF-8/CNFs nanocomposite thin film and its elements are investigated by FE-SEM/EDX (**Figure 3.11** and **Figure 3.12**). The FE-SEM images reveal a narrow size distribution of ZIF-8 particles, with sizes approximately 50 nm, along with the presence of CNFs strands interwoven among ZIF-8 crystals (**Figure 3.11**). These strands establish connections between the crystals, facilitating paths for electron transfer and conferring a semiconductive property to the nanocomposite.

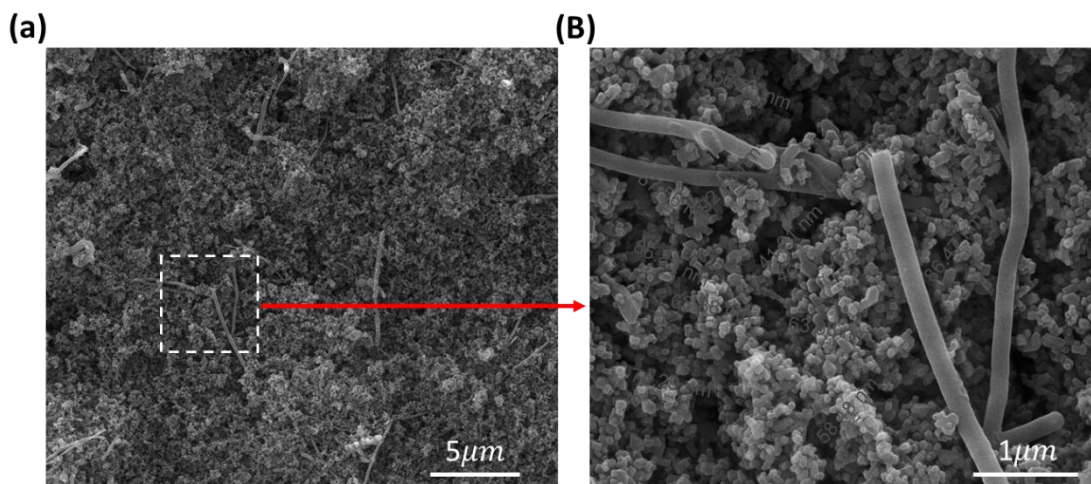


**Figure 3.12** a) Medium magnification, and b) high magnification FE-SEM images of ZIF-8/CNFs film.

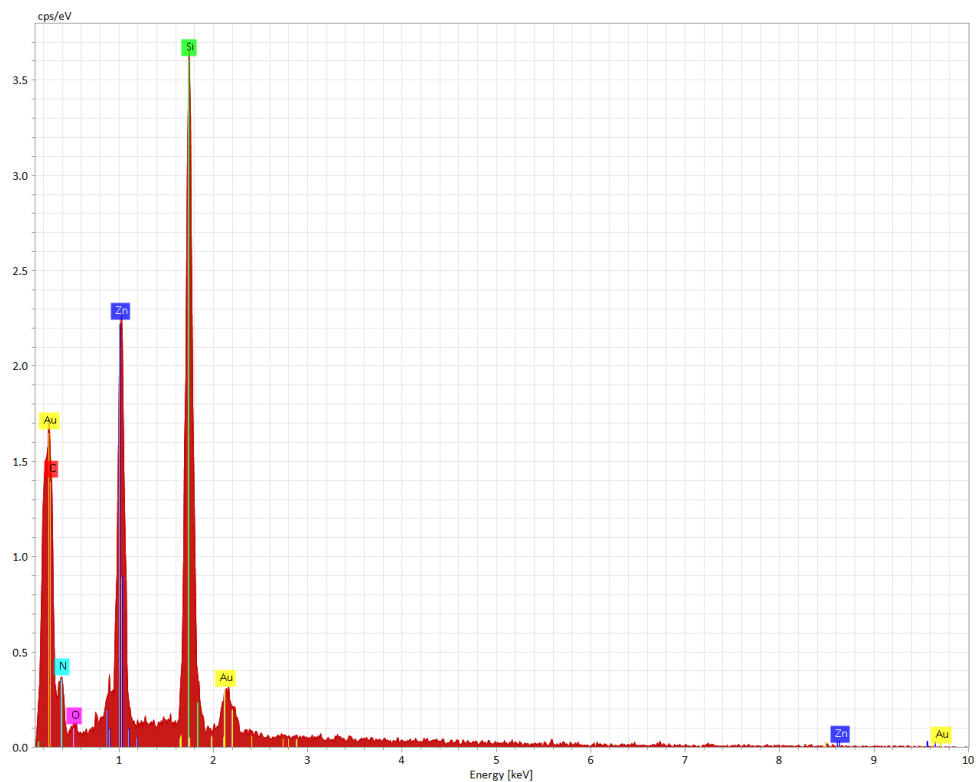


**Figure 3.13** EDX spectrum of ZIF-8/CNFs film on the surface of a silicon wafer with platinum coating: elements of carbons (C), nitrogen (N), oxygen (O), Zinc (Zn), silicon (Si) and gold (Au) come from ZIF-8's Hmim ligands and CNFs, ZIF-8's Hmim ligands, ZIF-8's metal node, the silicon wafer as substrate, and gold coating on the surface of ZIF-8/CNFs, respectively.

### 3.3 Thin Film Fabrication

To create a ZIF-8, ZIF-8/MWCNT, and ZIF-8/CNFs sensing layer on the surface of two types of chips - QCM and IDE chips, spray coating method was utilized. For implementing spray-coating, stable colloidal suspensions of the synthesized materials were obtained by re-dispersing the washed product in ethanol. An airbrush double action kit (Pinkiou SP180KTG, USA) with a nozzle diameter of 0.2 mm and a compressor air tank was used to make a sensing layer of ZIF-8/MWCNTs on the surface of an IDE chip and QCM chip. The QCM chip with a 1-inch diameter obtained from Stanford Research Systems (Sunnyvale, CA, USA), had circular gold electrodes on both sides. An alumina ceramic based-interdigitated electrode (IDE) chip with an overall size of 5 mm\*6 mm\*0.38 mm, consisted of 18 gold fingers (90  $\mu$ m wide, 3800  $\mu$ m long, and a gap of 90  $\mu$ m between fingers) was used (**Figure 3.14**). The spraying rate was optimized to 3 mL/min to obtain a uniform film. The distance between the tip of the nozzle and the substrate was optimized to 20 cm. The deposition time was varied to control the thickness of the sensing layer, resulting in approximately 8  $\mu$ m thick ZIF-8/MWCNT film on IDE chips, and about 400 nm thick ZIF-8 and ZIF-8/MWCNT films on QCM chips measured by an optical profilometer (Zeta<sup>TM</sup>-20).

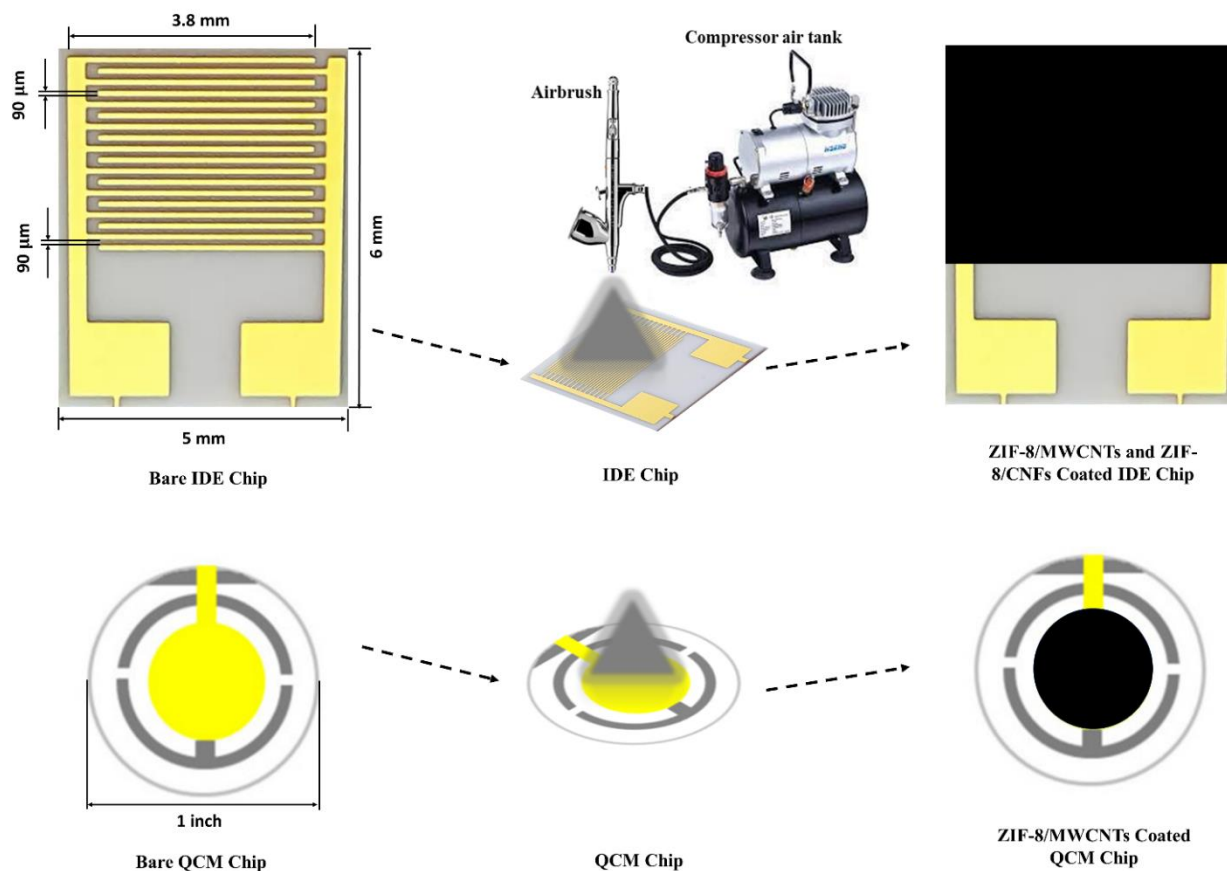


**Figure 3.14** Schematics of the spray-coating set-up with a dual action airbrush, an IDE, and QCM chips.

### 3.4 Experimental Test Setup

#### 3.4.1 IDE and QCM Based Gas Sensor Test Setup and Sensing Experiment:

The gas/vapour sensing tests of ZIF-8/MWCNT-coated chemiresistive sensor were evaluated by using an in-house fabricated flow chamber (**Figure 3.15**). To test the gas/vapour sensing performance of ZIF-8 or ZIF-8/MWCNT-coated QCM sensor and ZIF-8/MWCNT-coated chemiresistive sensor, an experimental setup was prepared as shown in **Figure 3.16**. Dry air was used as the carrier gas to simulate real-world applications. The gas flow rate at each line was regulated using a mass flow controller (MFC, AtoVac GMC1200, Suwon, South Korea) to control

gas concentration. Real-time resonance frequency measurements of the QCM sensors were conducted using a QCM200 system (Stanford Research Systems, Sunnyvale, CA, USA). The measured resonance frequency was converted into  $\Delta F$ , where  $\Delta F = (F_t - F_0)$  is the time-dependent resonance frequency change,  $F_0$  is the baseline resonance frequency in dry-air, and  $F_t$  is the measured resonance frequency under target gas/vapour exposure. For IDE-based chemiresistive sensors, real-time resistance measurements were taken using a digital multimeter (Keysight 34461A, Malaysia). The obtained resistance measurement was converted into a normalized response value ( $\Delta R/R_0$ ) where  $\Delta R$  is the time-dependent resistance change ( $\Delta R = (R_t - R_0)$ ),  $R_0$  is the baseline resistance in dry-air, and  $R_t$  is the measured resistance under target gas/vapour exposure. Prior to measurement, both QCM and IDE-based sensors were stabilized in dry air for two hours at a total flow rate of 100 sccm. All sensing tests were carried out at ambient pressure and RT (25°C). A bubbler filled with double distilled water (DDW) was used to control humidity levels, and an environmental sensor (Thorlabs - TSP01, USA) was employed to monitor temperatures and relative humidity (RH). To precisely control VOCs concentrations (see supporting information), a syringe pump (KDS Legato 100) was used instead of a bubbler.

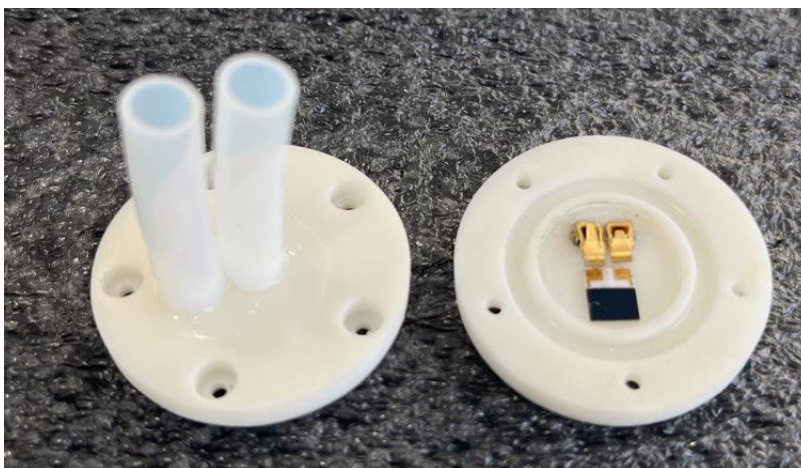


**Figure 3.15** Picture of the in-house fabricated flow chamber with electrode interface.

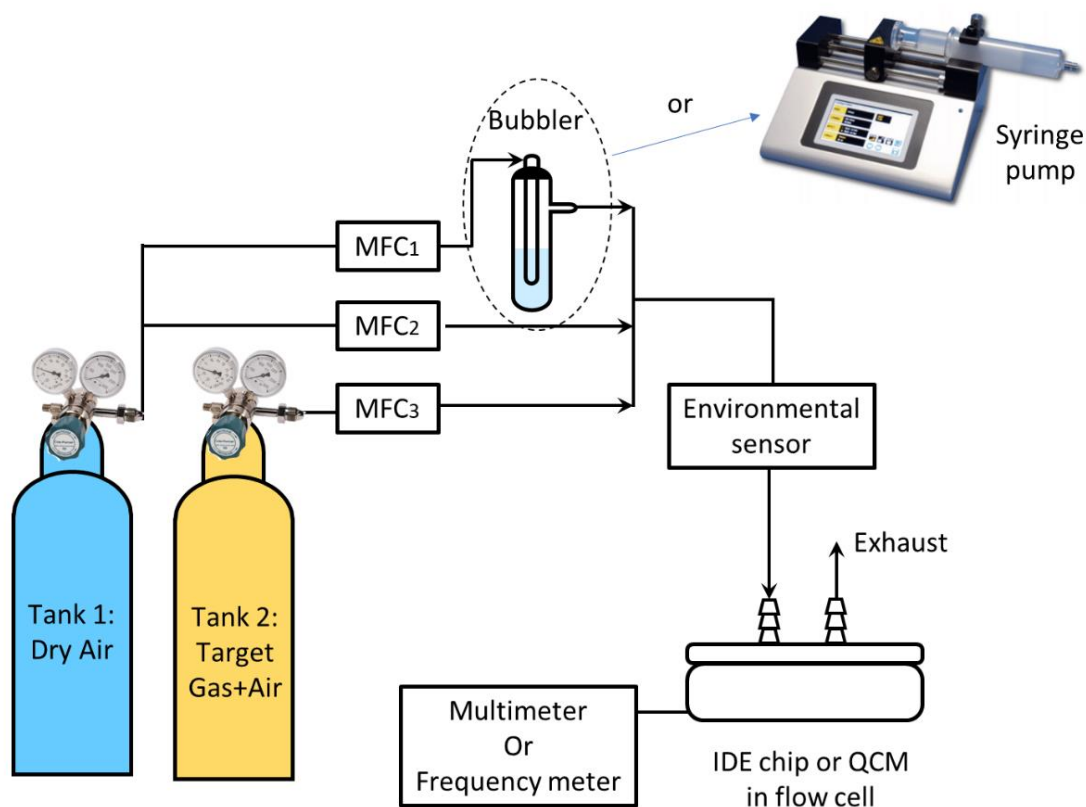


**Figure 3.16** Experimental setup for gas/vapour sensing experiments.

**Gas and humidity concentration calculation:** The  $\text{CH}_4$ ,  $\text{CO}_2$ ,  $\text{CO}$ ,  $\text{NO}_2$ ,  $\text{NH}_3$  concentration ( $C_{\text{ppm}}$ ) was estimated using Eq. (3-1). By controlling the flow rate of gases from tanks 1 and 2, different concentrations of gases were generated. Humidity concentration ( $\text{HC}_{\text{ppm}}$ ) was estimated using Eq. (3-2). The ratio of saturated vapor pressure to input pressure ( $a$ ) was determined by calculating the saturated vapor pressure from Antoine's equation (Eq. (3-3)) at RT and measuring the inlet pressure. Also, the ratio of the saturated vapor pressure to input pressure ( $a$ ) was used to calculate air flow rate including DDW moisture from the bubbler, as shown in Eq. (3-4). Detailed descriptions for the parameters in the equations are presented in **Table 3.2**.

$$C_{\text{ppm}} = \frac{F_t}{F_{a1\_out} + F_{a2} + F_{a3} + F_t} \times 10^6 \quad (3-1)$$

$$HC_{ppm} = \frac{a \times F_{a1\_in}}{F_{a1\_out} + F_{a2} + F_{a3} + F_t} \times 10^6 \quad (3-2)$$

$$a = \frac{\text{Saturated vapour pressure}}{\text{Input pressure}} = \frac{10^{A - \frac{B}{C+T}}}{P_{in}} \quad (3-3)$$

$$F_{a1\_out} = (a + 1)F_{a1\_in} \quad (3-4)$$

**VOCs concentration calculation:** We used a syringe pump to inject volumes of VOCs in liquid phase into the dry air with different rates to create different concentration of VOCs in the sensing chamber. A summary of VOCs' properties can be found in **Table 3.3**. The VOC's concentrations in parts per million (ppm) can be calculated by Eq. (3-5):

$$VOC_{ppm} = \frac{SP \times d \times 24.46}{MW \times F_{a1\_in}} \quad (3-5)$$

**Table 3.2** Descriptions of the parameters in equations (3-1)–(3-4)

Parameters	Description	Unit
$C_{ppm}$	Concentration of target gas	ppm
$HC_{ppm}$	Concentration of water vapour	ppm
$F_{a1\_in}$	Air flow rate from MFC 1 to bubbler	sccm
$F_{a1\_out}$	Air (including DDW moisture) flow rate from bubbler	sccm
$F_{a2}$	Air flow rate from MFC 2	sccm
$F_{a3}$	Air flow rate from MFC 3	sccm
$F_t$	CO <sub>2</sub> flow rate from MFC 3	sccm
$a$	Ratio of saturated vapor pressure to input pressure	-
$P_{in}$	Input pressure at bubbler inlet	psi
A, B, C	Antoine equation constant for DDW (8.07, 1730.63, 233.426)	-
T	Temperature (25 °C)	°C
$VOC_{ppm}$	VOCs vapour concentration at 25 °C and 760 mm Hg	ppm
SP	Syringe pump flow rate	pL/min
d	Density of VOCs at 25 °C and 760 mm Hg	g/ml
24.46	Volume (L) of 1 mole of gas at 25 °C and 760 mm Hg	L/mol
MW	Molar mass	g/mol

**Table 3.3** Summary of VOCs properties.

VOC	Density (g/ml)	Molar mass (g/mol)
Methanol	0.792	32.04
Ethanol	0.789	46.07
Isopropanol	0.786	60.10
Acetone	0.784	58.08

### **3.4.2 Photodetector Test Setup and Sensing Experiment:**

The optoelectronic characteristics of the photodetector based on the ZIF-8/CNFs nanocomposite were systematically investigated using a Keithley source measurement unit (SMU Model 2450). These investigations were conducted under RT and ambient conditions within a dark box to prevent the influence of ambient light. Laser light sources emitting at wavelengths of 635 nm (Thorlabs, LDM635), 532 nm (Thorlabs, CPS532), and 404 nm (Thorlabs, CPS405) were employed with nominal output powers of 3.0 , 4.7, and 4.9 mW, respectively. Neutral density (ND) filters (Thorlabs, FW1AND) with the optical density of 0.5, 1, 2, 3 were employed to adjust light power levels.

In this chapter, we have outlined the experimental methods encompassing materials synthesis, characterization, thin film, and sensors fabrication, as well as the experimental test setup. These methods lay the foundation for the subsequent three chapters, which delve into the practical applications of the synthesized nanocomposite in gas sensing and photodetector applications.

## **Chapter 4 : Application of ZIF-8/MWCNTs as a Resistive Based Sensor for CH<sub>4</sub> Detection**

The contents of this chapter have been published in a paper entitled “MOF/MWCNT–Nanocomposite Manipulates High Selectivity to Gas via Different Adsorption Sites with Varying Electron Affinity: A Study in Methane Detection in Parts-per-Billion”, ACS sensors, 2022, 7, 3846-3856, <https://doi.org/10.1021/acssensors.2c01796>.

### **4.1 Introduction**

Detecting methane at leak relevant levels at normal atmospheric conditions is crucial to industrial safety and environmental protection. Firstly, CH<sub>4</sub> is highly flammable exhibiting a deflagration to detonation transition in the range of 5-15% by volume (i.e., ~50,000-150,000 parts-per-million (ppm)). Undesired release of CH<sub>4</sub> during coal extractions, leaks from natural gas pipelines or outbursts can contribute to catastrophic disasters if not identified and mitigated quickly [1]. Furthermore, CH<sub>4</sub> is known to be 21 times more potent as a greenhouse gas over carbon dioxide (CO<sub>2</sub>) with an atmospheric lifetime of roughly a decade due to its very low reactivity to lose or gain an electron in atmospheric conditions [231]. Based on Intergovernmental Panel on Climate Change’s research, at least a quarter of today’s global warming is driven by CH<sub>4</sub> from anthropogenic sources, and it is a key precursor to tropospheric ozone generation that is harmful for our ecosystem as an air-pollutant. Thus, there is an urgent need to detect fugitive CH<sub>4</sub> at lower than the global ambient concentration level of  $1.8 \pm 0.2$  ppm [231], [232]. However, even with the current state-of-the-art detection techniques that include infrared spectroscopy [5], modulation spectroscopy [233], Raman spectroscopy [6], gas chromatography [234], photothermal spectroscopy [9], and pyroelectric sensors [235], low-cost and high-performance detection of CH<sub>4</sub>

at very low concentration with a miniaturized integrated gas sensor is still a formidable challenge. Therefore, an unmet need still exists for developing novel, cost-effective, and reliable miniaturized sensors with high sensitivity and selectivity for ppb concentration levels of CH<sub>4</sub>.

In recent years, the advances in micro/nano-fabrication technology and the use of newly designed nanomaterials facilitate the development of cost-effective miniaturized integrated gas sensors that have enhanced sensitivity and selectivity towards various target gases [7]. Among newly designed materials, metal oxides, graphene-based composites, CNTs, and polymers have been rigorously investigated as gas sensing materials [1]. However, the generally weak interaction of CH<sub>4</sub> with these materials led to very short residual time in the order of 10<sup>-10</sup> seconds making detection at very low concentrations a considerable challenge [1], [3], [9]. To enhance sorption and residual time, nanoporous materials like metal-organic-frameworks (MOFs) have been proposed. MOFs self-assemble via coordination bonds of metal nodes with organic ligands presenting a novel class of thermally stable and chemically inert crystalline hybrid nanoporous material with active sites of varying electron affinity. Their permanent porosity, tunable pore size and functionalizable internal pore-surfaces are conducive to rendering enhanced chemical sensitivity and selectivity that has been explored at length [10], [28], [29]. As such, MOFs are being routinely investigated for detection of polar molecules, organic molecules, and ions [68], [69], [92], [96]. However, only a few MOFs-based CH<sub>4</sub> sensors have been reported so far and the improvement of selectivity and sensitivity is still required before MOFs could be widely used as CH<sub>4</sub> sensors [98], [143]–[145], [236].

MOFs in general are excellent for high-pressure (~35 bar) gas storage applications owing to their high surface area and free volume allowing high gas uptake. However, at atmospheric pressures these factors do not correlate and their adsorption capacity is low [237]. This severely

limits real-time gas sensing applications with MOFs and results in low sensitivity, especially for low reactive gas like CH<sub>4</sub> which generally has weak interaction [1]. Moreover, the presence of ambient moisture in the order of a few parts per thousand at normal atmospheric conditions often leads to false positives, making selective detection a formidable challenge in most of sensing material, specifically in MOFs [238], [239]. Another key limitation of most MOFs as sensing materials is their intrinsic low electrical conductivity (lower than 10<sup>-10</sup> Scm<sup>-1</sup>) [50]. Based on experimental and theoretical studies, the basic reasons for this poor conductivity are the lack of charge carrier mobility and limited energy transport pathways because electron transfer proceeds weakly between non-redox-active metal centers and organic linkers [46], [47]. This severely hinders their applicability in making electrical sensors. Most reports in this area therefore focuses on optical sensors [36], [40], [41], or more complicated gravimetric sensors such as MOF-coated microcantilevers [42], and quartz crystal microbalances [43]–[45]. However, if MOFs can be tailored to improve electrical transport properties, adsorption/desorption kinetics can be monitored electrically by exploiting the property of varying electron affinity at their different adsorption sites. Thus, overcoming this electrical conductivity issue has been attempted by various routes such as compositing them with conducting/semiconducting nanomaterials (e.g., QDs, NPs, 2D-graphene, and CNTs), by post-synthetic modification, or via incorporation of guest molecules [46], [48]–[51]. In this work, we use bare MWCNTs to make a composite sensing material.

In the last two decades, CNTs-based sensors have demonstrated huge potential and found applications in gas sensing because of their unique morphology and electrical properties. However, pristine (bare) CNTs are chemically inert - exhibiting strong sp<sup>2</sup> bonds and weak sp<sup>3</sup> bonds at the tube ends, making it impossible to be utilized for gas sensing (especially for non-polar gases with low reactivity such as CH<sub>4</sub> to accept or donate electrons) [123], [240], [241]. Thus, CNTs have

been typically modified with functional groups, dopants, metallic NPs, metal-oxide NPs, and conductive polymers to overcome this limitation [1], [126], [133]. We take an alternative route following recent reports on composite modification of MWCNTs with MOFs [52], [53]. Incorporating MWCNTs in MOF architecture as a composite not only can combine the properties of both MWCNTs and MOFs for obtaining superior sensing performance, but also could address the limitation of both MOFs and MWCNTs for detection of low reactive and non-polar gases like CH<sub>4</sub>. Although there are a few reports on using of MOFs/MWCNTs composite for detection of VOCs [52], [53], to our knowledge, there is no study on using of this composite for detection of CH<sub>4</sub>. In most of the literatures, functionalized-MWCNTs were used to make MOF/MWCNTs composite [194], [195]. However, as a result of functionalization, MWCNTs could undergo important changes and lose their original properties, such as losing their hydrophobicity, which is desirable for gas sensing applications. Therefore, using bare MWCNTs, which are super-hydrophobic, could be a promising way to improve the overall hydrophobicity of their composite with MOFs.

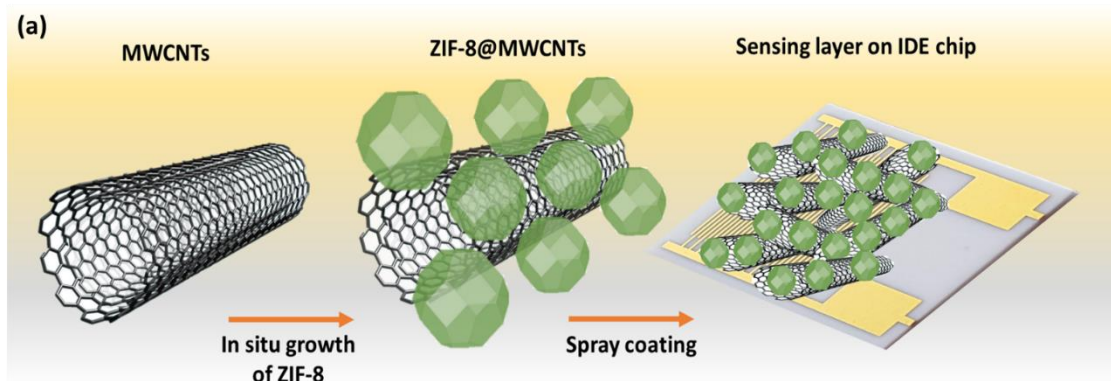
In this work, we introduce a nanocomposite of MOF with bare MWCNTs, which has a unique electrical property for selective detection of CH<sub>4</sub> at RT. Within the class of MOFs, we chose our sensing layer on ZIF-8 for its low water affinity and good stability in ambient conditions. This is the first ever usage of ZIF-8/MWCNTs nanocomposite as sensing layer of a chemiresistive sensor for selective detection of CH<sub>4</sub>. By making this nanocomposite, we demonstrate enhancement of electrical conductivity and hydrophobicity. Furthermore, we exploit its unique electrical transport enhancement for detecting CH<sub>4</sub> at very low concentration of 10 ppb in normal atmospheric conditions with a determined LOD ~0.22 ppb, hitherto unprecedented. Our composite approach is guided by the possibility of decreasing the electronic bandgap and activation energy of ZIF-8 by a

random incorporation of MWCNTs. For further evaluations of our sensor performance, responsivity, reversibility, selectivity, response and recovery time, sensitivity, repeatability, and linearity are systematically investigated.

## 4.2 Results and Discussion

### 4.2.1 Structural and Morphological Characterization of ZIF-8, MWCNTs and ZIF-8/MWCNTs Nanocomposite

In this work, in-situ growth of ZIF-8 in the presence of bare MWCNTs is achieved through an in-situ sonochemical synthesis method to make ZIF-8/MWCNTs nanocomposite. **Figure 4.1a** illustrates a schematic drawing of the preparation process of the ZIF-8/MWCNTs nanocomposite and its spray-coated thin film on the surface of an IDE chip. Zeta optical profilometer was used for the ZIF-8/MWCNTs' film thickness measurements, and defect inspection (**Figure 4.1b**). The obtained nanocomposite film has great uniformity with the thickness of  $\sim 8 \mu\text{m}$  without any defect. For further characterization, FT-IR spectroscopy (**Figure 3.1**), Raman spectroscopy (**Figure 3.2**), XRD analysis (**Figure 3.3**), and UV-vis spectroscopy (**Figure 3.4**) for bare MWCNTs, ZIF-8 and ZIF-8/MWCNTs nanocomposite, and FE-SEM/EDX analysis (**Figure 3.6** and **3.7**) for ZIF-8 and ZIF-8/MWCNTs nanocomposite, and TEM image (**Figure 3.8**) for bare MWCNTs have been performed.



(b)

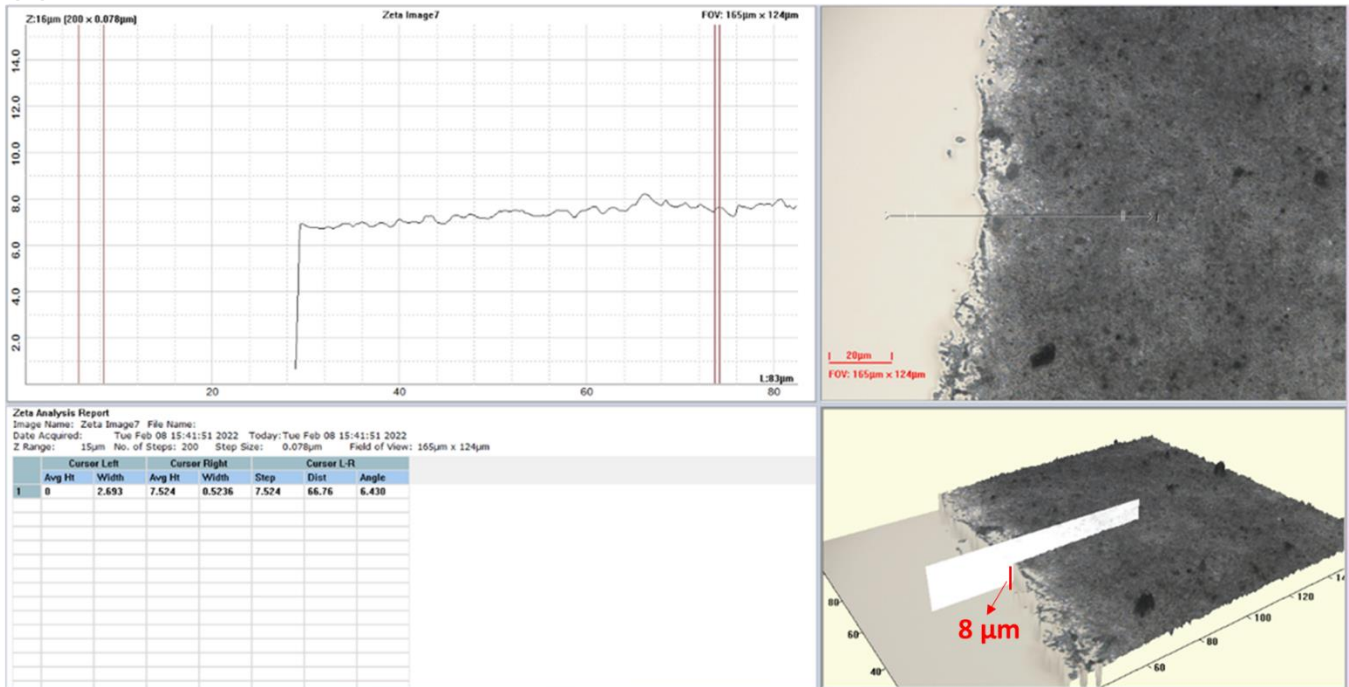


**Figure 4.1 a)** Schematic illustration of the material preparation process of the ZIF-8/MWCNTs nanocomposite and its spray-coated thin film on the surface of an IDE chip. **b)** Zeta Optical profilometer is used to measure thickness of the ZIF-8/MWCNTs film (~8 μm thick) and to inspect the uniformity of the spray-coated film.

The band gaps ( $E_g$ ) of the materials (**Figure 4.2a**) are determined by the UV-Vis absorption spectra - using the formula proposed by Tauc/Davis and Mott et al. [242]:

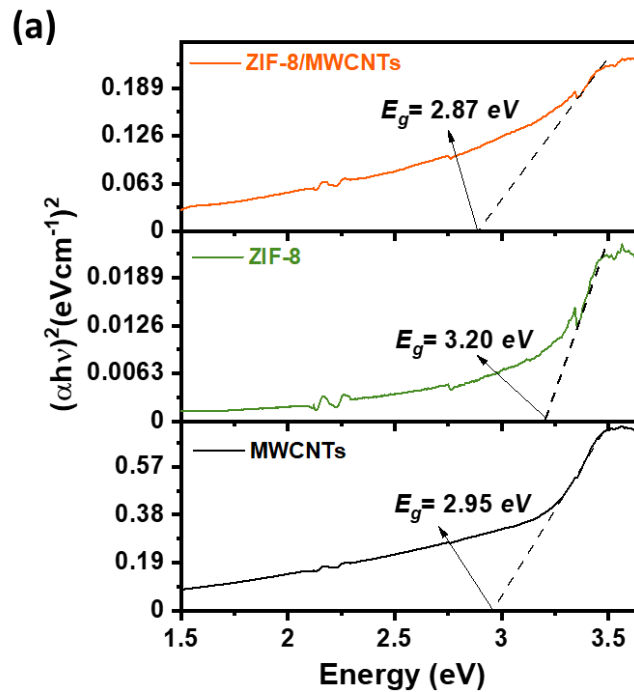
$$(\alpha hv)^2 = A(hv - E_g) \quad (4-1)$$

where  $\alpha$  is the absorption coefficient,  $hv$  denotes the photon energy corresponding to frequency  $\nu$ ,  $A$  is constant, and  $E_g$  is bandgap. The band gap values are obtained by an extrapolation of the linear part of the  $(\alpha hv)^2$  versus  $hv$ .

As reported so far, ZIF-8 is considered as an insulator with a wide band gap of around 5.5 eV [50][243]. However, the ZIF-8 nanoparticles (~50 nm) synthesized in this work, with a reduced band gap of 3.2 eV (**Figure 4.2a**), fall into the category of wide-bandgap semiconductors. This reduction in the band gap could be attributed to exceptional electrical properties of nanoparticles under size reduction [244][245]. In intrinsic semiconductors, no free charge carriers are available for conduction (the number of electrons and holes are equal) at RT, resulting in large activation or operation energy ( $\Delta E$ ) and no conduction [211]. Consequently, the synthesized ZIF-8 does not exhibit electrical conduction at RT, indicating its intrinsic semiconducting behavior. The typical band diagram of the p-type semiconductors for a visual representation of band gaps ( $E_g$ ), Fermi level ( $E_F$ ), activation energy ( $\Delta E$ ) and acceptor level ( $E_a$ ) has been illustrated in **Figure 4.2b** for ZIF-8, which has intrinsic semiconductive behavior.

Creating a composite of ZIF-8 with bare MWCNTs reduced the band gap to 2.87 eV (**Figure 4.2a**), indicating a semiconductor nature. On the other hand, our resistive sensor based on this composite shows a rise in resistance upon exposure to humidity, known for its electron-donating characteristics (**Figure 4.7a**). This behavior suggests that the ZIF-8/MWCNTs nanocomposite behaves as a p-type semiconductor. In p-type semiconductors, charge carriers are holes, and the adsorbed water molecules neutralize these holes by donating electrons, resulting in increased resistance. In P-type semiconductors, there are energy levels within the band gap very close to the valence band, which are called acceptor level ( $E_a$ ). This shifts the effective Fermi level to a point about halfway between the acceptor levels and the valence band to show a p-type semiconductor behavior [211]. The typical band diagram of the p-type semiconductors for a visual representation of band gaps ( $E_g$ ), Fermi level ( $E_F$ ), activation energy ( $\Delta E$ ) and acceptor level ( $E_a$ ) has been illustrated in **Figure 4.2b** for ZIF-8/MWCNTs nanocomposite, which shows p-type

semiconductive behavior. In p-type semiconductors, electrons can be easily excited from the valence band into acceptor levels, leaving mobile holes in the valence band that can contribute to good electrical conduction at RT, and small activation energy could significantly enhance gas-sensing performance due to the easier sharing of electrons to make more van der Waals interaction with target gas causing higher gas uptake. Hence, the incorporation of bare MWCNTs with ZIF-8 results in a nanocomposite exhibiting p-type semiconducting behavior. This overcomes the previous challenge of weak interaction between recent reported nanomaterials and methane [1], [3], [9], owing to its low activation energy and large surface area. The enhanced interaction enables the detection of methane at exceptionally low concentrations for the first time, as demonstrated in our subsequent experiments.



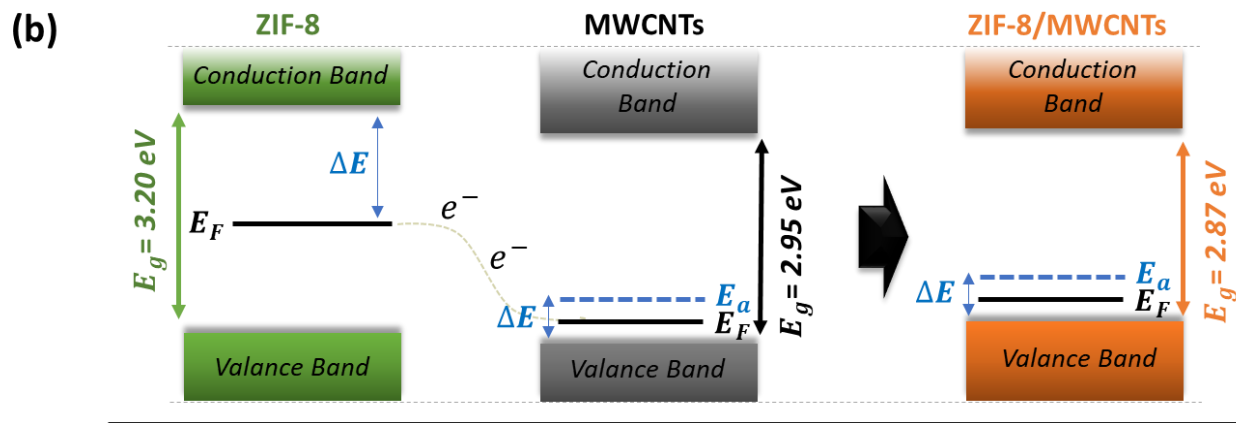


**Figure 4.2 a)** Tauc's plots for the band gap energy determination of MWCNTs (black), ZIF-8 (green) and ZIF-8/MWCNTs nanocomposite (orange), respectively. **b)** Schematic illustration of the band diagram for a visual representation of band gaps ( $E_g$ ), Fermi level ( $E_F$ ), activation energy ( $\Delta E$ ) and acceptor level ( $E_a$ ) in intrinsic (ZIF-8) and p-type semiconductive bare MWCNTs and ZIF-8/MWCNTs nanocomposite. The synergistic effect of compositing MWCNTs with ZIF-8 is evident in the lowering of the band gap and activation energy in the nanocomposite.

#### 4.2.2 Sensor Performance Evaluation:

To evaluate gas-sensing performance, the spray-coated IDE chips with ZIF-8/MWCNTs nanocomposite (5wt% of MWCNTs) are exposed to predetermined concentrations of CH<sub>4</sub>, CO, CO<sub>2</sub>, NO<sub>2</sub>, NH<sub>3</sub>, toluene, benzene, methanol, ethanol, isopropanol, and water vapour. Physically, upon exposure to different gas/vapour analytes, molecules are physisorbed into the pores and surfaces of ZIF-8 via electron accepting from or donating to ZIF-8/MWCNTs layer (**Figure 4.3**). The net exchanged electrons from the sensing layer to gas/vapour analytes can be negative ( $-\Delta e^-$ ), positive ( $+\Delta e^-$ ), or zero ( $\Delta e^- = 0$ ) resulting in decrease, increase, or no changes in normalized resistance change ( $\Delta R/R_0$ ), respectively.

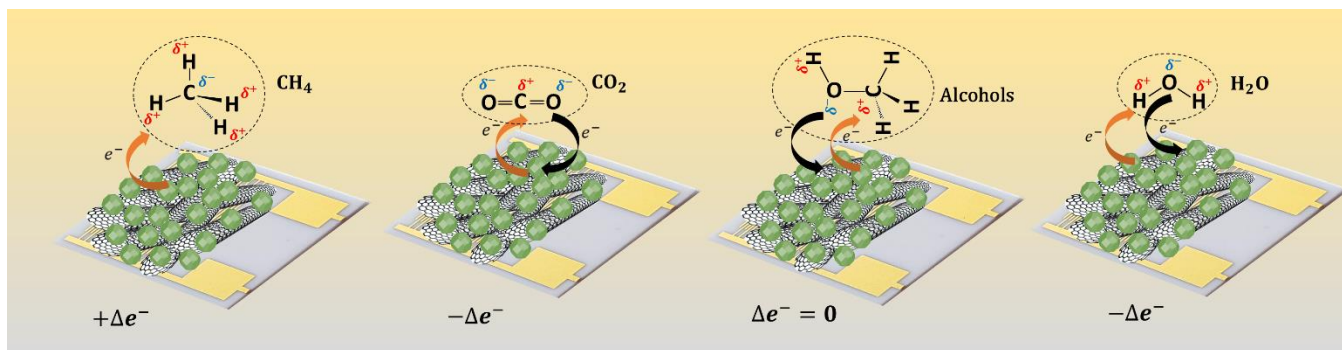


**Figure 4.3** Schematic illustration of CH<sub>4</sub>, CO<sub>2</sub>, alcohols vapours and H<sub>2</sub>O molecules physisorption into the pores and surfaces of ZIF-8 via electron accepting from or donating to ZIF-8/MWCNTs layer and the net exchanged electrons ( $\Delta e^-$ ) from the sensing layer to them, respectively.

For investigating our sensor's CH<sub>4</sub> responsivity, the coated IDE chips with ZIF-8/5wt% MWCNTs was initially exposed to 200 standard cubic centimeter per minute (sccm) dry air to record the baseline resistance ( $R_0$ ), followed by exposing to desired CH<sub>4</sub> concentrations (1.5 - 100 ppm) at the total flow rate of 200 sccm until sensor response reached steady state (**Figure 4.4**). Subsequently, dry-air flow cycle was run to recover back the baseline confirming reversibility (**Figure 4.5**) which can be attributed to physisorption without chemical bonding. The considerable responsivity to CH<sub>4</sub> down to 1.5 ppm has roots in the significantly smaller band gap of our composite and smaller activation energy ( $\Delta E$ ) (**Figure 4.2b**), allowing easier share of electrons between the composite and the gas/vapour molecules to make a van der Waals interaction causing higher gas uptake in our system. In contrary to CH<sub>4</sub>, 100 ppm of pure CO<sub>2</sub> results in a slight increase in normalized resistance change ( $+\Delta e^-$ ) (**Figure 4.6a**). However, in the case of ethanol, methanol, and isopropanol vapors, the sensor response is negligible ( $\Delta e^- = 0$ ) (**Figure 4.6a**).

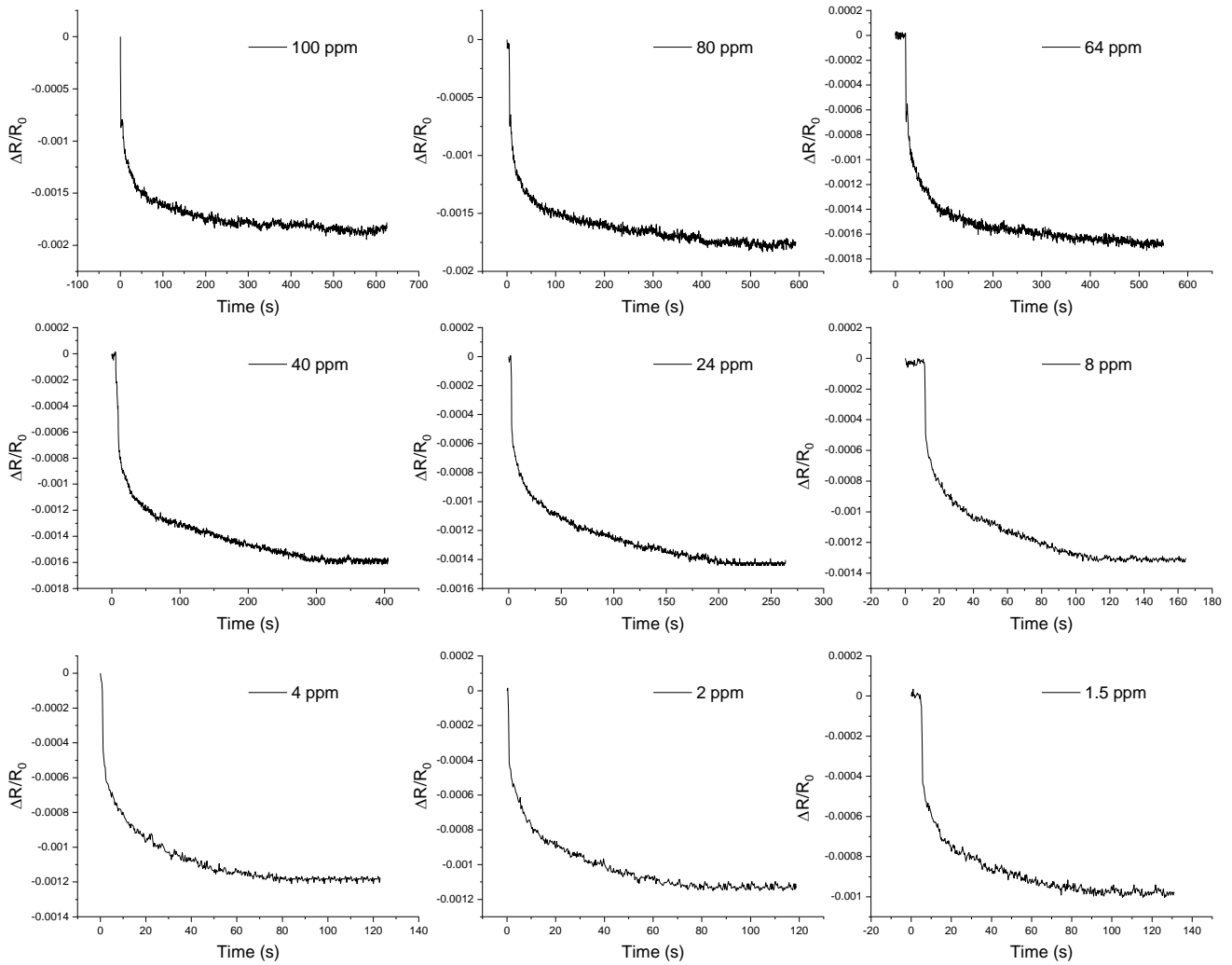


**Figure 4.4** The sensor responses by exposing to desired  $\text{CH}_4$  concentrations (1.5 - 100 ppm) at the total flow rate of 200 sccm until sensor response reached steady state.

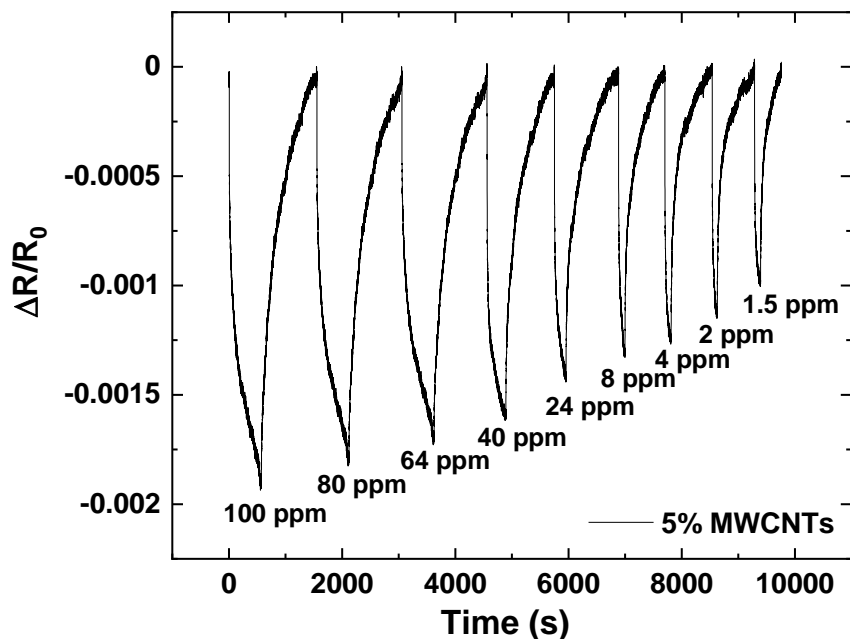


**Figure 4.5** The dynamic response/recovery signals of the sensor with 5wt% MWCNTs for CH<sub>4</sub> at total flow rate of 200 sccm: As it is evident our sensor shows good response in this range of concentrations, even as low concentration of 1.5 ppm.

Moreover, to evaluate our sensor's selectivity toward CH<sub>4</sub> in the presences of these vapours, our sensor was exposed to binary mixtures of 100 ppm of CH<sub>4</sub> with each of these vapours respectively resulting in nearly identical response compared to 100 ppm of CH<sub>4</sub> alone (**Figure 4.6b**) with appreciable reversibility, attesting to selective sensing performance in mixtures. This selectivity can be attributed to ZIF-8's different adsorption sites with varying electron affinity which is explained in detail in section 2.3. The sensor responses to CO, NO<sub>2</sub>, NH<sub>3</sub>, toluene, and benzene (10 ppm) were also investigated for additional evaluation of our sensor selectivity (**Figure 4.6c and d**). In contrary to CH<sub>4</sub>, the sensor response to 10 ppm of CO, NO<sub>2</sub>, NH<sub>3</sub>, toluene and benzene gases/vapors are negligible ( $\Delta e^- = 0$ ) (**Figure 4.6c**). To evaluate our sensor's selectivity toward CH<sub>4</sub> in the presences of these analytes, our sensor was exposed to binary mixtures of 10 ppm of

CH<sub>4</sub> with each of these gases/vapours, respectively, resulting in nearly identical response compared to 10 ppm of CH<sub>4</sub> alone (**Figure 4.6d**) with appreciable reversibility, attesting to selective sensing performance in mixtures. As the outdoor background concentrations of CO, NO<sub>2</sub>, NH<sub>3</sub>, benzene, and toluene are around 0.12 ppm [246], 0.09 ppm [247], [248], 0.005 ppm [249], 0.02 ppm [250], [251], and 0.005 ppm [252], respectively, the CH<sub>4</sub> selective responses of our sensor in presence of these analytes were done in 10 ppm of each of them, orders of magnitude higher concentration than the outdoor concentration of these analytes.

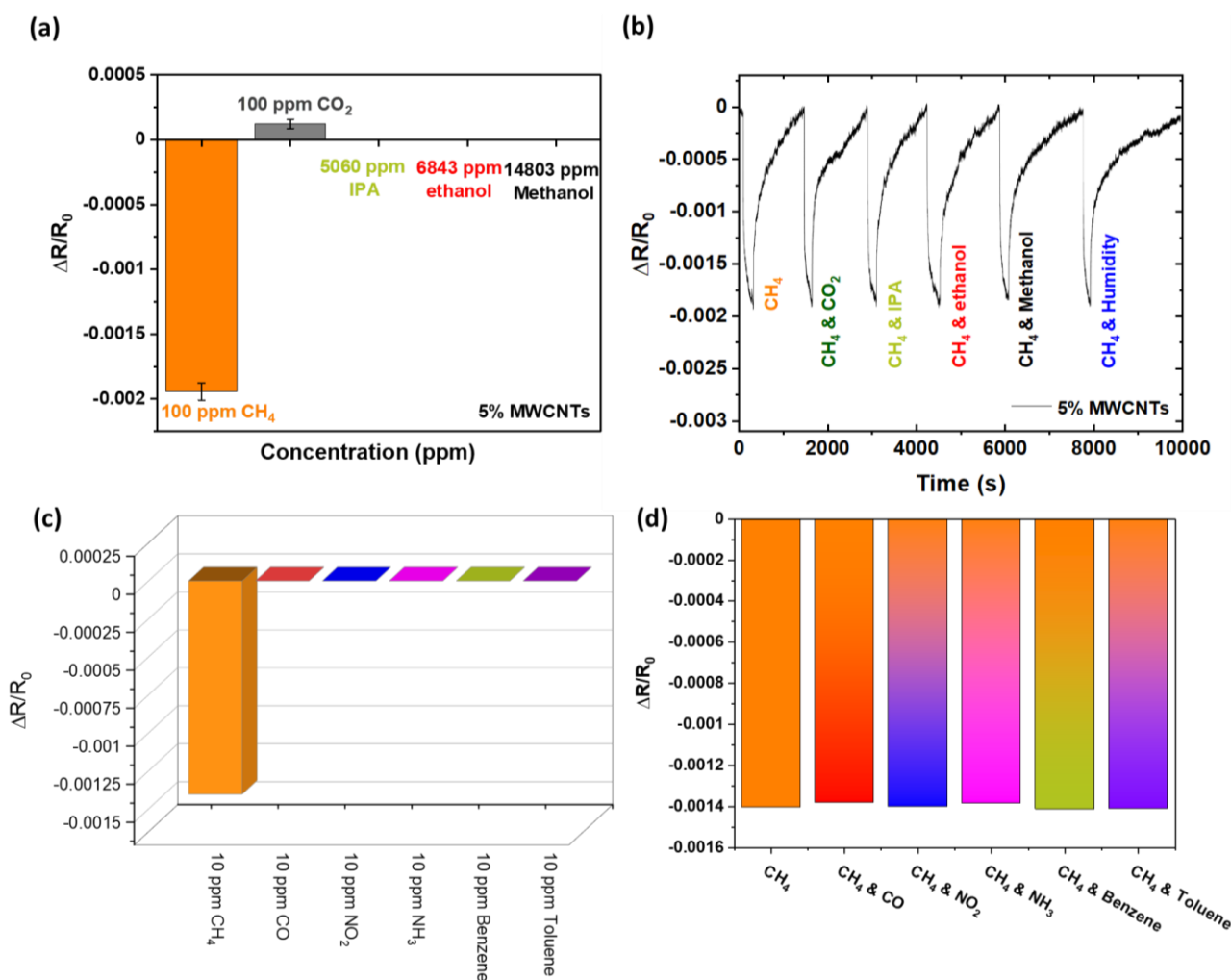


**Figure 4.6** a) The sensor's comparative responses to 100 ppm of CH<sub>4</sub>, 100 ppm of CO<sub>2</sub>, 5060 ppm of IPA, 6843 ppm of ethanol, and 14803 ppm of methanol at a total flow rate of 200 sccm.

**b)** Selectivity tests of the sensor toward 100 ppm CH<sub>4</sub> in a mixture in presence of 100 ppm of CO<sub>2</sub>, 5060 ppm of IPA, 6843 ppm of ethanol, 14803 ppm of methanol and 24327 ppm of water vapour at a total flow rate of 200 sccm, respectively. **c)** The sensor's comparative responses to 10 ppm of CH<sub>4</sub>, CO, NO<sub>2</sub>, NH<sub>3</sub>, benzene, toluene at a total flow rate of 200 sccm. **d)** Selectivity tests of the sensor toward 10 ppm of CH<sub>4</sub> in a mixture in presence of 10 ppm of CO, NO<sub>2</sub>, NH<sub>3</sub>, benzene and toluene vapour at a total flow rate of 200 sccm, respectively.

One key challenge of various sensing layers explored in the literature to date for CH<sub>4</sub> is the potential false positives with ambient moisture [1]. Thus, from the perspective of maintaining reliability, it is very important to eliminate or mitigate the dependence of sensor response to humidity. Generally, the concentration of moisture in the atmosphere ranges from 6,000 to 12,000 ppm (30-80% RH) [253]. To investigate the response of our sensor to ambient moisture, it was exposed to different humidity levels. Contrary to CH<sub>4</sub>, water vapour results in a slight increase in normalized resistance change ( $+\Delta e^-$ ) (**Figure 4.7a**). Nevertheless, the positive change in resistance to 13,662 ppm of water vapour, which is more than 80% RH, remains significantly less than the response to 1.5 ppm of CH<sub>4</sub>. This can be attributed to the inherent hydrophobicity of the ZIF-8 at the inner-network of their pores with the limited adsorption site on its outer surface which we will discuss further in section 2.3 [254]. To investigate the performance of our sensor for CH<sub>4</sub> detection in humid environment, it was exposed to mixtures of 100 ppm of CH<sub>4</sub> with 24,327 ppm of humidity (more than 90% RH). The results show that the sensitivity of our sensor to CH<sub>4</sub> is not affected by the presence of humidity even at RH > 90% (**Figure 4.6b**), confirming that CH<sub>4</sub> and H<sub>2</sub>O molecules do not compete for the same adsorption sites in the ZIF-8 pores which will be discussed in detail in response mechanism section. In addition, the stability of our sensor over a period of 8 months has been tested and demonstrated in **Figure 4.7b**.

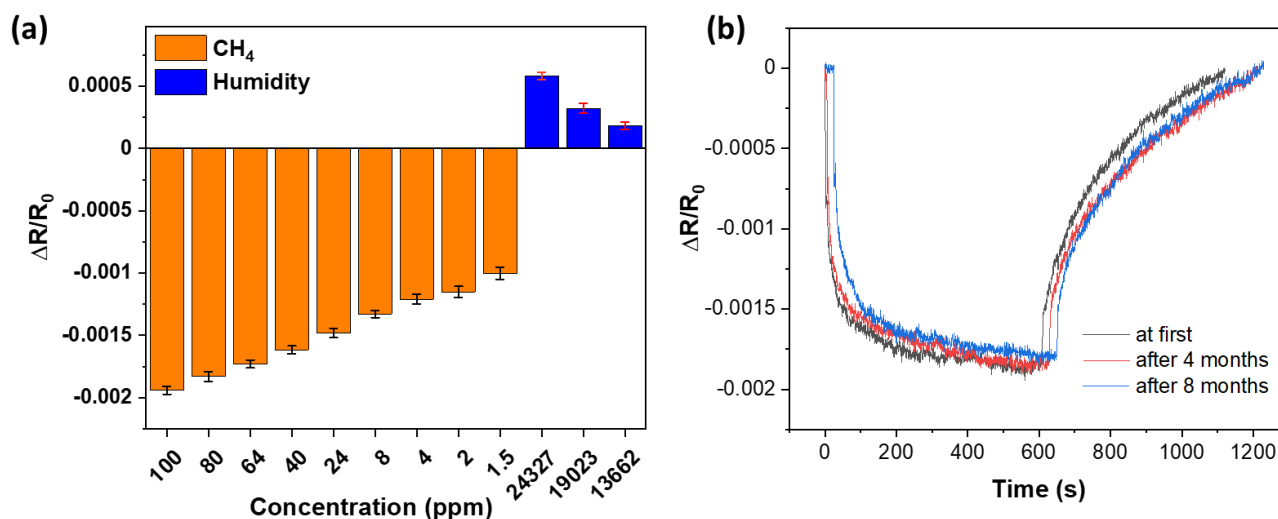


**Figure 4.7 a)** Humidity response of our sensor in compared to  $\text{CH}_4$  response at a total flow rate of 200 sccm. **b)** The sensor responses to 100 ppm of  $\text{CH}_4$  at the total flow rate of 200 sccm over a period of 8 months. Overlapping of these data sets reflects high sensor stability.

**Repeatability and linearity:** For different total flow rates in the range of 12.5 – 200 sccm, when the device is repeatedly exposed to  $\text{CH}_4$  and dry air alternatively, no significant change in the response sensitivity is observed for different concentrations, indicating that the fabricated sensor has good repeatability and stability (**Figure 4.8**). The alternative exposure to gas and dry air was repeated seven times to ascertain the repeatability. Error bars represent standard deviations for measurements taken from the seven independent experiments. As can be seen for higher flow rates in **Figure 4.8**, the dynamic range of the sensor is larger and typically shows an exponential change in response that can further be explained in detail with the variations in partition function at higher concentrations. However, the linearity of the sensor response is maintained in the concentration ranges of 8-100 ppm, for all the total flow rates. This allows us to construct calibration curves for the individual flow rates (**Figure 4.9**).

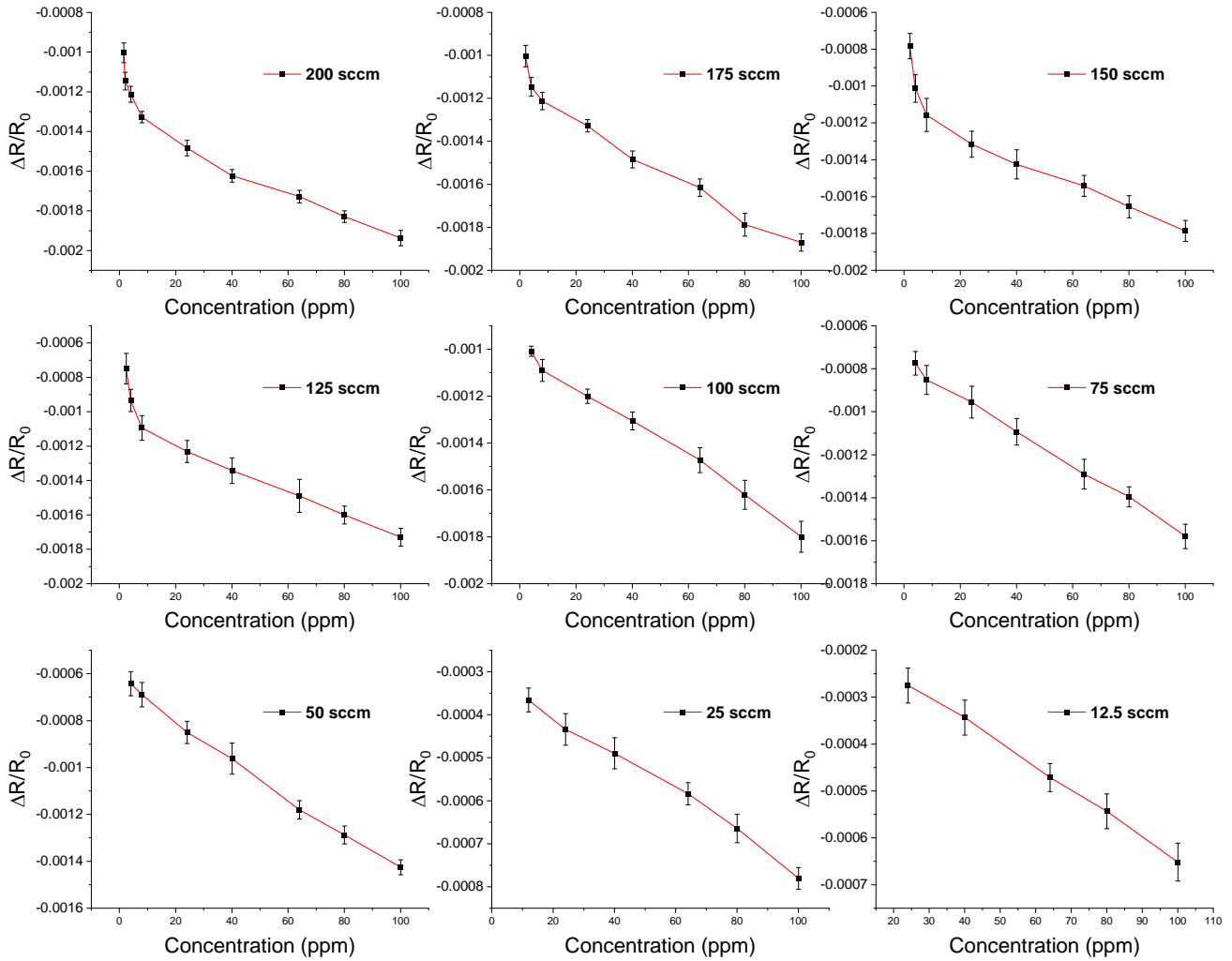


**Figure 4.8** The sensor responses to  $\text{CH}_4$ ' random shuffling concentration range of 1.5-100 ppm with different total flow rate range of 12.5-200 sccm. Error bars represent standard deviations of 7 measurements. Error bars for each data point are in the order of 1-10%. Red lines are a guide to the eyes.

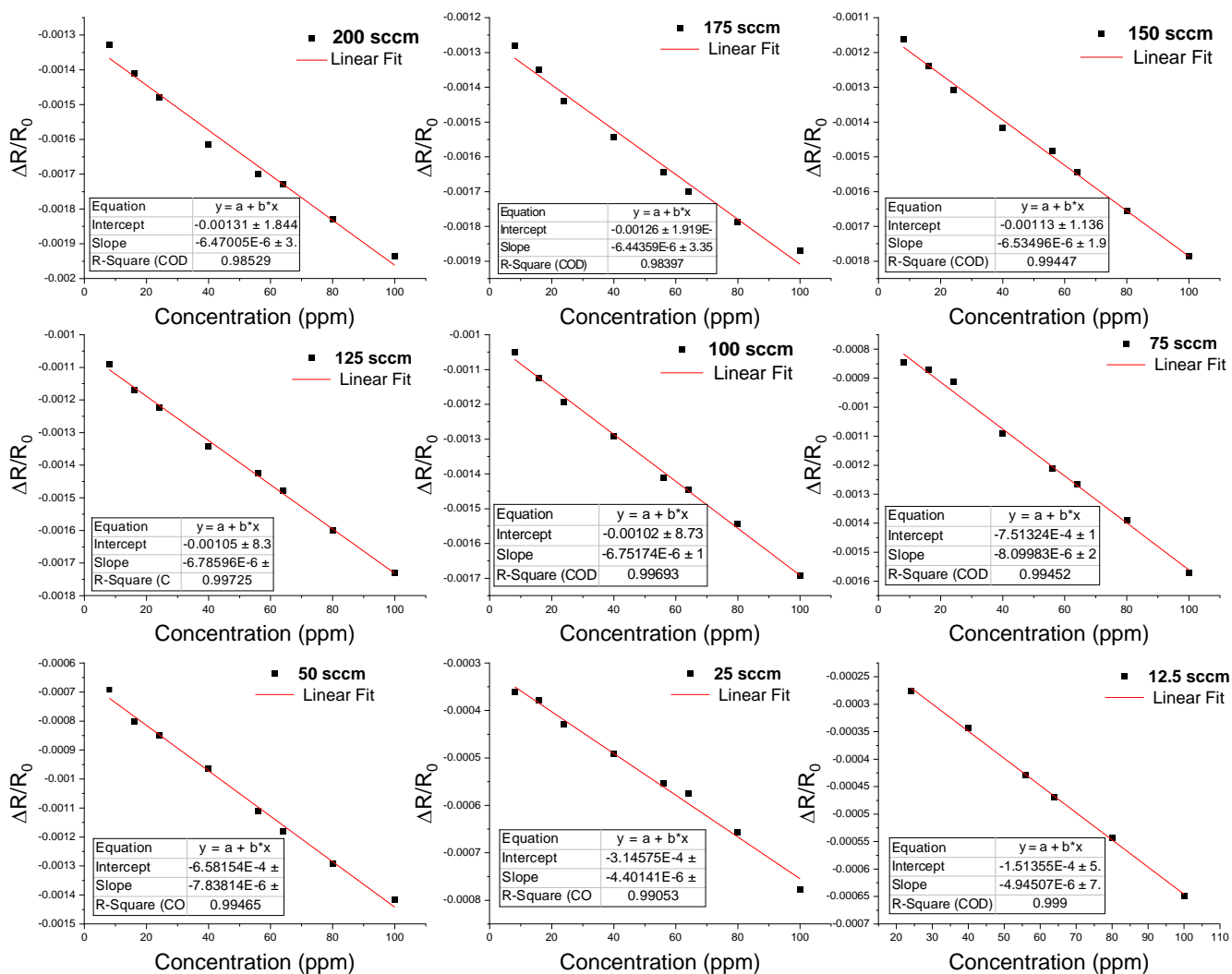


**Figure 4.9** Calibration curves showing linearity of the sensor responses to CH<sub>4</sub>' random shuffling concentration range of 8-100 ppm at different total flow rate of 12.5-200 sccm. Red lines are linear fitting of data.

**The effect of total flow rate changes on sensitivity & normalized resistance change ( $\Delta R/R_0$ ):** Definition of sensitivity, based on International Union of Pure and Applied Chemistry (IUPAC) standards, is the slope of the calibration curve [255], [256]. Based on the calibration curve for each flow rate in **Figure 4.9**, for CH<sub>4</sub> concentration ranges of 8-100 ppm, sensitivity of the fabricated

sensor is presented in **Figure 4.10a**. As can be seen in **Figure 4.10b**, by increasing the total flow rate, the slope of  $\Delta R/R_0$  also increases and reaches a maximum at 75 sccm. This is probably due to the decrease in boundary layer thicknesses with increasing flow rate, increasing adsorption. The decreases in the slope at higher flow rates may be due to the limiting adsorption time of the gas molecules on the sensor surface.

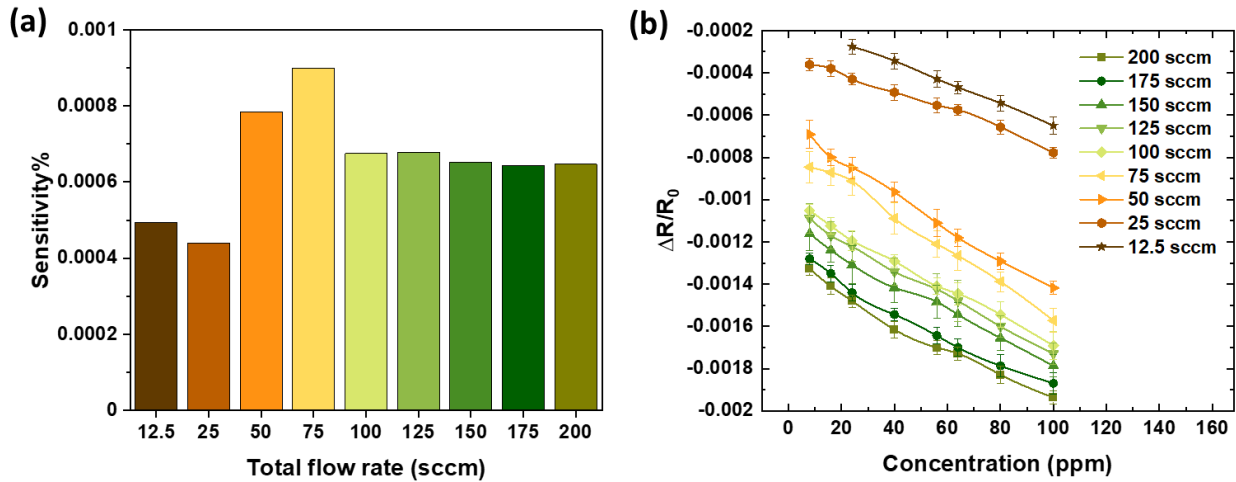


**Figure 4.10 a)** Sensor sensitivity for 8-100 ppm of CH<sub>4</sub> at different total flow rates of 12.5-200 sccm. **b)** The effect of variation of total flow rate on our sensor's normalized resistance change.

**The effect of variation of thickness on the sensor response:** To evaluate the effect of variation of thickness of the sensing layer on the device characteristics and detection process, sensor responses with 4 and 8 μm thick films were investigated, respectively, at total flow rates of 12.5 and 200 sccm (**Figure 4.11**). As can be seen in **Figure 4.11**, the sensitivity increased (higher slope) with a thicker layer which can be attributed to the increased number of pores for the adsorption of larger amount of gas molecules [144], [257].

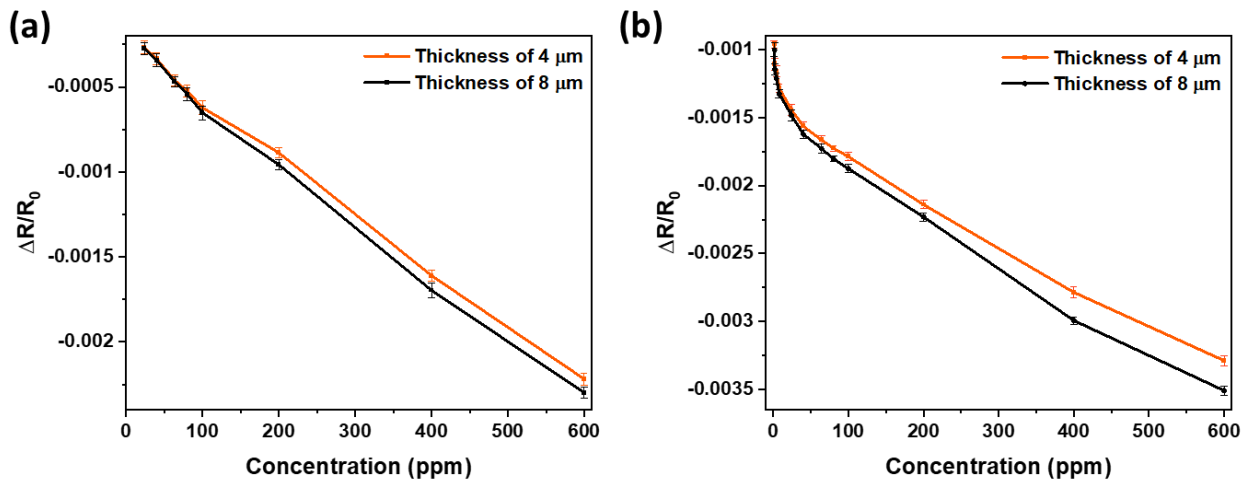


**Figure 4.11** The effect of variation of thickness on the response of the fabricated sensor to  $\text{CH}_4$  in concentration range of 1.5-600 ppm for total flow rates of **a)** 12.5 sccm, and **b)** 200 sccm. Red and black lines are a guide to the eyes.

Furthermore, to investigate the variation of MWCNTs concentration in the composite's effect on our sensor performance, a newly coated IDE chips with ZIF-8/10wt% MWCNTs was exposed to repeating cycles of  $\text{CH}_4$  (10 ppb to 100 ppm) and dry-air flow as before (**Figure 4.12a**). The relative resistance change as a function of  $\text{CH}_4$  concentration is normalized and fitted as a power-law dependence, shown in **Figure 4.12b**, with the x-intercept representing the LOD  $\sim 0.22$  ppb. The normalized minimum measurable limit was determined to be in the order of 0.17 corresponding to the 3x noise floor at 200 sccm flow of dry air. Generally, gas adsorption in porous materials occurs by three steps of adsorption, diffusion, and desorption process [258]. This non-linear response of our system to  $\text{CH}_4$  could be attributed to the dominance of surface adsorption effect at lower concentrations and bulk diffusion effect at higher concentration. Compared to the ZIF-8/5wt%MWCNTs based sensor for detection of  $\text{CH}_4$ , the ZIF-8/10wt%MWCNTs based sensor shows a slight increase in normalized resistance change which can be attributed to its higher

uptake of CH<sub>4</sub> in atmospheric pressure due to increase in electron transport and the easier sharing of electrons to make van der Waals interaction with CH<sub>4</sub> (**Figure 4.12c**). Interestingly, the response and recovery times are significantly reduced with the increase in MWCNTs concentration because more MWCNTs facilitate faster rate of charge transfer on adsorption (**Figure 4.12d**).

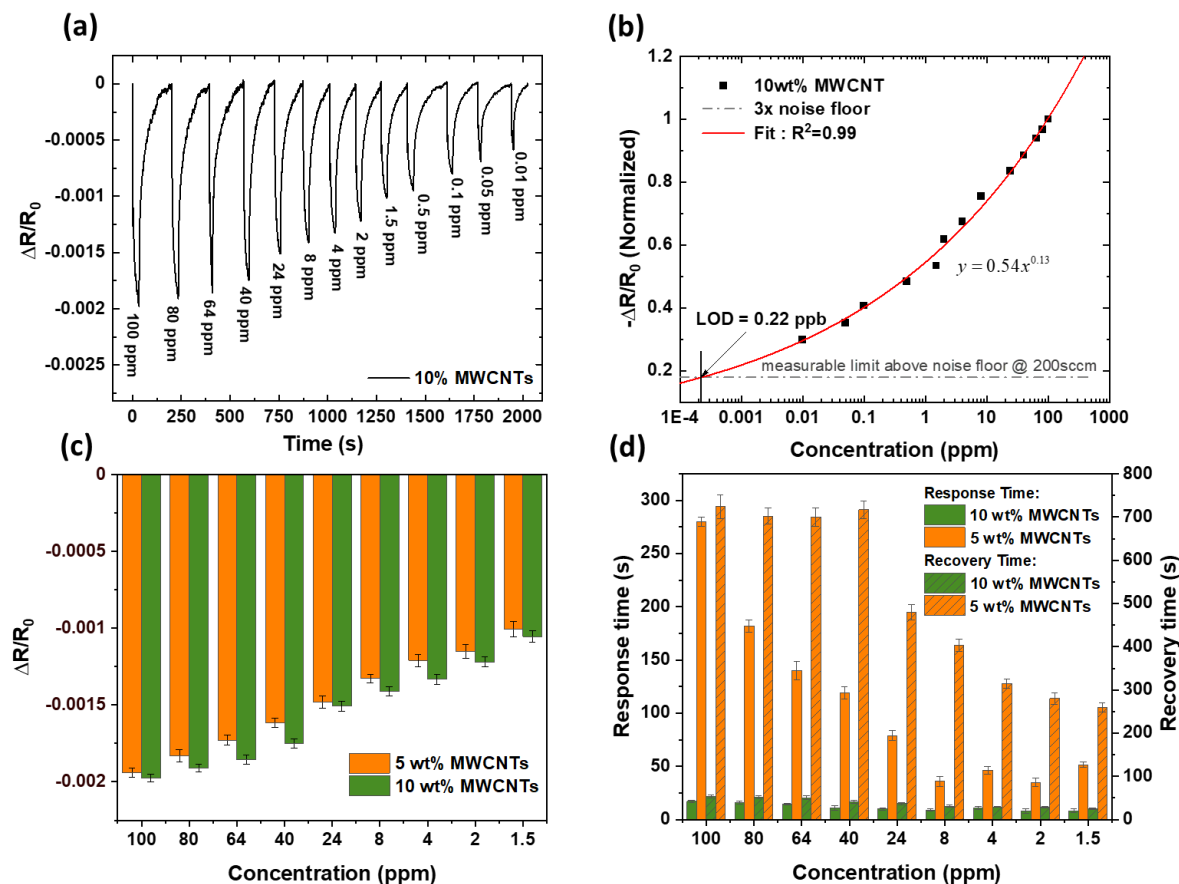


**Figure 4.12 a)** The dynamic response/recovery signals of the sensor with ZIF-8/10wt%MWCNTs for CH<sub>4</sub> at a total flow rate of 200 sccm: As it is evident our sensor shows very good response in this range of concentrations, even as low as 10 ppb. **b)** Negative normalized resistance changes as a function of CH<sub>4</sub> concentration depicting the LOD from power law fit of obtained response data. **c)** Comparative normalized resistance change responses, and **d)** response and recovery times of CH<sub>4</sub> for the sensor with 5 and 10wt% of MWCNTs. All error bars represent standard deviations of 7 measurements.

### 4.2.3 Response Mechanism Based on Structural and Electrical Properties of ZIF-8 and MWCNTs:

It is imperative to evaluate each role of MWCNTs and ZIF-8 in ZIF-8/MWCNTs nanocomposite in sensing mechanism that instigates significant responsivity of the sensor for ppb concentration level of CH<sub>4</sub> in atmospheric pressure with ultrahigh selectivity. This significant responsivity can be attributed to the role of conductive MWCNTs creating acceptor level ( $E_a$ ) within the band gap very close to the valence band. The ZIF-8/MWCNTs nanocomposite with narrower band gap and smaller activation energy ( $\Delta E$ ) (**Figure 4.5** and **Figure 4.6a**) facilitates easier share of electrons between the composite and the gas molecules. The ultrahigh selectivity of our sensor corresponds to the role of ZIF-8 as a porous material with ultra-high surface area providing different adsorption sites with varying electron affinity for adsorption of gas molecules. To better represent our sensor's selectivity mechanism, knowledge of these adsorption sites in ZIF-8 is crucial, which can be achieved by knowing the ZIF-8's crystal and chemical structure. ZIF-8 crystals are formed by the attack of unconjugated lone pairs of neutral Hmim linkers to the partially positive terminal zinc atoms to form cages (called "sodalite (SOD) cages") with 8 hexagonal windows and 6 square windows. These cages are packed together to form the SOD framework (**Figure 4.13a**) [259]. The sharpest XRD peak at 7.74° confirms ZIF-8 crystals have a SOD morphology, having 12 exposed (110) faces (**Figure 3.3**) [53]. Compared with many other MOFs, as ZIF-8 has no metal oxides cluster, its major adsorption sites are near imidazole rings instead of metal oxides cluster, shown in **Figure 4.13a** [260][261]. Moreover, owing to the absence of hydrogen bonding groups at the inner network of their pores and uncoordinated centers from the inorganic ligands, adsorption of water molecules inside its pores are energetically unfavorable [254][262]. However, the existence of N–H functionality of the residual Hmim on the outer surface of ZIF-8 which are the only

adsorption sites for making hydrogen bonding with water is responsible for limited adsorption of water vapour in our system (**Figure 4.13b**) [263]. Because of the electron-donating nature of water molecules and increasing in the resistance of our sensor in exposure to humidity (**Figure 4.7a**), it can be concluded that the obtained ZIF-8/MWCNTs nanocomposite has a p-type semiconducting behavior. In other words, in p-type semiconductors the charge carriers are holes, and the adsorbed water molecules neutralize the hole carriers in our system by donating the electron, resulting in an increase in the resistance.

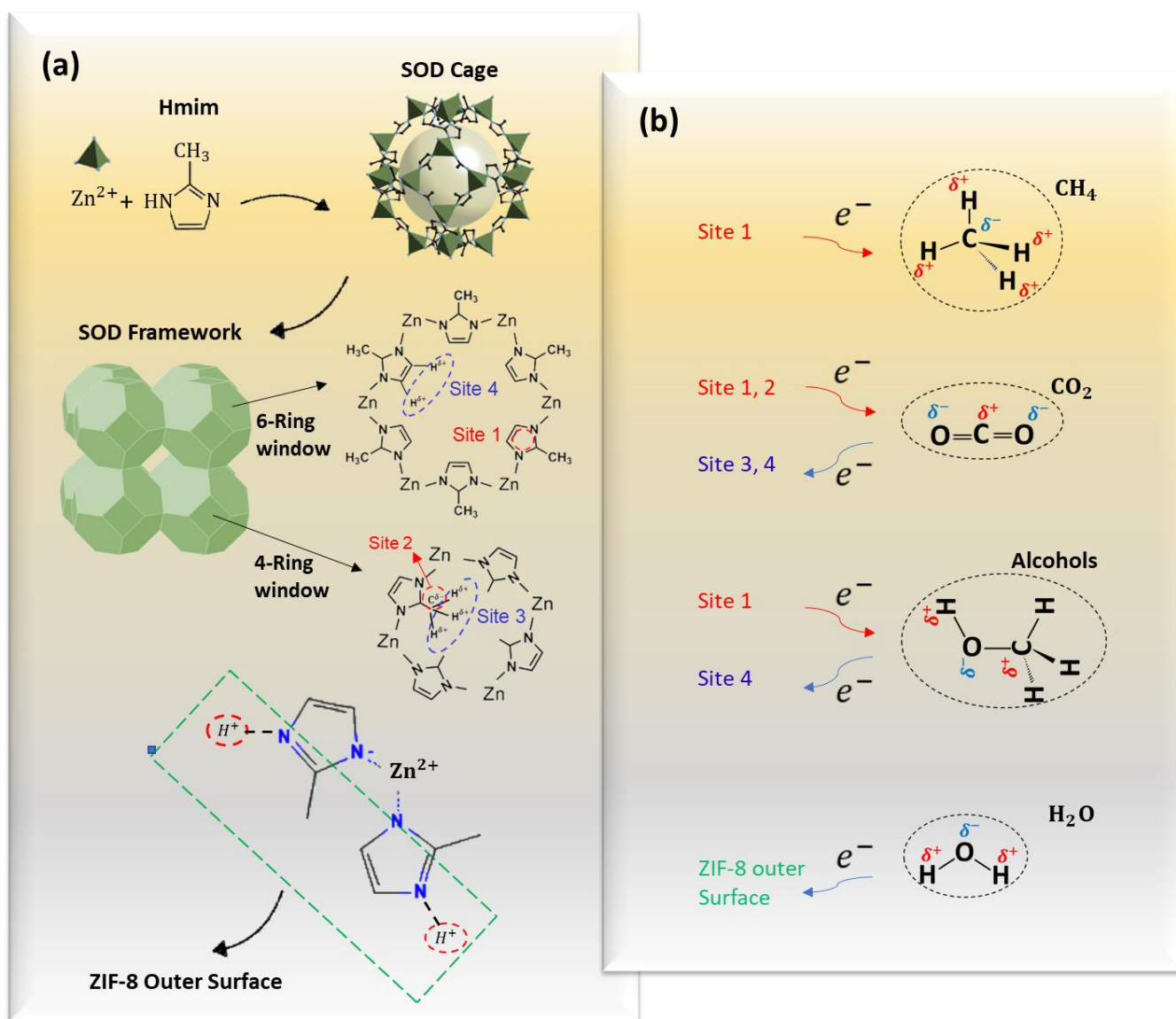


**Figure 4.13 a)** Schematic illustration of ZIF-8 crystal structure with different adsorption sites, **b)**

The adsorption sites for each of CH<sub>4</sub>, CO<sub>2</sub>, alcohols, and water vapours' physisorption into the ZIF-8 pores and surface via electron accepting or donating.

The exact adsorption sites for each of CH<sub>4</sub>, CO<sub>2</sub> and alcohols are shown in **Figure 4.13b**. Based on literatures [260], CH<sub>4</sub> is mostly populated at sites 1 through a sigma-  $\pi$  electron interaction between  $\pi$  electrons on the Hmim ring and sigma C-H bonds of CH<sub>4</sub>. Thus, CH<sub>4</sub> acts as an electron acceptor which results in the number of charge carrier (holes) increasing in our p-type semiconducting layer and decreases the resistance in our system (**Figure 4.5**). As for CO<sub>2</sub>, carbon atom is electron deficient and oxygen is electron rich, it can act either as electron acceptor or donor depending on the environment [264]. In ZIF-8 as reported by Liu et.al. [261], CO<sub>2</sub> molecules behave as electron acceptor in sites 1 and 2 via the quadrupole- $\pi$  electron interaction between the  $\pi$  electrons on the imidazole ring and the electron-deficient C <sup>$\delta^+$</sup>  (CO<sub>2</sub>), and the weak electrostatic interaction between the C <sup>$\delta^-$</sup>  (methyl) and C <sup>$\delta^+$</sup>  (CO<sub>2</sub>), respectively. However, CO<sub>2</sub> can also behave as electron donor in sites 3 and 4 through a hydrogen bond-like interaction between O <sup>$\delta^-$</sup>  (CO<sub>2</sub>) and H <sup>$\delta^+$</sup>  (methyl), and a very weak electrostatic interaction between the O <sup>$\delta^-$</sup>  (CO<sub>2</sub>) and the positive electrostatic potential of the H <sup>$\delta^+$</sup>  (Hmim), respectively. The slight increase in our sensor's resistance in exposure to CO<sub>2</sub> (**Figure 4.6a**) indicates that the possibility of CO<sub>2</sub> electron donating is somewhat higher than its electron accepting in our system, which is in agreements with experimental and molecular simulation of CO<sub>2</sub> adsorption on ZIF-8 [260].

Based on literature, alcohol sorption amounts in ZIFs are extremely low, and these low uptakes are disadvantageous for ZIF materials in alcohol extraction [265]. Moreover, ZIF-8 structure can be readily accessible for alcohols molecules through the sites 1, and 4 in six-ring windows (**Figure 4.13a**) [263]. They act as electron acceptor in site 1 through a sigma-  $\pi$  electron interaction between

$\pi$  electrons on the Hmim ring and sigma C-H bonds of alcohols molecules, and electron donor in site 4 via a very weak electrostatic interaction between the  $O^{\delta-}$  (alcohols) and the positive electrostatic potential of the  $H^{\delta+}$  (Hmim) (**Figure 4.13b**). However, our sensor shows negligible responses to methanol, ethanol, and isopropanol (**Figure 4.6a**), which can be regarded that in competition between electron donating and accepting, there is no winner and in overall we have negligible changes in charge density of our sensing layer.

**Table 4.1** Comparison table of different materials' sensing performance for  $CH_4$  detection.

Reproduced with permission from ref 1. Copyright (2020) Elsevier.

Materials	Operating Temperature	Response Time (s)	Sensing Reversibility	Selectivity	Limit of Detection (ppm)
<b>Metal oxides</b>	25°C-900°C (typically >150°C)	$10^0$ - $10^2$	Low-Medium	Low-Medium	$10^0$ - $10^3$
<b>Gd<sub>0.2</sub>La<sub>0.2</sub>Ce<sub>0.2</sub>Hf<sub>0.2</sub>Zr<sub>0.2</sub>O<sub>2</sub></b> [266]	RT	165-210	High	Medium	-
<b>Carbon</b>	Room Temperature (RT)–450°C	$10^1$ - $10^2$	Low-Medium	Low-Medium	$10^1$ - $10^4$
<b>f-MWCNT/Pd</b> [267]	RT	20	High	High	-
<b>SWCNT-P4VP-Pt-POM</b> [268]	RT	-	High	Low	29
<b>Conducting Polymers</b>	RT	$10^1$ - $10^2$	Low-Medium	Low-Medium	$10^2$ - $10^3$
<b>MOFs</b>	RT	$10^1$ - $10^2$	Medium-High	Medium	$10^2$ - $10^5$
<b>ZIF-8/MWCNTs (This work)</b>	RT	$10^0$ - $10^{1.2}$	High	High	$0.22 \times 10^{-3}$

### 4.3 Conclusions

We demonstrate the rapid, facile, and low-cost preparation of ZIF-8/MWCNTs nanocomposite and its first ever usage as a sensing layer of a chemiresistive sensor for the selective detection of  $CH_4$  at ambient condition. The obtained ZIF-8/MWCNTs nanocomposite with high surface area, narrow bandgap, rapid carrier mobility, high stability, and nontoxic peculiarity has outstanding sensing performance in compared to other reported materials for detection of  $CH_4$  (**Table 4.1**). Our composite approach renders unique p-type semiconducting behaviour to the sensing layer making possible the detection of  $CH_4$  at very low concentration of 10 ppb with the LOD  $\sim$  0.22 ppb.

Unprecedented sensitivity, appreciable repeatability, stability, reversibility, and high selectivity in presence of CO<sub>2</sub>, CO, NO<sub>2</sub>, NH<sub>3</sub>, alcohols, benzene and toluene at RT and ambient conditions are successfully demonstrated. Moreover, the low response of our sensor to humidity makes it an excellent candidate for real world applications. We explain the mechanism of selective response to CH<sub>4</sub> over CO<sub>2</sub>, alcohols and moisture based on different adsorption sites in ZIF-8 with varying electron affinity for adsorption of molecules. Beyond CH<sub>4</sub>, selectivity to other non-polar gases with low reactivity could be engineered for other real-time demanding applications. Similar carbon-engineered MOF-nanocomposites will have the promise of a new class of sensing materials that have selective response to low reactive gases via carrier manipulation in the energy band gap.

## **Chapter 5 : Application of ZIF-8/MWCNTs for Detection of VOCs Based QCM Sensor and as a Resistive Based Sensor for Detection of Acetone**

The contents of this chapter have been published in a paper entitled “ZIF-8/MWCNT-Nanocomposite Based-Resistive Sensor for Highly Selective Detection of Acetone in Parts-Per-Billion: Potential Noninvasive Diagnosis of Diabetes”. *Sensors and Actuators B: Chemical*, 2023, 393, 134197, <https://doi.org/10.1016/j.snb.2023.134197>.

### **5.1 Introduction**

Diabetes is a chronic health condition characterized by insufficient insulin production or improper utilization of insulin in the body, leading to elevated blood sugar levels. There are two main types of diabetes: type 1, which results from an autoimmune reaction that destroys the cells in the pancreas responsible for insulin production, and type 2, which occurs when the body becomes resistant to insulin and cannot regulate blood sugar effectively [54], [55]. The prevalence of diabetes is on the rise, with data from the World Health Organization (WHO) and other sources indicating that 422 million adults worldwide have the condition, and 1.6 million deaths are registered each year (WHO, 2023) [56], [57]. This trend highlights the urgent need for effective strategies to manage and monitor diabetes in order to reduce the risk of complications such as diabetic coma and death.

In clinical studies conducted on diabetic and prediabetic patients, blood sugar and ketone bodies are typically monitored through blood tests to diagnose all forms of diabetes [269]. However, this traditional method involves pricking the finger to draw a drop of blood and inserting it onto a strip for electronic reading, which can be painful, invasive, and even unsafe for some individuals.

Moreover, diabetes management often requires frequent blood glucose monitoring, making this method cumbersome [55]. Consequently, non-invasive and simpler diagnostic techniques, such as human breath analysis, hold great promise for diabetes detection and monitoring.

Patients with diabetes experience a shift in their body's energy production and body uses fats instead of glucose to produce energy, resulting in the overproduction of ketones such as acetone [55], [270]. These ketones are eliminated from the body through urine, sweat, and breath, making acetone a valuable biomarker for diabetes mellitus, particularly in type 1 [271]. While blood glucose measurements are commonly used for diagnosis, breath analysis has been shown to provide more precise control over a patient's diabetic condition by providing real-time measurements of acetone concentration, which strongly correlates with ketone concentration in the blood [146].

Various sensitive and selective breath analysis techniques, including gas chromatography coupled to mass spectrometry, high-performance liquid chromatography, proton transfer reaction with mass spectrometry, gas chromatography equipped with a flame ionization detector, ion mobility spectrometry, selected ion flow tube-mass spectrometry, laser photoacoustic spectrometry, have been proposed for detecting acetone non-invasively [55], [58]–[62]. However, these techniques are costly, non-portable, and sophisticated, limiting their practical use for daily point-of-care diabetes management [63]. Recent studies are focusing on developing non-invasive nanomaterial-based gas sensors that can detect acetone at room RT and atmospheric pressure, allowing for the creation of portable, affordable, and easy-to-use devices for diabetes management.

There have been significant efforts to develop various nanomaterials, including metal oxides, graphene-based composites, carbon nanotubes, and polymers, for the detection of acetone [57], [64]–[66]. Acetone concentration levels in exhaled breath are typically in the range of 0.2–1.8 ppm and 1.25–2.5 ppm for healthy individuals and those with diabetes, respectively [57], [67].

However, some individuals with type 1 diabetes may have acetone concentration levels as high as 25 ppm [57], [59], [67]. Despite all these efforts, most of nanomaterials could only detect acetone at concentrations above 10 ppm at RT (25°C), which is outside the range of exhaled acetone levels [55], [57], [64]–[66]. Additionally, exhaled breath contains not only acetone but also carbon dioxide (CO<sub>2</sub>), water, and thousands of other VOCs such as methanol, isoprene, ethanol, and other alcohols [272], [273]. As a result, these nanomaterials often lack the selectivity required to detect acetone accurately in the presence of these other gases/vapours, limiting their usefulness for acetone breath sensors.

To enhance the sensitivity and selectivity of gas/vapour detection, maximizing the specific surface area and porosity is crucial as gas reactions mainly occur on the surface of materials. Nanoporous materials like MOFs are a promising option due to their high surface area, permanent porosity, tunable pore size, and functionalizable internal pore surfaces, which provide active sites with varying electron affinity. MOFs self-assemble via coordination bonds of metal nodes with organic ligands, presenting a novel class of thermally stable and chemically inert crystalline hybrid nanoporous material [10], [28], [29]. Previous studies have explored MOFs for their enhanced chemical sensitivity and selectivity in detecting acetone and other VOCs [68], [69]. Despite these promising features, there is still a need to improve the sensitivity, selectivity, and water resistivity of MOFs to make them widely usable for acetone breath sensors. Detecting acetone in human exhaled breath with high sensitivity and selectivity is crucial for the diagnosis and monitoring of diabetes. However, it is challenging to obtain a reliable response to parts-per-billion (ppb) levels of acetone while avoiding cross-sensitivity due to the large amount of moisture and CO<sub>2</sub> present in exhaled breath. To address this issue, we focused on MOFs and chose ZIF-8 due to its low water affinity and stability in ambient conditions. However, ZIF-8 alone has the disadvantage of low

sorption capacity of VOCs at atmospheric pressure and RT. In this study, we significantly enhanced the VOCs sorption capacity by developing a nanocomposite of ZIF-8 with multiwall-carbon-nanotubes (MWCNTs) and demonstrated various VOCs sorption on ZIF-8/MWCNT-coated QCM sensor under ambient conditions. However, selectivity towards acetone, a crucial biomarker for diabetes, is lacking when other VOCs are present. Therefore, we conducted an investigation on different sensing platforms with different sensing mechanisms to achieve selectivity. We used the ZIF-8/MWCNT nanocomposite as a sensing layer on either QCM or interdigitated electrode (IDE) chip at RT (25°C). We systematically investigated the sensor's performance in terms of responsivity, reversibility, selectivity, response and recovery time, sensitivity, repeatability, and determined the LOD. Our findings demonstrate that the ZIF-8/MWCNT-coated chemiresistive sensor is highly sensitive and selective towards acetone at ppb levels with a quick response and recovery time. Overall, our study provides a promising approach for the sensitive and selective detection of acetone in human exhaled breath, which has potential applications in the diagnosis and monitoring of diabetes.

## **5.2 Results and Discussion**

### **5.2.1 Characterization of ZIF-8, MWCNTs and ZIF-8/MWCNT Nanocomposite**

This work utilizes an in-situ sonochemical synthesis method to create ZIF-8 and ZIF-8/MWCNT nanocomposite. Rather than utilizing functionalized-MWCNTs for making MOF/MWCNT nanocomposite, unmodified MWCNTs were used. This decision was made due to the possibility of functionalization resulting in the loss of desirable properties, such as hydrophobicity, which is not ideal for gas sensing applications. The synthesized ZIF-8 and ZIF-8/MWCNT nanocomposite

and MWCNTs were characterized using various methods, including FT-IR spectroscopy (**Figure 3.1**), Raman spectroscopy (**Figure 3.2**), XRD analysis (**Figure 3.3**), UV-vis spectroscopy (**Figure 3.4**), and BET analysis (**Figure 3.5**). FE-SEM/EDX analysis (**Figure 3.6 and 3.7**) were performed for ZIF-8 and ZIF-8/MWCNTs.

Using a Tauc plot analysis (Eq. (4-1)) of the UV-Vis absorption spectra, the optical band gaps ( $E_g$ ) of ZIF-8, MWCNTs, and ZIF-8/MWCNT have been determined (**Figure 4.2a**). The results indicate that the composite of ZIF-8 with bare MWCNTs exhibits a semiconducting behavior with a narrow band gap, which could potentially enhance the gas-sensing performance of the material. This is due to the ease of electron sharing to make van der Waals interaction with the target gas/vapour, as explained in our previous publication [93].

## 5.2.2 Sensor Performance Evaluation

In order to assess the sensing performance of ZIF-8 and ZIF-8/MWCNT nanocomposites (10wt% of MWCNTs), they were applied to QCM chips and IDE chips through spray coating. These chips were then exposed to predetermined concentrations of acetone, methanol, ethanol, and isopropanol. Upon exposure to different gases or vapours at RT (25 C°), the molecules are physically adsorbed into the pores and surfaces of the ZIF-8 material through van der Waals interaction. This adsorption causes an increase in the mass of the QCM crystal, leading to a decrease in its resonance frequency. With IDE-based chemiresistive sensors, the van der Waals interaction causes changes in resistance through the transfer of electrons between the gas/vapour molecules and the ZIF-8/MWCNT layer.

To explore how incorporating MWCNTs with ZIF-8 affects its sensing capabilities, QCM chips coated with ZIF-8 and ZIF-8/MWCNT nanocomposite were exposed to 100 sccm dry air to establish the baseline frequency ( $F_0$ ). They were then exposed to varying concentrations (0.62 - 20

ppm) of target VOCs (acetone, IPA, ethanol, and methanol) at the same flow rate until the sensor response reached a steady state. Afterward, the baseline was restored by cycling the flow of dry air. **Figure 5.1a** shows that the responses of the ZIF-8-coated QCM sensor to acetone, IPA, ethanol, and methanol vapours are insignificant ( $\Delta F \cong 0$ ). However, **Figure 5.1b** shows that the ZIF-8/MWCNT-coated QCM sensor displays substantial responsiveness to all of these VOCs down to 0.62 ppm. This phenomenon can be attributed to the smaller band gap of the composite (as depicted in **Figure 4.2a**), which facilitates electron sharing between the composite and the gas/vapour molecules, leading to a van der Waals interaction and higher gas adsorption in the composite as compared to pure ZIF-8 [93].

Although the ZIF-8/MWCNTs nanocomposite resulted in a significant improvement in the sorption of VOCs, it is essential to achieve chemical selectivity towards acetone when designing an acetone sensor. Thus, we investigated the different sensing platforms with different response mechanisms on chemical selectivity. We developed a ZIF-8/MWCNT-coated chemiresistive sensor and compared its performance with the ZIF-8/MWCNT-coated QCM sensor. Our results indicated that the ZIF-8/MWCNT-coated chemiresistive sensor demonstrated high selectivity towards acetone and had negligible responses to other VOCs such as IPA, ethanol, and methanol (**Figure 5.1c**). This high selectivity can be attributed to the different sensing mechanism of the chemiresistive sensor, which is discussed in detail in section 3.3, as opposed to the gravimetric QCM sensor used above. This research work highlights how different sensing mechanisms can be exploited to achieve chemical selectivity.

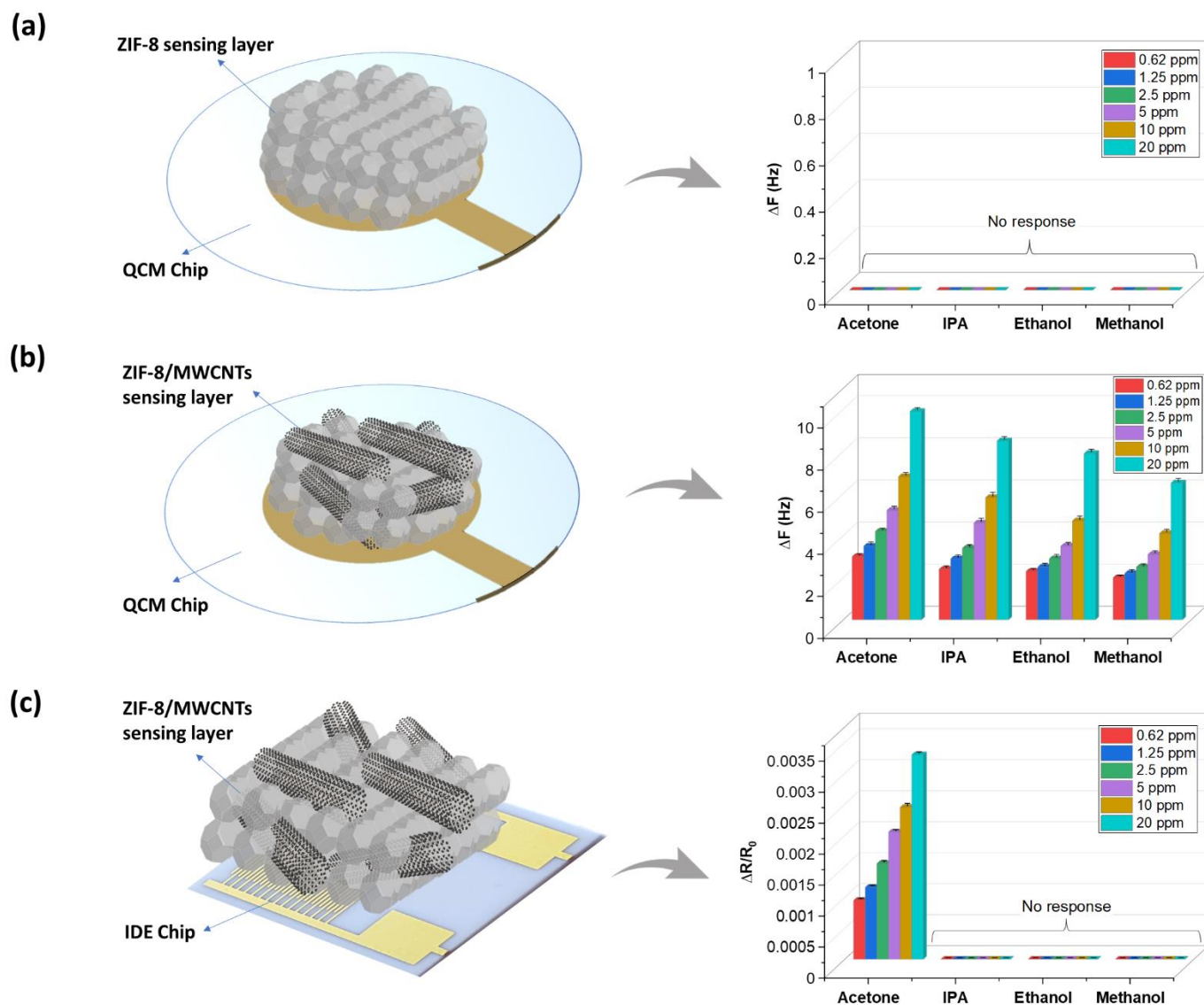
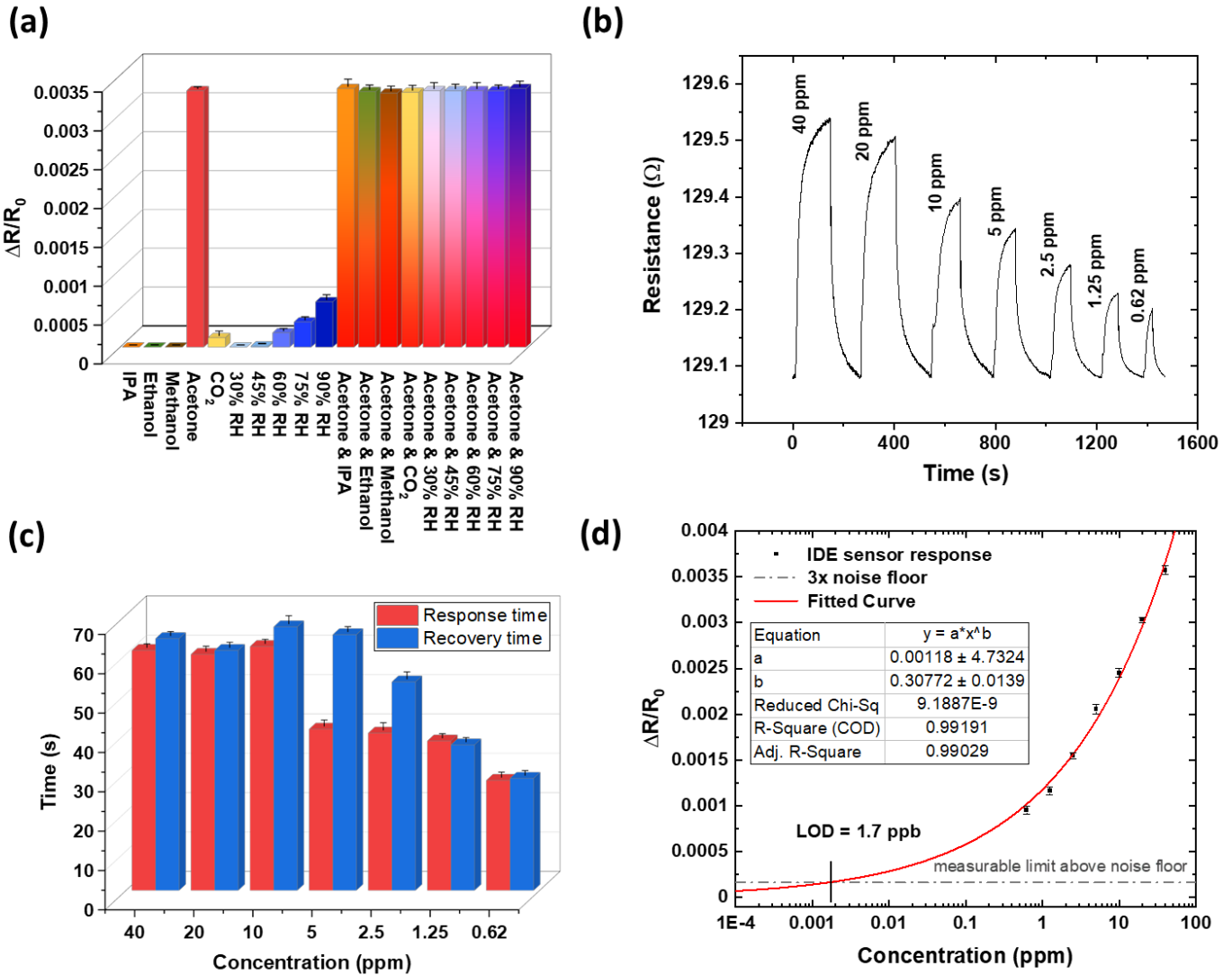


**Figure 5.1** Sensing responses of **a)** ZIF-8-coated QCM sensor, **b)** ZIF-8/MWCNT-coated QCM sensor, and **c)** ZIF-8/MWCNT-coated IDE chemiresistive sensor to varying concentrations (0.62-20 ppm) of acetone, IPA, ethanol, and methanol at RT (25 C°), respectively. All error bars represent standard deviations of seven measurements.

To further investigate the potential of our ZIF-8/MWCNT-coated chemiresistive sensor for diabetes diagnosis and monitoring through breath analysis, various parameters were studied, including selectivity, reversibility, response and recovery time, repeatability, and LOD, as shown in **Figure 5.2**. The selectivity of our ZIF-8/MWCNT-coated chemiresistive sensor towards acetone was evaluated in the presence of other VOCs commonly found in human exhaled breath, such as IPA, ethanol, methanol, CO<sub>2</sub>, and different percentage of RH. As can be seen in **Figure 5.2a**, the responses of our sensor to IPA, ethanol, methanol, and RH less than 60% are negligible. Moreover, the sensor response to 60-90% RH remains significantly less than that to 0.62 ppm of acetone (**Figure 5.2e**). Binary mixtures containing 20 ppm of acetone and each of the gas/vapours mentioned, and varying RH levels from 30 to 90% were tested. Notably, the chemiresistive sensor exhibited nearly identical responses when compared to 20 ppm of acetone alone, thereby confirming its selective sensing capabilities even in the presence of other gas/vapor. Although, the average RH of exhaled breath is reported around 66-76% [274], our sensor's response to acetone remained unaffected by humidity, even at extremely high RH levels (>75%) as shown in **Figure 5.2a** and **e**. This chemical selectivity can be attributed to ZIF-8's varying adsorption sites with different electron affinity and the specific sensing mechanism of chemiresistive sensors, as explained in detail in section 3.3.

Reversibility of the ZIF-8/MWCNT-coated chemiresistive sensor was confirmed by exposing it to repeating cycles of acetone at varying concentrations (0.62-40 ppm) and dry air flow to recover back to the baseline, as shown in **Figure 5.2b**. The response and recovery times for acetone were also determined and observed to be typically within a minute (**Figure 5.2c**). For the determination of LOD, the relative resistance change as a function of acetone concentration was normalized and fitted as a power-law dependence (**Figure 5.2d**), with the x-intercept representing the LOD of ~1.7

ppb. The normalized minimum measurable limit was determined to be on the order of 0.0002, corresponding to the 3x noise floor in exposure to a flow of dry air. The error bars in **Figure 5.2d** represent standard deviations for measurements taken from seven independent experiments, which ensure repeatability.



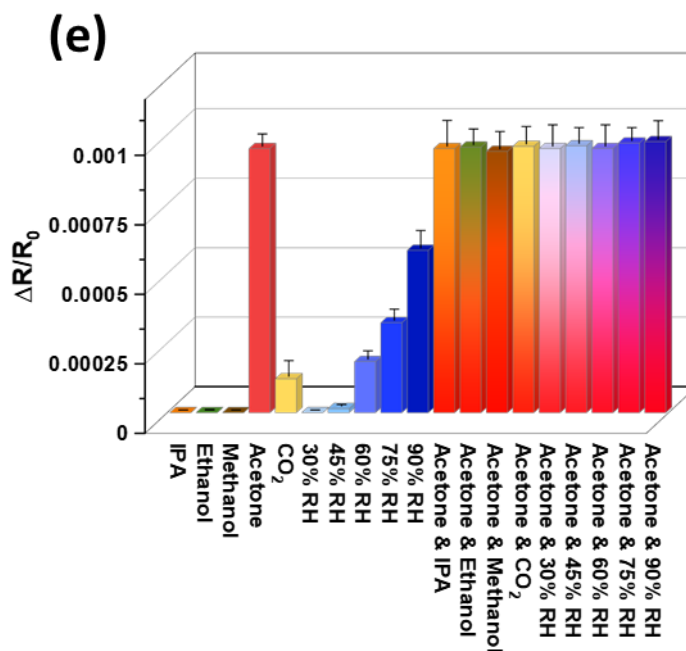


**Figure 5.2 a)** Normalized resistance changes of the ZIF-8/MWCNT-coated chemiresistive sensor toward 20 ppm of IPA, 20 ppm of ethanol, 20 ppm of methanol, 20 ppm of acetone, 900 ppm of CO<sub>2</sub>, and varying RH levels (30-90% RH), and selectivity tests of 20 ppm acetone in a binary mixture in presence of 20 ppm of IPA, 20 ppm of ethanol, 20 ppm of methanol, 900 ppm of CO<sub>2</sub>, and varying RH levels (30-90% RH) at a total flow rate of 100 sccm, respectively. **b)** The dynamic response/recovery signals of the chemiresistive sensor for acetone at a total flow rate of 100 sccm: as it is evident the chemiresistive sensor shows complete reversibility and good response in this range of concentrations, even as low concentration as 0.62 ppm. **c)** Acetone response and recovery times for the ZIF-8/MWCNT-coated chemiresistive sensor as a function of acetone concentration. **d)** Normalized resistance changes as a function of acetone concentration depicting the LOD from power law fit of obtained response data. All error bars represent standard deviations of seven measurements. **e)** Normalized resistance changes of the ZIF-8/MWCNT-coated chemiresistive sensor toward 20 ppm of IPA, 20 ppm of ethanol, 20 ppm

of methanol, 0.62 ppm of acetone, 900 ppm of CO<sub>2</sub>, and varying RH levels (30-90% RH), and selectivity tests of 0.62 ppm of acetone in a binary mixture in presence of 20 ppm of IPA, 20 ppm of ethanol, 20 ppm of methanol, 900 ppm of CO<sub>2</sub>, and varying RH levels (30-90% RH) at a total flow rate of 100 sccm, respectively.

### 5.2.3 Sensing Mechanisms

The low sorption amounts of alcohols and acetone in ZIFs at atmospheric pressure and RT, as evidenced by the literature [93], [265], [275], are disadvantageous characteristics of these materials. This was demonstrated experimentally with the ZIF-8-coated QCM sensor, which did exhibit negligible responses to acetone, IPA, ethanol, and methanol at atmospheric pressure and RT (25°C), as shown in **Figure 5.1a**. The lack of changes in the mass of the QCM sensor indicates that there is negligible adsorption of these analytes in our ZIF-8 pores. This is due to the absence of hydrogen bond groups at the inner surface of the ZIF-8 material and uncoordinated centers from the inorganic pattern, which renders the adsorption of alcohols and acetone molecules inside their pores energetically unfavorable at atmospheric pressure, as explained by Zhang and Snurr [254] and Canivet et al. [262]. Furthermore, unlike many other MOFs, ZIF-8 does not possess metal oxides cluster [254], [262], which are the main sites for adsorption of alcohols and acetone through hydrogen bonds in other types of MOFs.

In this study, the low adsorption of alcohols and acetone in atmospheric pressure and RT by ZIF-8 (**Figure 5.1a**) has been addressed by creating a composite of ZIF-8 with MWCNTs (**Figure 5.1b**). The significant responsivity in the ZIF-8/MWCNT nanocomposite can be attributed to two factors: its higher BET surface area compared to pure ZIF-8 (**Table 3.1**), and the narrower band gap and p-type semiconducting behavior of ZIF-8/MWCNTs compared to pure ZIF-8 (**Figure**

**4.21)** [93]. However, literature shows that despite ZIF-8 possessing a high surface area, its response to VOCs is negligible at concentrations below 10% (100,000 ppm) or at relative pressures below 0.1 [276], [277]. This is due to the absence of hydrogen bond groups and uncoordinated centers on the inner surface of ZIF-8, making adsorption of alcohols and acetone energetically unfavorable at atmospheric pressure [254], [262]. This indicates that the influence of the high surface area in ZIF-8 becomes significant only at very high concentrations or elevated pressure when it comes to alcohols and acetone adsorption. The use of bare MWCNTs in ZIF-8/MWCNTs also lacks hydrogen bond groups, further hindering adsorption of low concentration of alcohols and acetone at atmospheric pressure. Therefore, the disparity in surface area between ZIF-8 and CNT-embedded ZIF-8 becomes noticeable only under high concentration or saturation of alcohols and acetone at elevated pressure. However, in our study that focuses on very low concentrations of VOCs at atmospheric pressure, the contribution of difference in BET surface area between the materials (**Table 3.1**) becomes comparatively less pronounced. Therefore, the enhanced uptake of VOCs in ZIF-8/MWCNTs can primarily be attributed to the narrower band gap and p-type semiconducting behavior of ZIF-8/MWCNTs compared to pure ZIF-8 (**Figure 4.2a**) [93]. The synthesized ZIF-8 nanoparticle exhibits intrinsic semiconducting properties with a 3.2 eV band gap [93]. However, the absence of free charge carriers in intrinsic semiconductors results in a high activation energy, which can impact gas-sensing performance. However, ZIF-8 composite with bare MWCNTs has a p-type semiconductor behavior with a narrower 2.87 eV band gap. The introduction of MWCNTs creates acceptor levels within the band gap, shifting the effective Fermi level and enabling easy electron sharing [93]. This narrower band gap facilitates improved electron sharing, thereby promoting more van der Waals interactions with the target gas and ultimately enhancing gas uptake [93].

The order of resonance frequency changes or responsivity of the ZIF-8/MWCNT-coated QCM sensor for the tested VOCs is as follows: acetone > IPA > ethanol > methanol. The results for IPA, ethanol, and methanol indicate that a higher molecular weight (molar mass) results in a higher frequency change (**Table 5.1**), which is consistent with previous research [278]–[280]. However, this generalization is not always the case, as our results shown in **Figure 5.1b**. Although acetone has a lower mass than IPA, the resulting frequency changes are higher due to its higher polarity (dipole moment) [280] (**Table 5.1**).

**Table 5.1** Summary of VOCs' properties.

<b>Analyte</b>	<b>Molar mass (g/mol)</b> [68][280]	<b>Dipole moment (D)</b> [68]
<b>Acetone</b>	58.08	2.88
<b>IPA</b>	60.10	1.66
<b>Ethanol</b>	46.07	1.69
<b>Methanol</b>	32.04	1.70

In the case of the ZIF-8/MWCNT-coated chemiresistive sensor, changes in resistance occur as a result of the physisorption of analyte molecules through van der Waals interactions with the ZIF-8/MWCNT layer, which can either accept or donate electrons. This process results in a negative ( $-\Delta e^-$ ), positive ( $+\Delta e^-$ ), or neutral ( $\Delta e^- = 0$ ) exchange of electrons between the sensing layer and gas/vapour analytes, leading to a decrease, increase, or no change in normalized resistance change ( $\Delta R/R_0$ ) in the nanocomposite, respectively. The synthesized ZIF-8/MWCNT exhibits p-type semiconductor behavior with holes as the charge carriers [93]. As shown in **Figure 5.3**, molecules such as acetone, IPA, ethanol, and methanol, which have electron-deficient carbon atoms and electron-rich oxygen atoms, can function as electron acceptors or donors depending on the ZIF-8's adsorption sites with varying electron affinity [93], [281]. The negligible resistance

changes observed in the ZIF-8/MWCNT-coated chemiresistive sensor to IPA, ethanol, and methanol suggest that there is no clear winner in the competition between electron donating and accepting of these analytes, resulting in an overall negligible change in the charge density of the nanocomposite layer ( $\Delta e^- = 0$ ). Moreover, although the chemiresistive sensor demonstrates only minimal positive responses ( $+\Delta e^-$ ) to  $\text{CO}_2$  and  $\text{H}_2\text{O}$ , it displays a substantial positive response ( $+\Delta e^-$ ) to acetone, suggesting that in our system,  $\text{CO}_2$  and  $\text{H}_2\text{O}$  are slightly and more likely to donate electrons than to accept them. In contrast, acetone exhibits a significantly higher propensity for electron donation than acceptance (as shown in **Figure 5.2a** and **5.3**).

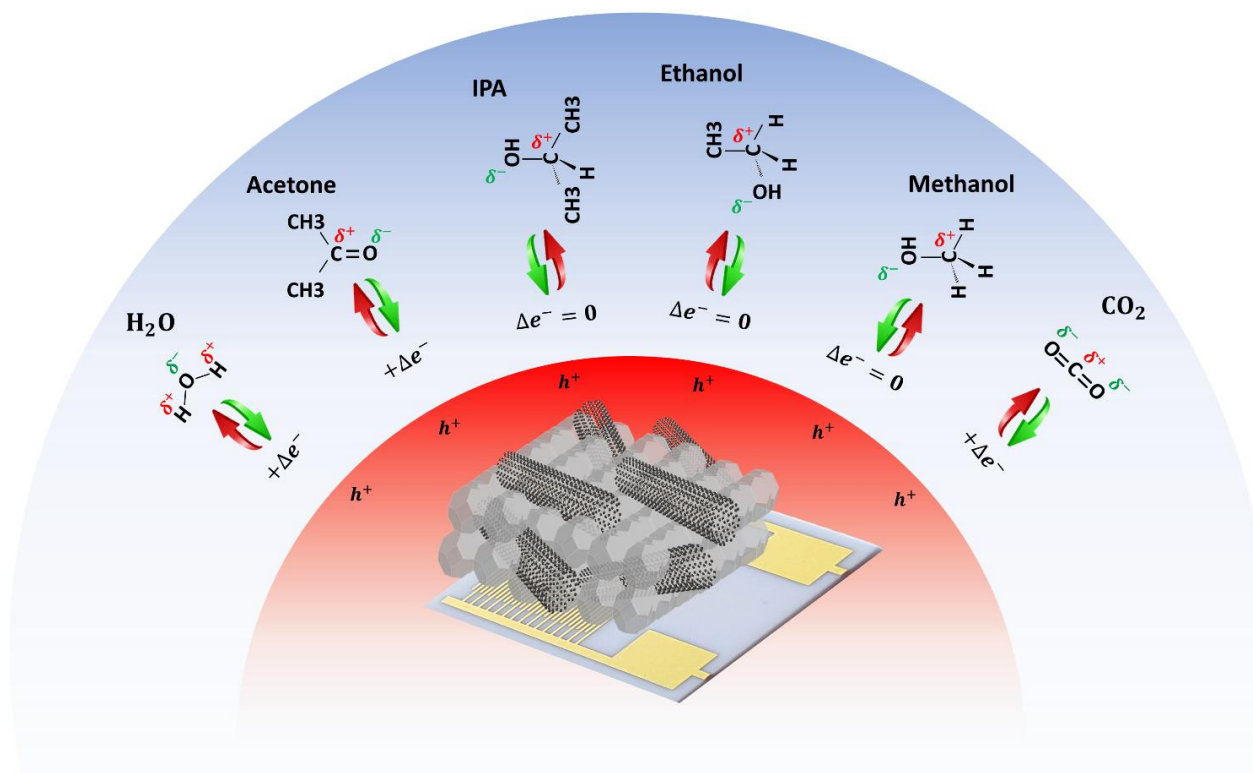


**Figure 5.3** a) Schematic illustration of water, acetone, IPA, ethanol, methanol, and  $\text{CO}_2$  molecules physisorption into the pores and surfaces of ZIF-8/MWCNT via electron accepting from or donating to ZIF-8/MWCNT layer and the net exchanged electrons ( $\Delta e^-$ ) from the sensing layer to them.

**Table 5.2** Comparison of Sensing Performance for Acetone Detection at RT with previous works.

Material	Testing concentration range	Limit of Detection (LOD)	Selectivity in mixture
PANI/Cellulose/WO <sub>3</sub> based Impedance sensor [150]	10-100 ppm	10 ppm	-
V <sub>2</sub> O <sub>5</sub> nanoneedles based resistive sensor [282]	1.7-140 ppm	0.941 ppm	-
SnO <sub>2</sub> based resistive sensor [283]	10-100 ppm	-	-
SnO <sub>2</sub> /rGO based resistive sensor [284]	10-2000 ppm	-	-
TiO <sub>2</sub> Nanotubes based resistive sensor [285]	10-1000 ppm	-	-
Ni/ZnO Nanorods based resistive sensor [286]	100 ppm	-	-
Na/ZnO Nanoflowers based resistive sensor [287]	1-500 ppm	0.09 ppm	-
VO <sub>2</sub> /ZnO based resistive sensor [288]	10-200 ppm	-	-
Cu-BTC-based PP capacitive sensor [68], [69]	250-1500 ppm	100 ppm	-
Cu-BTC-based IDE capacitive sensor [69]	250-1500 ppm	149 ppm	Yes
ZIF-8/MWCNTs nanocomposite (this work)	0.62-40 ppm	1.7 ppb	Yes

### 5.3 Conclusions

A significant improvement by addressing the disadvantage of ZIF-8's low sorption amounts of VOCs at atmospheric pressure and RT was achieved by synthesizing ZIF-8 into a nanocomposite with bare MWCNTs. The resultant ZIF-8/MWCNT-coated QCM sensor exhibited outstanding sorption performance in detecting low concentrations of VOCs at 0.62 ppm at atmospheric pressure and RT (25°C), compared to the ZIF-8-coated QCM sensor. This outstanding sorption performance could be attributed to the p-type semiconducting behavior of ZIF-8/MWCNT with a narrower band gap. A comparative study was conducted between the chemiresistive sensor and the gravimetric QCM sensor based on ZIF-8/MWCNT to investigate the effect of different sensing platforms with different sensing mechanisms on achieving high selectivity for acetone. This comparative study provides a significant reference to guide future studies on designing other gas sensors for achieving high selectivity. The results indicate that the ZIF-8/MWCNT-coated chemiresistive sensor exhibited a significant performance for acetone detection in terms of low

response to humidity, high selectivity, good repeatability, complete reversibility, and fast response time was achieved with a determined LOD of approximately 1.7 ppb at RT (25°C). This LOD is much lower than the concentration level of 1.8 ppm in the exhaled breath of diabetic patients. As obtaining a reliable response to ppb levels of acetone at RT and avoiding cross-sensitivity due to the presence of other gases and the large amount of moisture in exhaled breath are still great challenges (**Table 5.2**). Therefore, these results open a potential opportunity for a simple, inexpensive, and noninvasive diagnosis and monitoring of diabetes.

## **Chapter 6 : Application of ZIF-8/CNFs Nanocomposite as a Spectrally Selective Photodetector**

The contents of this chapter have been submitted in a paper entitled “Eco-friendly and High-Performance Photodetector based on Bandgap-Engineered MOFs/CNFs Nanocomposites for Violet Light Detection”, *Advanced optical material*, submitted.

### **6.1 Introduction**

Photodetectors have emerged as essential components in various technological domains, including optical communication, imaging, sensing, security, environmental monitoring, and medical diagnostics. The ability to harness and convert light signals into electrical signals has revolutionized these fields, enabling high-speed data transmission, precise imaging, and remote sensing.[70] Despite the considerable progress made in photodetection technologies, significant challenges persist. Conventional photodetectors, predominantly based on inorganic semiconductors like silicon and complementary metal oxide semiconductors, have been widely used due to their great compatibility with integrated circuits, which guarantees their application in miniaturized photodetectors and other featured devices [70]–[74]. Nonetheless, given the intrinsic drawbacks, e.g., high brittleness and complicated manufacturing process, these traditional photodetectors are limited in flexible applications and manufacturing cost-savings. Besides, due to the broadband absorption of inorganic semiconductors, spectrally selective detection of these photodetectors is unavailable without attached optical filters or photonic crystal surface patterning [74]. Traditional spectrometers typically utilize diffraction gratings or dichroic prisms within broad-spectrum photodetectors to achieve spectral selectivity. However, the intricate manufacturing processes and associated high cost have posed significant obstacles to their

widespread commercial adoption [74]. Therefore, nanomaterials have emerged as promising candidates for next-generation photodetectors to overcome the shortcomings of conventional photodetectors [70].

Nanomaterials in nonconventional device architectures have been extensively researched due to their size-dependent optical and electrical properties. Various nanomaterials, such as semiconducting nanoparticles, QDs, graphene, transition metal dichalcogenides, perovskite nanocrystals, and organic molecules have demonstrated intriguing optoelectronic properties and impressive photodetection performance [75]–[89]. However, each of these nanomaterials is accompanied by limitations such as toxicity, low responsivity, low quantum efficiency, slow response time, limited tunability, low stability, scalability, inadequate sensitivity in certain wavelength ranges, high cost, fabrication complexities, challenges in large-scale synthesis, challenges in device integration and compatibility with existing fabrication techniques, which hinder their widespread implementation [70], [74], [90], [91]. Among the emerging nanomaterials, CNFs, with their exceptional electrical conductivity, mechanical strength, and thermal stability, have exhibited promising potential as high-performance and cost-effective photodetectors [289]. However, to our knowledge, there is no study on CNF-based photodetectors. On the other hand, as CNF is a low band gap material [289], its selective performance could be hindered due to its broadband absorption. However, this limitation of CNFs could be addressed by integrating them with other materials to create composite structures for tuning the band gap.

The distinctive attributes of MOFs, characterized by their ultra-high surface area, tunable structures and properties, diverse chemical functionality, and diverse optical properties, have propelled them to the forefront of nanomaterial research [92], [93]. The versatility of these crystalline networks, composed of metal ions coordinated with organic ligands, has allowed

researchers to tailor MOFs for various applications, including gas storage, separation, catalysis, and sensing [68], [69], [92]–[98]. Their intrinsic light-harvesting abilities and potential for modification make them attractive candidates for photodetection. Incorporating MOFs into photodetectors can lead to enhanced light absorption, charge separation, selective and tailored photoresponse. While 2D MOFs and single crystal MOFs have demonstrated promising photodetection capabilities [94], [99]–[103], their 3D counterparts have faced inherent limitations in terms of limited carrier mobility and slow charge transport dynamics, hindering their ability to swiftly respond to photogenerated carriers [46], [47], [50]. Nonetheless, challenges associated with the synthesis of single crystal MOFs, high-quality and large area 2D MOF films, and their integration into device architectures hinder their widespread adoption. These constraints have motivated us to explore composite systems to leverage the strengths of 3D MOFs while addressing their weaknesses.

One of the paramount challenges in modern photodetection is achieving high selectivity in the identification of specific wavelengths or sources of light, which enhances the reliability and accuracy of photodetectors. This is especially crucial in applications such as environmental monitoring, medical imaging, optical communication, and intelligent optoelectronic devices where accurate discrimination of different light sources is essential [290]. The integration of different nanomaterials as a nanocomposite material holds great promise in addressing this challenge, as it combines the complementary properties of different materials to enable enhanced selectivity through tailored surface chemistry, materials' bandgaps, energy band structures and efficient charge separation [1], [93], [126], [133]. In this paper, we delve into the realm of photodetectors based on the novel MOFs nanocomposites with CNFs.

In this study, ZIF-8 was selected from the family of 3D MOFs due to its low water affinity and stability under ambient conditions. However, like many 3D MOFs, ZIF-8 exhibits low charge transport properties [93], and consequently limited optoelectronic responses. In contrast, CNFs typically demonstrate broad optical absorption across a wide spectral range, which poses constraints on their selectivity. The integration of ZIF-8 with CNFs presents a promising strategy to address the individual limitations of both materials. By combining ZIF-8's high surface area and porosity with CNFs' excellent conductivity, a nanocomposite material is created that manifests enhanced light absorption, improved photoresponse, efficient charge transport, and enhanced charge separation. This composite approach not only enables fine-tuning of optoelectronic properties but also establishes a platform for tailoring selectivity through band gap manipulation, eliminating the need for attaching optical filters. This unique attribute simplifies the fabrication of spectrally selective photodetectors, leading to reduced manufacturing costs. Furthermore, the study employs the spray coating method to fabricate the composite thin film on an interdigitated electrode (IDE) chip, streamlining the fabrication process and eliminating the complexity associated with current photodetectors' hybrid heterojunction. This approach holds potential for cost-effective, large-area thin film production of MOFs. The synthesis, characterization, and distinctive optoelectronic behavior of this composite material are explored comprehensively. Through an exhaustive investigation, improved sensitivity, response time, and spectral selectivity of this photodetector to violet light under RT and ambient conditions are demonstrated, presenting a strong case for their integration into diverse technological applications such as environmental monitoring (ozone detection, air and water quality, etc.), biomedical imaging, optical communication, astronomy and astrophysics, and security and authentication. This study

illuminates the potential of 3D MOFs nanocomposites to unlock new possibilities for applications in various fields requiring high-performance and spectrally selective photodetection.

## 6.2 Results and Discussion

### 6.2.1 Structural and Morphological Characterization of the ZIF-8, CNFs, and ZIF-8/CNFs Nanocomposite:

In this study, the ZIF-8/CNFs nanocomposite is synthesized through an in situ sonochemical and hydrothermal method, enabling the growth of ZIF-8 in the presence of bare CNFs. The resulting nanocomposite is then spray-coated as a thin film onto an interdigitated electrode (IDE) chip (**Figure 6.1a**). For further characterization, FT-IR spectroscopy (**Figure 3.9**), XRD analysis (**Figure 3.10**), and UV-vis spectroscopy (**Figure 3.11**) for bare CNFs, ZIF-8 and ZIF-8/CNFs nanocomposite, and FE-SEM/EDX analysis (**Figure 3.12** and **3.13**) for ZIF-8/CNFs nanocomposite have been performed.

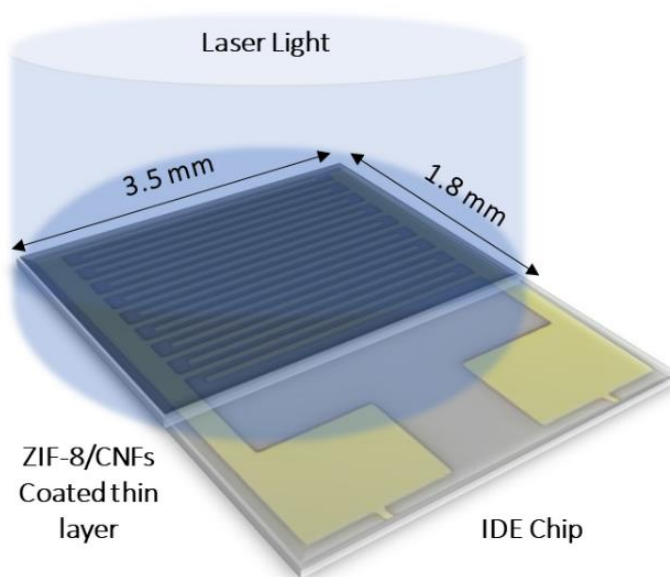


**Figure 6.1** Schematic of the photodetector device based on 8  $\mu\text{m}$  thick ZIF-8/CNFs spray-coated thin film on the surface of an IDE chip.

The band gaps ( $E_g$ ) of the materials were assessed through the analysis of their UV-Vis absorption spectra, employing a Tauc plot method (Eq. (4-1)) as depicted in **Figure 6.2**. The findings reveal that the individual band gaps of CNFs and ZIF-8 are 1.17 eV and 3.20 eV, respectively. Remarkably, the formation of a composite integrating these materials leads to a tailored band gap of 2.44 eV for the ZIF-8/CNFs nanocomposite.

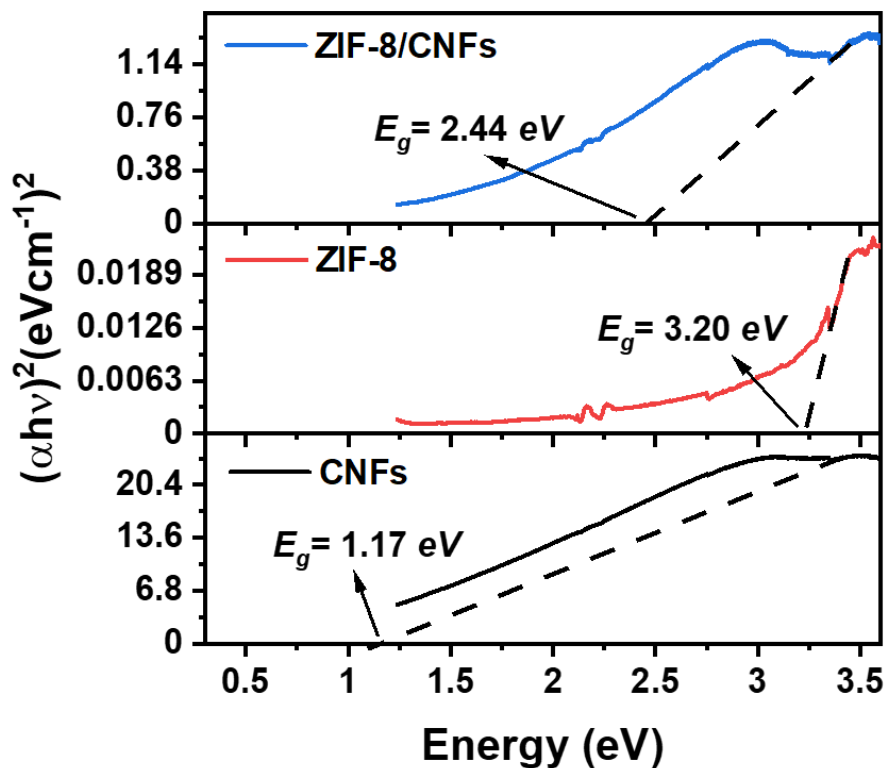


**Figure 6.2** Tauc's plots for the optical band gap energy determination of CNFs (black), ZIF-8 (red) and ZIF-8/CNFs nanocomposite (blue), respectively.

### 6.2.2 Sensor Performance Evaluation:

The optoelectronic characteristics of the photodetector based on the ZIF-8/CNFs nanocomposite were systematically investigated using a Keithley source measurement unit (SMU Model 2450). These investigations were conducted under RT and ambient conditions within a dark box to

prevent the influence of ambient light. Laser light sources emitting at wavelengths of 635 nm, 532 nm, and 404 nm were employed, with neutral density (ND) filters to adjust light power levels. Upon exposure to the laser illumination, electrons situated in the valence band of ZIF-8/CNFs absorbed photon energy, facilitating their transition from the valence band to the conduction band [89]. As the concentration of electron carriers increased, the photodetector's conductivity was correspondingly increased.

Preceding the photoelectronic property assessments, an examination of the ZIF-8/CNFs nanocomposite's electrical properties was conducted through application of a bias voltage spanning from -3 V to 3 V in dark condition (**Figure 6.3a**). The observed nonlinear current-voltage (I–V) behavior implies the establishment of a Schottky-type barrier within the devices [75]. With the incorporation of a ZIF-8 layer, the incident light absorption prompts the emergence of excitons (electron-hole pairs) at the Schottky-like ZIF-8/CNFs interface.

The selectivity of the ZIF-8/CNFs nanocomposite photodetector was subjected to comprehensive scrutiny through exposure to distinct light wavelengths of 404 nm, 532 nm, and 635 nm at a constant 100% light intensity, respectively (**Figure 6.3b**). As illustrated in **Figure 6.3b**, the current under 404 nm illumination registers an augmentation compared to the dark current. This enhancement can be attributed to the amplification of photogenerated carriers within the ZIF-8/CNFs nanocomposite film upon light absorption. In contrast, the photodetector exhibits negligible current variation in comparison to the dark current when exposed to photons with 532 nm and 635 nm wavelengths. In photodetectors, photon absorption and consequent photocurrent generation are governed by the material's bandgap energy. Shorter incident light wavelengths of 404 nm carry higher energy, facilitating electron excitation across the bandgap and yielding a photocurrent. In contrast, longer wavelengths of 532 nm and 635 nm carry comparatively lower

energy, posing a greater challenge for photons to induce electron transitions and consequently leading to the absence of photocurrent [77]. This underscores the photodetector's outstanding selectivity, highlighting its potential for applications demanding highly selective photodetection. Expanding on the observed wavelength selectivity pattern for 404 nm, subsequent investigations were focused on evaluating the sensor's photodetection performance tailored specifically to this wavelength.

To account for the influence of light intensity, Figure 3c illustrates the I-V characteristic under 404 nm illumination, spanning a range of light intensities from  $72 \mu\text{W}/\text{cm}^2$  to  $72 \text{mW}/\text{cm}^2$  (**Figure 6.3c**). With an increase in the intensity of optical power illumination, there is a correlated elevation in the current, attributed to the augmented population of photogenerated carriers (**Figure 6.3c**).

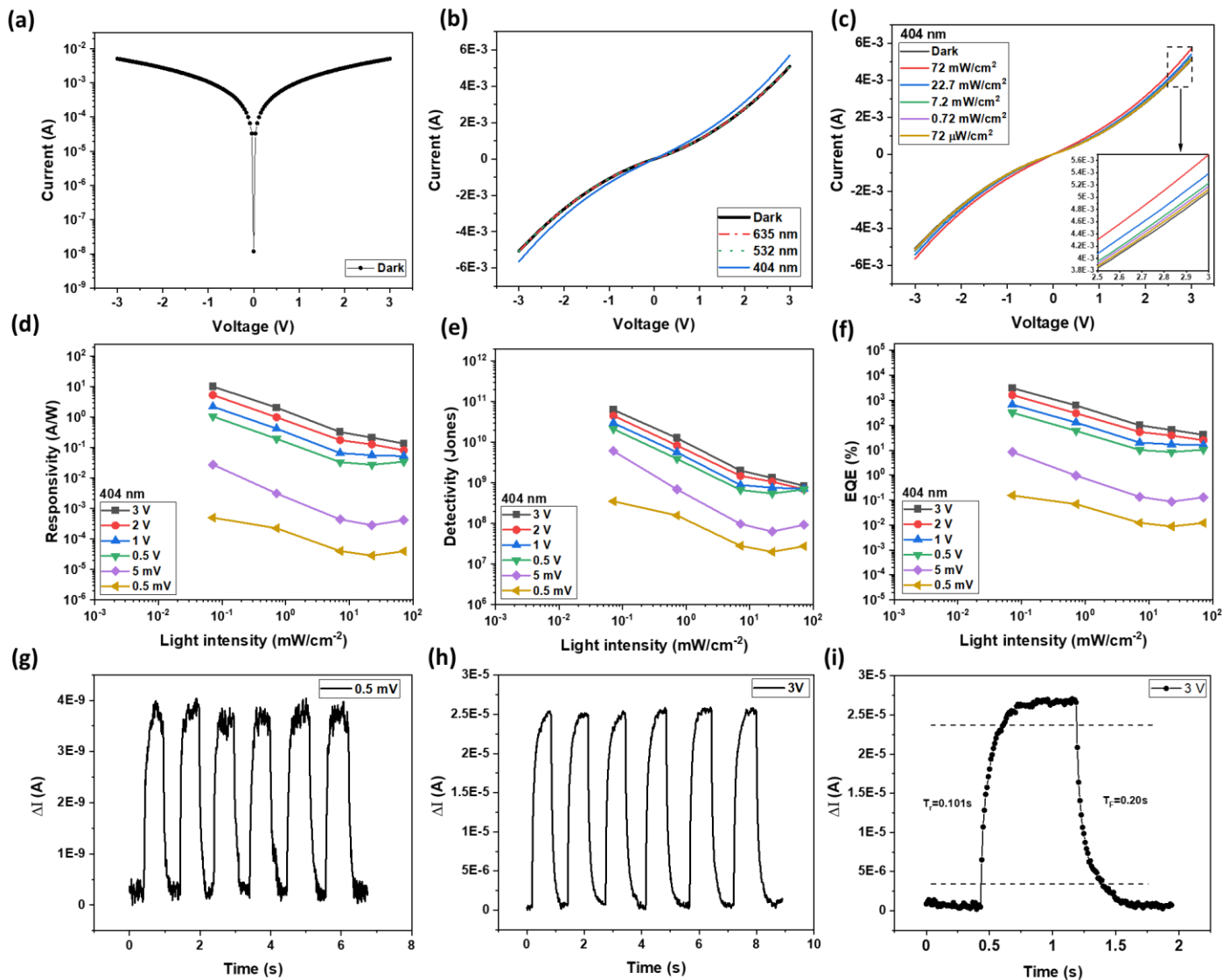


**Figure 6.3** Photoelectric properties of ZIF-8/CNFs photodetector at RT. **a)** I–V characteristics ZIF-8/CNFs under -3 to 3 V bias voltage in a dark environment. **b)** Response of the PD under dark and laser illuminated of 404, 532, and 535 nm to show selectivity. **c)** I–V curves for different power intensities of 404 nm wavelength. **d)** The power-dependent responsivity, **e)** the light density-dependent detectivity, and **f)** External quantum efficiency (EQE) of the PD versus optical power intensity at different bias voltage. Photoresponse of the PD as a function of time at

bias voltage of **g**) 0.0005 V and **h**) 3 V. **i**) Rising and falling edges for estimating rise time ( $T_r$ ) and the fall time ( $T_f$ ) the PD under 404 nm laser illumination at bias voltage of 3V.

For further assessment of the photodetector performance, the parameters of the figure of merit including responsivity (R), specific detectivity (D), and external quantum efficiency (EQE) were evaluated under 404 nm illumination, considering various light intensities and bias voltage levels.

These parameters are defined by the following equations:

$$R = \frac{I_p - I_d}{P_{opt} \times A} \quad (6-1)$$

$$D = \frac{R\sqrt{A}}{\sqrt{2qI_d}} \quad (6-2)$$

$$EQE = R \times \frac{1240}{\lambda} \times 100\% \quad (6-3)$$

where  $I_d$  is the dark current (in A),  $I_p$  is the current under illumination (in A),  $P_{opt}$  is the power density of incident light (in mW/cm<sup>2</sup>),  $A$  is the total effective illuminated area (0.063 cm<sup>2</sup>) of the device,  $q$  is electron charge ( $1.602176634 \times 10^{-19}$ ), and  $\lambda$  is excitation wavelength (404 nm). The interrelation of these parameters with light intensity under various bias voltages is presented for comparison in **Figure 6.3d-f**. Upon the application of bias voltage, an external electric field forms at the junction interface, heightening the separation efficiency of photogenerated carriers. This augmentation subsequently elevates the values of R, D, and EQE, which progressively rise with the increase in applied voltage (**Figure 6.3d-f**) [77]. For each bias voltage, R, D, and EQE experience amplification at lower light power intensity but diminish with increasing light power intensity (**Figure 6.3d-f**).

The maximum R, D, and EQE values for 404 nm illumination are found to be 10 A/W,  $6.31 \times 10^{10}$  Jones, and 3112% at low light illumination power intensity of 72  $\mu$ W/cm<sup>2</sup> under a bias voltage of 3 V. Remarkably, these values, particularly at the lowest power density, underscore the ultrahigh

sensitivity of our photodetector. Notably, the achieved maximum EQE surpasses 100%, an exceptional achievement surpassing previous reports (referenced in **Table 6.1**). These exceptional outcomes arise from the abundant surface-to-volume ratio of ZIF-8 nanoparticles and CNFs, yielding remarkable photon absorption and consequent photocurrent generation. Moreover, the interface between ZIF-8 and CNFs facilitates exciton separation and carrier extraction, further bolstering the photocurrent effects.

The time-switching responses ( $I-t$ ) of the photodetector were assessed at bias voltages of 0.5 mV and 3 V (**Figure 6.3g and h**). A repeated sequence of six on-off switching cycles illustrates the consistent rise and decay of current changes ( $\Delta I = I_p - I_D$ , where  $I_p$  is the current under illumination and  $I_D$  is the initial current in dark) demonstrating a uniform pattern across each cycle. As shown in **Figure 6.3g and 3h**, while the enhancement of photoresponsivity is evident with increased external bias voltage, the device remarkably maintains a high photoresponsivity even at an extremely low external bias voltage of 0.5 mV. This observation underscores the photodetector's capacity to effectively accomplish photodetection tasks while operating with minimal bias voltage requirements, signifying its promising suitability for ultra-low power applications.

Two other fundamental properties of the photoresponse are the rise time ( $T_r$ ) and fall time ( $T_f$ ), as depicted in **Figure 6.3f**. The rise time refers to the duration needed to transition from 10% to 90% of the maximum current, while the fall time pertains to the time taken to transition from 90% to 10% of the falling edge. At a wavelength of 404 nm and a bias voltage of 3 V, the ZIF-8/CNFs photodetector exhibits response times of 101 ms and 200 ms, respectively.

**Table 6.1** Comparison of this work with earlier reported MOFs based photodetector.

Materials	Temperature (C)	Bias (V)	Wavelength (nm)	Responsivity (A/W)	Detectivity (Jones)	EQE (%)	T <sub>rise</sub> /T <sub>fall</sub> (s)	Working Wavelength (nm)	Reference
<b>2D MOF [Ni-CAT-1]/Bi<sub>2</sub>Se<sub>3</sub> hybrid heterojunction</b>	RT	60	1500	4725	$3.5 \times 10^{13}$	4185	0.130/0.006	500-2000	[99]
<b>2D MOF [Fe<sub>3</sub>(THT)<sub>2</sub>(NH<sub>4</sub>)<sub>3</sub>]</b>	-196	-1	785	0.142	$7 \times 10^8$	-	2.3/2.15	400–1575	[100]
<b>Single crystalline SMOF [heterochiral AlaNDI-Ca]</b>	RT	50	365	0.650	$4.8 \times 10^{11}$	221	150/163	365	[101]
<b>Single crystalline MOF [HKUST-1]</b>	-	-	-	-	-	-	0.1/-	600–1000	[102]
<b>Eu–MOF</b>	RT	0	254	0.0002	$1.015 \times 10^{10}$	-	0.98/0.122	245	[103]
<b>SnO<sub>2</sub>/MOF [ZrBDC]/TFB heterojunction</b>	40	0	254	0.0017	$7.85 \times 10^{10}$	0.78	0.08/0.150	254	[94]
<b>ZIF-8/CNFs nanocomposite</b>	RT	3	404	10.2	$6.31 \times 10^{10}$	3112	0.101/0.149	404	This work

### 6.3 Conclusions

By leveraging ZIF-8's impressive surface area and porosity alongside CNFs' outstanding conductivity, we have created a nanocomposite material that excels in light absorption, photoresponse, charge transport, and charge separation. This composite approach not only allows for precise control over photoelectronic properties but also establishes a platform for selectivity modulation through band gap manipulation, eliminating the need for external optical filters. This unique attribute streamlines the fabrication of spectrally selective photodetectors, ultimately reducing manufacturing costs. Throughout this comprehensive investigation, we have demonstrated improved sensitivity, response time, and spectral selectivity of our photodetector to violet light under RT and ambient conditions. These findings underscore the potential of 3D MOF nanocomposites to advance photodetection technology and unlock new possibilities for their integration into diverse technological applications such as environmental monitoring (ozone detection, air and water quality monitoring, etc.), biomedical imaging, optical communication, astronomy and astrophysics, and security and authentication. This study illuminates the path

towards high-performance and spectrally selective photodetection, with far-reaching implications for a wide range of fields requiring advanced photodetection capabilities.

## Chapter 7 : Conclusions and Further Works

### 7.1 Conclusions

In the pursuit of advancing the field of nanocomposite materials, this thesis has embarked on a journey of innovation and discovery, exploring the synergistic potential of MOFs in combination with MWCNTs and CNFs. These investigations have yielded remarkable insights and groundbreaking applications across three distinct projects: ZIF-8/MWCNTs-based nanocomposites for methane detection, ZIF-8/MWCNTs-based nanocomposites for diabetes diagnosis via acetone detection, and the utilization of ZIF-8/CNFs as advanced photodetectors.

**First Project:** In our first project, we unveiled a rapid, cost-effective, and efficient method for the preparation of the ZIF-8/MWCNTs nanocomposite. This composite marked a significant advancement, offering an innovative sensing layer for a chemiresistive sensor capable of selectively detecting CH<sub>4</sub> at ambient conditions. The ZIF-8/MWCNTs nanocomposite, characterized by its high surface area, narrow bandgap, rapid carrier mobility, stability, and non-toxic properties, exhibited exceptional sensing performance surpassing that of previously reported materials for CH<sub>4</sub> detection. The introduction of p-type semiconducting behavior to the sensing layer enabled the detection of CH<sub>4</sub> at an astonishingly low concentration of 10 ppb, with a LOD of approximately 0.22 ppb.

Our sensor showcased not only unprecedented sensitivity but also commendable repeatability, stability, reversibility, and high selectivity in the presence of various gases, including CO<sub>2</sub>, CO, NO<sub>2</sub>, NH<sub>3</sub>, alcohols, benzene, and toluene, all at RT and ambient conditions. Moreover, its minimal response to humidity positions it as a promising candidate for real-world applications. We provide the first comprehensive explanation of the sensing mechanism for MOFs/MWCNTs

nanocomposite-based resistive gas sensors, particularly in their selective response to CH<sub>4</sub> over CO<sub>2</sub>, alcohols, and moisture, laying the groundwork for tailored responses to other non-polar gases with low reactivity. This pioneering work signifies the advent of a new class of sensing materials, capable of selectively detecting low-reactivity gases through carrier manipulation within the energy band gap.

**Second Project:** In our second endeavor, we achieved a significant enhancement by addressing the limitation of ZIF-8's low sorption capacity for VOCs at atmospheric pressure and RT. This feat was accomplished by synthesizing a nanocomposite of ZIF-8 and bare MWCNTs. The resulting ZIF-8/MWCNT-coated QCM sensor demonstrated outstanding sorption performance, detecting low concentrations of VOCs, particularly acetone, at 0.62 ppm under atmospheric pressure and RT, surpassing the capabilities of the ZIF-8-coated QCM sensor.

This achievement was attributed to the p-type semiconducting behavior of the ZIF-8/MWCNT composite, which featured a narrower bandgap. We conducted a comparative study between the chemiresistive sensor and the gravimetric QCM sensor based on ZIF-8/MWCNT, shedding light on the effect of different sensing platforms and mechanisms in achieving high selectivity for acetone. The chemiresistive sensor emerged as a standout performer, boasting low response to humidity, high selectivity, good repeatability, complete reversibility, and rapid response times, ultimately achieving a LOD of approximately 1.7 ppb at RT. This LOD significantly outperforms the typical acetone concentration in the exhaled breath of diabetic patients, marking a milestone in the quest for simple, cost-effective, and non-invasive diabetes diagnosis and monitoring.

**Third Project:** Our third project heralded a paradigm shift in photodetection technology by introducing a novel nanocomposite material that harnessed the unique attributes of MOFs and

CNFs. This nanocomposite exhibited exceptional light absorption, photoresponse, charge transport, and charge separation capabilities. Notably, it facilitated precise control over optoelectronic properties and eliminated the need for external optical filters, streamlining the fabrication of spectrally selective photodetectors and reducing manufacturing costs.

Throughout our comprehensive investigation, we demonstrated improved sensitivity, response time, and spectral selectivity of our nanophotodetector under RT and ambient conditions. These findings underscore the transformative potential of 3D MOF nanocomposites in revolutionizing photodetection technology and unlocking new possibilities across diverse technological applications.

In conclusion, these three distinct projects represent significant contributions to the fields of gas sensing, medical diagnostics, and photodetection. They showcase the versatility and promise of MOF-based nanocomposites, opening doors to innovative applications and breakthroughs that have the potential to impact various industries and improve the quality of life for individuals around the world. As we look ahead, the future holds exciting prospects for further exploration and refinement of these pioneering technologies, propelling us towards a new era of scientific and technological advancements.

## **7.2 Future Works**

The culmination of our three distinct projects involving MOF nanocomposites with MWCNTs and CNFs marks significant progress in the fields of gas sensing and advanced photodetectors. However, there remain several avenues for future exploration and development, building upon the foundations we have laid.

**First Project - CH<sub>4</sub> Detection:** While our ZIF-8/MWCNTs nanocomposite has demonstrated remarkable performance in CH<sub>4</sub> detection, there are still opportunities for improvement and diversification. Future work should focus on:

- **Real-World Applications:** Extend the applicability of the sensor to real-world scenarios, such as industrial settings or environmental monitoring, where the detection of low concentrations of CH<sub>4</sub> is crucial.
- **Miniaturization:** Work on further miniaturizing the sensor to make it even more compact and cost-effective, suitable for deployment in portable devices and widespread use.

**Second Project - Acetone Detection for Diabetes Diagnosis:** Our ZIF-8/MWCNT-coated sensors have shown great promise in detecting acetone for diabetes diagnosis. Future research in this area should consider:

- **Clinical Trials:** Conduct clinical trials to validate the effectiveness of our sensors in real healthcare settings. Collaborate with medical professionals and institutions to integrate these sensors into diabetes management protocols.
- **Cross-Sensitivity:** Investigate any potential cross-sensitivity issues in more detail, especially when exposed to a broader range of compounds found in exhaled breath. Develop strategies to further minimize these interferences.
- **Integration:** Work on the integration of these sensors into wearable devices, smartphone apps, or telehealth platforms to enable non-invasive, real-time diabetes monitoring.

**Third Project - Advanced Photodetectors:** Our innovative nanocomposite material combining MOFs and CNFs for advanced photodetectors represents a significant breakthrough. For future endeavors, we should:

- **Material Diversity:** Investigate other MOFs and nanomaterial combinations to expand the range of potential applications and fine-tune optoelectronic properties.
- **Selective Photodetectors:** Explore our selective photodetectors for specific applications, such as medical imaging, optical communication or environmental monitoring.
- **Device Integration:** Collaborate with industry partners to integrate these advanced photodetectors into existing technologies and develop new applications, thereby maximizing their impact.

In conclusion, our research has opened up exciting possibilities in the fields of gas sensing and photodetection through the innovative use of MOF nanocomposites. These future research directions promise to further advance these technologies and bring them closer to practical implementation in various real-world settings, ultimately benefiting society in healthcare, environmental monitoring, and beyond.

## Appendix A: List of publications

1. **S. Homayoonnia**, S. Kim, Eco-friendly and High-Performance Photodetector based on Bandgap-Engineered MOFs/CNFs Nanocomposites for Violet Light Detection, *Advanced Optical Materials*, submitted.
2. **S. Homayoonnia**, S. Kim, ZIF-8/MWCNT-Nanocomposite Based-Resistive Sensor for Highly Selective Detection of Acetone in Parts-Per-Billion: Potential Noninvasive Diagnosis of Diabetes, *Sensors and Actuators B: Chemical*, 393 (2023) 134197.
3. **S. Homayoonnia**, A. Phani, S. Kim, MOF/MWCNTs-Nanocomposite Manipulates High Selectivity to Gas via Different Adsorption-Sites with Varying Electron Affinity: A Study in Methane Detection in Parts-Per-Billion, *ACS sensor*, 7 (2022) 3846-3856.
4. D. Wong, A. Phani, **S. Homayoonnia**, S. Kim, O. Abuzalat, Manipulating Active Sites of 2D Metal Organic Framework Nanosheets with Fluorescent Materials for Enhanced Colorimetric and Fluorescent Ammonia Sensing, *Advanced Materials Interfaces*, 9 (2022) 2102086.
5. **S. Homayoonnia**, Y. Lee, D. Andalib, MS. Rahman, J. Shin, K. Kim, S. Kim, Micro/nanotechnology-inspired rapid diagnosis of respiratory infectious diseases, *Biomedical Engineering Letters*, 11 (2021) 335-365.
6. O. Abuzalat, **S. Homayoonnia**, D. Wong, HR. Tantawy, S. Kim, Facile and rapid synthesis of functionalized Zr-BTC for the optical detection of the blistering agent simulant 2-chloroethyl ethyl sulfide (CEES), *Dalton Trans.*, 50 (2021) 3261-3268.
7. Y. Park, **S. Homayoonnia**, S. Kim, HW. Kim, In-situ fabrication of Cu-BDC on a quartz crystal microbalance for methane sensing at room temperature, *Journal of Inclusion Phenomena and Macrocyclic Chemistry*, 101 (2021) 321-327.

8. A. Huang, O. Abuzalat, **S. Homayoonnia**, D. Wong, N. S. Gunda, S. Kim, S. Mitra, Design of an Arsine Gas Free Rapid Arsenic Detector Using a Novel Luminescent Metal-Organic Framework, ECS Meeting Abstracts, 29, 2201 (2020).

# Appendix B: Reuse Permission Letters

## Permission for Table 2.1

12/4/23, 4:55 PM

Rightslink® by Copyright Clearance Center





**State-of-the-art of methane sensing materials: A review and perspectives**

Author: Tao Hong, Jeffrey T. Culp, Ki-Joong Kim, Jagannath Devkota, Chenhu Sun, Paul R. Ohodnicki  
 Publication: TrAC Trends in Analytical Chemistry  
 Publisher: Elsevier  
 Date: April 2020

© 2020 Elsevier B.V. All rights reserved.

### Order Completed

Thank you for your order.

This Agreement between Miss. Setareh Homayoornia ("You") and Elsevier ("Elsevier") consists of your license details and the terms and conditions provided by Elsevier and Copyright Clearance Center.

Your confirmation email will contain your order number for future reference.

License Number: 5682160725911 [Printable Details](#)

License date: Dec 04, 2023

<h4>Licensed Content</h4> <table border="0"> <tr><td>Licensed Content Publisher</td><td>Elsevier</td></tr> <tr><td>Licensed Content Publication</td><td>TrAC Trends in Analytical Chemistry</td></tr> <tr><td>Licensed Content Title</td><td>State-of-the-art of methane sensing materials: A review and perspectives</td></tr> <tr><td>Licensed Content Author</td><td>Tao Hong, Jeffrey T. Culp, Ki-Joong Kim, Jagannath Devkota, Chenhu Sun, Paul R. Ohodnicki</td></tr> <tr><td>Licensed Content Date</td><td>Apr 1, 2020</td></tr> <tr><td>Licensed Content Volume</td><td>125</td></tr> <tr><td>Licensed Content Issue</td><td>n/a</td></tr> <tr><td>Licensed Content Pages</td><td>1</td></tr> </table> <h4>About Your Work</h4> <table border="0"> <tr><td>Title of new work</td><td>Development of 3D MOF Nanocomposites with Semiconducting Behavior for Resistive Gas Sensors and Photodetectors Applications</td></tr> <tr><td>Institution name</td><td>University Of Calgary</td></tr> <tr><td>Expected presentation date</td><td>Dec 2023</td></tr> </table>	Licensed Content Publisher	Elsevier	Licensed Content Publication	TrAC Trends in Analytical Chemistry	Licensed Content Title	State-of-the-art of methane sensing materials: A review and perspectives	Licensed Content Author	Tao Hong, Jeffrey T. Culp, Ki-Joong Kim, Jagannath Devkota, Chenhu Sun, Paul R. Ohodnicki	Licensed Content Date	Apr 1, 2020	Licensed Content Volume	125	Licensed Content Issue	n/a	Licensed Content Pages	1	Title of new work	Development of 3D MOF Nanocomposites with Semiconducting Behavior for Resistive Gas Sensors and Photodetectors Applications	Institution name	University Of Calgary	Expected presentation date	Dec 2023	<h4>Order Details</h4> <table border="0"> <tr><td>Type of Use</td><td>reuse in a thesis/dissertation</td></tr> <tr><td>Portion</td><td>figures/tables/illustrations</td></tr> <tr><td>Number of figures/tables/illustrations</td><td>1</td></tr> <tr><td>Format</td><td>electronic</td></tr> <tr><td>Are you the author of this Elsevier article?</td><td>No</td></tr> <tr><td>Will you be translating?</td><td>No</td></tr> </table> <h4>Additional Data</h4> <table border="0"> <tr><td>Order reference number</td><td>1</td></tr> <tr><td>Portions</td><td>Table 2</td></tr> </table>	Type of Use	reuse in a thesis/dissertation	Portion	figures/tables/illustrations	Number of figures/tables/illustrations	1	Format	electronic	Are you the author of this Elsevier article?	No	Will you be translating?	No	Order reference number	1	Portions	Table 2
Licensed Content Publisher	Elsevier																																						
Licensed Content Publication	TrAC Trends in Analytical Chemistry																																						
Licensed Content Title	State-of-the-art of methane sensing materials: A review and perspectives																																						
Licensed Content Author	Tao Hong, Jeffrey T. Culp, Ki-Joong Kim, Jagannath Devkota, Chenhu Sun, Paul R. Ohodnicki																																						
Licensed Content Date	Apr 1, 2020																																						
Licensed Content Volume	125																																						
Licensed Content Issue	n/a																																						
Licensed Content Pages	1																																						
Title of new work	Development of 3D MOF Nanocomposites with Semiconducting Behavior for Resistive Gas Sensors and Photodetectors Applications																																						
Institution name	University Of Calgary																																						
Expected presentation date	Dec 2023																																						
Type of Use	reuse in a thesis/dissertation																																						
Portion	figures/tables/illustrations																																						
Number of figures/tables/illustrations	1																																						
Format	electronic																																						
Are you the author of this Elsevier article?	No																																						
Will you be translating?	No																																						
Order reference number	1																																						
Portions	Table 2																																						

12/4/23, 4:55 PM

Rightslink® by Copyright Clearance Center

Requestor Location	Tax Details
Miss. Setareh Homayoonnia 2500 University Drive Northwest	Publisher Tax ID GB 494 6272 12
Requestor Location	Calgary, AB T2N 1N4 Canada Attn: Miss. Setareh Homayoonnia
<b>Total: 0.00 USD</b>	
CLOSE WINDOW	ORDER MORE

© 2023 Copyright - All Rights Reserved | [Copyright Clearance Center, Inc.](#) | [Privacy statement](#) | [Data Security and Privacy](#)  
| [For California Residents](#) | [Terms and Conditions](#) Comments? We would like to hear from you. E-mail us at [customercare@copyright.com](mailto:customercare@copyright.com)

# Permission for Table 2.3

12/4/23, 5:20 PM

Rightslink® by Copyright Clearance Center



## Recent Advances in Low-Dimensional Nanomaterials for Photodetectors

Author: Jaehyun Kim, Junho Lee, Jong-Min Lee, et al

Publication: Small Methods

Publisher: John Wiley and Sons

Date: May 18, 2023

© 2023 Wiley-VCH GmbH

### Order Completed

Thank you for your order.

This Agreement between Miss. Setareh Homayoonnia ("You") and John Wiley and Sons ("John Wiley and Sons") consists of your license details and the terms and conditions provided by John Wiley and Sons and Copyright Clearance Center.

Your confirmation email will contain your order number for future reference.

License Number 5682170723483

[Printable Details](#)

License date Dec 04, 2023

#### Licensed Content

Licensed Content Publisher	John Wiley and Sons
Licensed Content Publication	Small Methods
Licensed Content Title	Recent Advances in Low-Dimensional Nanomaterials for Photodetectors
Licensed Content Author	Jaehyun Kim, Junho Lee, Jong-Min Lee, et al
Licensed Content Date	May 18, 2023
Licensed Content Volume	0
Licensed Content Issue	0
Licensed Content Pages	27

#### Order Details

Type of use	Dissertation/Thesis
Requestor type	University/Academic
Format	Electronic
Portion	Figure/table
Number of figures/tables	1
Will you be translating?	No

#### About Your Work

Title of new work	Development of 3D MOF Nanocomposites with Semiconducting Behavior for Resistive Gas Sensors and Photodetectors Applications
Institution name	University Of Calgary
Expected presentation date	Dec 2023

#### Additional Data

Portions	Table 2.3
----------	-----------

12/4/23, 5:20 PM

Rightslink® by Copyright Clearance Center

Requestor Location	Tax Details
Miss. Setareh Homayoonnia 2500 University Drive Northwest	Publisher Tax ID EU826007151
Requestor Location	Calgary, AB T2N 1N4 Canada Attn: Miss. Setareh Homayoonnia

Would you like to purchase the full text of this article? If so, please continue on to the content ordering system located here: [Purchase PDF](#)  
If you click on the buttons below or close this window, you will not be able to return to the content ordering system.

**Total: 0.00 USD**

CLOSE WINDOW ORDER MORE

© 2023 Copyright - All Rights Reserved | [Copyright Clearance Center, Inc.](#) | [Privacy statement](#) | [Data Security and Privacy](#)  
| [For California Residents](#) | [Terms and Conditions](#) Comments? We would like to hear from you. E-mail us at [customer-care@copyright.com](mailto:customer-care@copyright.com)

## Permission for Figure 2.1



This is a License Agreement between University of Calgary ("User") and Copyright Clearance Center, Inc. ("CCC") on behalf of the Rightsholder identified in the order details below. The license consists of the order details, the Marketplace Permissions General Terms and Conditions below, and any Rightsholder Terms and Conditions which are included below.

All payments must be made in full to CCC in accordance with the Marketplace Permissions General Terms and Conditions below.

Order Date	04-Dec-2023	Type of Use	Republish in a thesis/dissertation
Order License ID	1423340-1	Publisher	ROYAL SOCIETY OF CHEMISTRY, ETC.]
ISSN	0306-0012	Portion	Chart/graph/table/figure

### LICENSED CONTENT

Publication Title	Chemical Society reviews	Rightsholder	Royal Society of Chemistry
Article Title	Functional metal-organic frameworks as effective sensors of gases and volatile compounds.	Publication Type	Journal
Author/Editor	CHEMICAL SOCIETY (GREAT BRITAIN)	Start Page	6364
Date	01/01/1972	End Page	6401
Language	English	Issue	17
Country	United Kingdom of Great Britain and Northern Ireland	Volume	49

### REQUEST DETAILS

Portion Type	Chart/graph/table/figure	Distribution	Canada
Number of Charts / Graphs / Tables / Figures Requested	1	Translation	Original language of publication
Format (select all that apply)	Electronic	Copies for the Disabled?	No
Who Will Republish the Content?	Academic institution	Minor Editing Privileges?	No
Duration of Use	Life of current edition	Incidental Promotional Use?	No
Lifetime Unit Quantity	Up to 499	Currency	CAD
Rights Requested	Main product		

### NEW WORK DETAILS

<b>Title</b>	Development of 3D MOF Nanocomposites with Semiconducting Behavior for Resistive Gas Sensors and Photodetectors Applications	<b>Institution Name</b>	University of Calgary
		<b>Expected Presentation Date</b>	2023-12-07
<b>Instructor Name</b>	Setareh Homayoonnia		

### ADDITIONAL DETAILS

<b>Order Reference Number</b>	N/A	<b>The Requesting Person / Organization to Appear on the License</b>	University of Calgary
-------------------------------	-----	--	-----------------------

### REQUESTED CONTENT DETAILS

<b>Title, Description or Numeric Reference of the Portion(s)</b>	Development of 3D MOF Nanocomposites with Semiconducting Behavior for Resistive Gas Sensors and Photodetectors Applications	<b>Title of the Article / Chapter the Portion Is From</b>	Functional metal-organic frameworks as effective sensors of gases and volatile compounds.
<b>Editor of Portion(s)</b>	Li, Hai-Yang; Zhao, Shu-Na; Zang, Shuang-Quan; Li, Jing	<b>Author of Portion(s)</b>	Li, Hai-Yang; Zhao, Shu-Na; Zang, Shuang-Quan; Li, Jing
<b>Volume / Edition</b>	49	<b>Issue, if Republishing an Article From a Serial</b>	17
<b>Page or Page Range of Portion</b>	6364-6401	<b>Publication Date of Portion</b>	2020-09-06

## Permission for Figure 2.2



This is a License Agreement between University of calgary ("User") and Copyright Clearance Center, Inc. ("CCC") on behalf of the Rightsholder identified in the order details below. The license consists of the order details, the Marketplace Permissions General Terms and Conditions below, and any Rightsholder Terms and Conditions which are included below.

All payments must be made in full to CCC in accordance with the Marketplace Permissions General Terms and Conditions below.

Order Date	04-Dec-2023	Type of Use	Republish in a thesis/dissertation
Order License ID	1423342-1	Publisher	Royal Society of Chemistry
ISSN	2058-9689	Portion	Chart/graph/table/figure

### LICENSED CONTENT

Publication Title	Molecular Systems Design & Engineering	Rightsholder	Royal Society of Chemistry
Article Title	Molecular engineering of perovskite photodetectors: recent advances in materials and devices	Publication Type	e-Journal
Author/Editor	Royal Society of Chemistry (Great Britain),, Institution of Chemical Engineers (Great Britain),	Start Page	702
Date	01/01/2016	End Page	716
Language	English	Issue	5
Country	United Kingdom of Great Britain and Northern Ireland	Volume	3

### REQUEST DETAILS

Portion Type	Chart/graph/table/figure	Distribution	Canada
Number of Charts / Graphs / Tables / Figures Requested	1	Translation	Original language of publication
Format (select all that apply)	Electronic	Copies for the Disabled?	No
Who Will Republish the Content?	Academic institution	Minor Editing Privileges?	No
Duration of Use	Life of current edition	Incidental Promotional Use?	No
Lifetime Unit Quantity	Up to 499	Currency	CAD
Rights Requested	Main product		

### NEW WORK DETAILS

<b>Title</b>	Development of 3D MOF Nanocomposites with Semiconducting Behavior for Resistive Gas Sensors and Photodetectors Applications	<b>Institution Name</b>	university of Calgary
		<b>Expected Presentation Date</b>	2023-12-07
<b>Instructor Name</b>	Setareh Homayoonnia		

### ADDITIONAL DETAILS

<b>Order Reference Number</b>	N/A	<b>The Requesting Person / Organization to Appear on the License</b>	University of calgary
-------------------------------	-----	--	-----------------------

### REQUESTED CONTENT DETAILS

<b>Title, Description or Numeric Reference of the Portion(s)</b>	Development of 3D MOF Nanocomposites with Semiconducting Behavior for Resistive Gas Sensors and Photodetectors Applications	<b>Title of the Article / Chapter the Portion Is From</b>	Molecular engineering of perovskite photodetectors: recent advances in materials and devices
<b>Editor of Portion(s)</b>	Gui, Pengbin; Lin, Qianqian; Yao, Fang; Zhang, Qi	<b>Author of Portion(s)</b>	Gui, Pengbin; Lin, Qianqian; Yao, Fang; Zhang, Qi
<b>Volume / Edition</b>	3	<b>Issue, if Republishing an Article From a Serial</b>	5
<b>Page or Page Range of Portion</b>	702-716	<b>Publication Date of Portion</b>	2017-12-31

## Permission for Figure 2.3

12/4/23, 5:50 PM

Rightslink® by Copyright Clearance Center



**Chapter:**  
11 Luminescence and photodetection characteristics of rare earth-doped zinc oxide nanostructures  
**Book:** Ceramic Science and Engineering  
**Author:** Rajesh Kumar, Sheo K. Mishra  
**Publisher:** Elsevier  
**Date:** 2022

Copyright © 2022 Elsevier Ltd. All rights reserved.

### Order Completed

Thank you for your order.

This Agreement between Miss. Setareh Homayoonnia ("You") and Elsevier ("Elsevier") consists of your license details and the terms and conditions provided by Elsevier and Copyright Clearance Center.

Your confirmation email will contain your order number for future reference.

License Number 5682181020805

[Printable Details](#)

License date Dec 04, 2023

#### Licensed Content

Licensed Content Publisher	Elsevier
Licensed Content Publication	Elsevier Books
Licensed Content Title	Ceramic Science and Engineering
Licensed Content Author	Rajesh Kumar, Sheo K. Mishra
Licensed Content Date	Jan 1, 2022
Licensed Content Pages	32

#### Order Details

Type of Use	reuse in a thesis/dissertation
Portion	figures/tables/illustrations
Number of figures/tables/illustrations	1
Format	electronic
Are you the author of this Elsevier chapter?	No
Will you be translating?	No

#### About Your Work

Title of new work	Development of 3D MOF Nanocomposites with Semiconducting Behavior for Resistive Gas Sensors and Photodetectors Applications
Institution name	University Of Calgary
Expected presentation date	Dec 2023

#### Additional Data

Portions	Figure 2.3
----------	------------

12/4/23, 5:50 PM

Rightslink® by Copyright Clearance Center

Requestor Location	Tax Details
Miss. Setareh Homayoonnia 2500 University Drive Northwest	Publisher Tax ID GB 494 6272 12
Requestor Location	
Calgary, AB T2N 1N4 Canada Attn: Miss. Setareh Homayoonnia	
<b>Total: 0.00 CAD</b>	
CLOSE WINDOW	ORDER MORE

© 2023 Copyright - All Rights Reserved | [Copyright Clearance Center, Inc.](#) | [Privacy statement](#) | [Data Security and Privacy](#)  
| [For California Residents](#) | [Terms and Conditions](#) Comments? We would like to hear from you. E-mail us at [customer@copyright.com](mailto:customer@copyright.com)

## Permission for Chapter 3 and 4

9/20/23, 3:05 PM

Rightslink® by Copyright Clearance Center



### MOF/MWCNT–Nanocomposite Manipulates High Selectivity to Gas via Different Adsorption Sites with Varying Electron Affinity: A Study in Methane Detection in Parts-per-Billion

Author: Setareh Homayoonnia, Arindam Phani, Seonghwan Kim

Publication: ACS Sensors

Publisher: American Chemical Society

Date: Dec 1, 2022

Copyright © 2022, American Chemical Society

#### PERMISSION/LICENSE IS GRANTED FOR YOUR ORDER AT NO CHARGE

This type of permission/license, instead of the standard Terms and Conditions, is sent to you because no fee is being charged for your order. Please note the following:

- Permission is granted for your request in both print and electronic formats, and translations.
- If figures and/or tables were requested, they may be adapted or used in part.
- Please print this page for your records and send a copy of it to your publisher/graduate school.
- Appropriate credit for the requested material should be given as follows: "Reprinted (adapted) with permission from {COMPLETE REFERENCE CITATION}. Copyright {YEAR} American Chemical Society." Insert appropriate information in place of the capitalized words.
- One-time permission is granted only for the use specified in your RightsLink request. No additional uses are granted (such as derivative works or other editions). For any uses, please submit a new request.

If credit is given to another source for the material you requested from RightsLink, permission must be obtained from that source.

[BACK](#)

[CLOSE WINDOW](#)

© 2023 Copyright - All Rights Reserved | [Copyright Clearance Center, Inc.](#) | [Privacy statement](#) | [Data Security and Privacy](#)  
| [For California Residents](#) | [Terms and Conditions](#) Comments? We would like to hear from you. E-mail us at [customercare@copyright.com](mailto:customercare@copyright.com)

## Permission for Chapter 3 and 5

9/20/23, 3:19 PM

Rightslink® by Copyright Clearance Center



- Home
- Help ▾
- Live Chat
- Sign in
- Create Account



### ZIF-8/MWCNT-nanocomposite based-resistive sensor for highly selective detection of acetone in parts-per-billion: Potential noninvasive diagnosis of diabetes

Author: Setareh Homayoonnia, Seonghwan Kim

Publication: Sensors and Actuators B: Chemical

Publisher: Elsevier

Date: 15 October 2023

© 2023 Elsevier B.V. All rights reserved.

#### Journal Author Rights

Please note that, as the author of this Elsevier article, you retain the right to include it in a thesis or dissertation, provided it is not published commercially. Permission is not required, but please ensure that you reference the journal as the original source. For more information on this and on your other retained rights, please visit: <https://www.elsevier.com/about/our-business/policies/copyright#Author-rights>

BACK

CLOSE WINDOW

© 2023 Copyright - All Rights Reserved | [Copyright Clearance Center, Inc.](#) | [Privacy statement](#) | [Data Security and Privacy](#)  
| [For California Residents](#) | [Terms and Conditions](#) Comments? We would like to hear from you. E-mail us at [customercare@copyright.com](mailto:customercare@copyright.com)

## References

- [1] T. Hong, J. T. Culp, K. J. Kim, J. Devkota, C. Sun, and P. R. Ohodnicki, “State-of-the-art of methane sensing materials: A review and perspectives,” *TrAC - Trends Anal. Chem.*, vol. 125, p. 115820, 2020, doi: 10.1016/j.trac.2020.115820.
- [2] A. M. Thompson, K. B. HOGAN, and J. S. HOFFMAN, “SHORT COMMUNICATION METHANE REDUCTIONS : IMPLICATIONS FOR GLOBAL WARMING AND ATMOSPHERIC CHEMICAL CHANGE METHANE CONCENTRATION ( ppbv ) ACTUAL TEMPERATURE INCREASE ( C ° ),” *Atmos. Environ.*, vol. 26, no. 14, pp. 2665–2668, 1992.
- [3] N. S. Lawrence, “Analytical detection methodologies for methane and related hydrocarbons,” *Talanta*, vol. 69, no. 2 SPEC. ISS., pp. 385–392, 2006, doi: 10.1016/j.talanta.2005.10.005.
- [4] “Reducing methane emissions.” <https://www.alberta.ca/climate-methane-emissions.aspx>.
- [5] J. Shemshad, S. M. Aminossadati, and M. S. Kizil, “A review of developments in near infrared methane detection based on tunable diode laser,” *Sensors Actuators, B Chem.*, vol. 171–172, pp. 77–92, 2012, doi: 10.1016/j.snb.2012.06.018.
- [6] M. C. Caumon *et al.*, “Determination of methane content in NaCl-H<sub>2</sub>O fluid inclusions by Raman spectroscopy. Calibration and application to the external part of the Central Alps (Switzerland),” *Chem. Geol.*, vol. 378–379, no. 1, pp. 52–61, 2014, doi: 10.1016/j.chemgeo.2014.03.016.
- [7] H. Nazemi, A. Joseph, J. Park, and A. Emadi, “Advanced micro-and nano-gas sensor technology: A review,” *Sensors (Switzerland)*, vol. 19, no. 6, p. 1285, 2019, doi: 10.3390/s19061285.

- [8] P. Jacquinet, B. Müller, B. Wehrli, and P. C. Hauser, “Determination of methane and other small hydrocarbons with a platinum-Nafion electrode by stripping voltammetry,” *Anal. Chim. Acta*, vol. 432, no. 1, pp. 1–10, 2001, doi: 10.1016/S0003-2670(00)01359-3.
- [9] M. Rahimi, I. Chae, J. E. Hawk, S. K. Mitra, and T. Thundat, “Methane sensing at room temperature using photothermal cantilever deflection spectroscopy,” *Sensors Actuators, B Chem.*, vol. 221, pp. 564–569, 2015, doi: 10.1016/j.snb.2015.07.006.
- [10] M. Eddaoudi *et al.*, “Systematic Design of Pore Size and Functionality in Isoreticular MOFs and Their Application in Methane Storage,” *Science (80-. )*, vol. 295, no. 5554, pp. 469–472, Jan. 2002, doi: 10.1126/science.1067208.
- [11] E. Li, K. Jie, M. Liu, X. Sheng, W. Zhu, and F. Huang, “Vapochromic crystals: Understanding vapochromism from the perspective of crystal engineering,” *Chem. Soc. Rev.*, vol. 49, no. 5, pp. 1517–1544, 2020, doi: 10.1039/c9cs00098d.
- [12] A. Kirchon, L. Feng, H. F. Drake, E. A. Joseph, and H. C. Zhou, “From fundamentals to applications: a toolbox for robust and multifunctional MOF materials,” *Chem. Soc. Rev.*, vol. 47, no. 23, pp. 8611–8638, 2018, doi: 10.1039/c8cs00688a.
- [13] A. M. Rice, C. R. Martin, V. A. Galitskiy, A. A. Berseneva, G. A. Leith, and N. B. Shustova, “Photophysics Modulation in Photoswitchable Metal-Organic Frameworks,” *Chem. Rev.*, vol. 120, no. 16, pp. 8790–8813, 2020, doi: 10.1021/acs.chemrev.9b00350.
- [14] H.-Q. Yin and X.-B. Yin, “Metal–Organic Frameworks with Multiple Luminescence Emissions: Designs and Applications,” *Acc. Chem. Res.*, vol. 53, no. 2, pp. 485–495, Feb. 2020, doi: 10.1021/acs.accounts.9b00575.
- [15] C. Y. Sun *et al.*, “Efficient and tunable white-light emission of metal-organic frameworks by iridium-complex encapsulation,” *Nat. Commun.*, vol. 4, pp. 1–8, 2013, doi:

- 10.1038/ncomms3717.
- [16] M. Pan, W. M. Liao, S. Y. Yin, S. S. Sun, and C. Y. Su, “Single-Phase White-Light-Emitting and Photoluminescent Color-Tuning Coordination Assemblies,” *Chem. Rev.*, vol. 118, no. 18, pp. 8889–8935, 2018, doi: 10.1021/acs.chemrev.8b00222.
- [17] B. Li, H. T. Fan, S. Q. Zang, H. Y. Li, and L. Y. Wang, “Metal-containing crystalline luminescent thermochromic materials,” *Coord. Chem. Rev.*, vol. 377, pp. 307–329, 2018, doi: 10.1016/j.ccr.2018.09.004.
- [18] C. Yang *et al.*, “A semiconducting layered metal-organic framework magnet,” *Nat. Commun.*, vol. 10, no. 1, pp. 1–9, 2019, doi: 10.1038/s41467-019-11267-w.
- [19] A. E. Thorarinsdottir and T. D. Harris, “Metal-Organic Framework Magnets,” *Chem. Rev.*, vol. 120, no. 16, pp. 8716–8789, 2020, doi: 10.1021/acs.chemrev.9b00666.
- [20] G. Mínguez Espallargas and E. Coronado, “Magnetic functionalities in MOFs: From the framework to the pore,” *Chem. Soc. Rev.*, vol. 47, no. 2, pp. 533–557, 2018, doi: 10.1039/c7cs00653e.
- [21] H. F. Wang, L. Chen, H. Pang, S. Kaskel, and Q. Xu, “MOF-derived electrocatalysts for oxygen reduction, oxygen evolution and hydrogen evolution reactions,” *Chem. Soc. Rev.*, vol. 49, no. 5, pp. 1414–1448, 2020, doi: 10.1039/c9cs00906j.
- [22] X. Xiao, L. Zou, H. Pang, and Q. Xu, “Synthesis of micro/nanoscaled metal-organic frameworks and their direct electrochemical applications,” *Chem. Soc. Rev.*, vol. 49, no. 1, pp. 301–331, 2020, doi: 10.1039/c7cs00614d.
- [23] A. Pathak *et al.*, “Integration of a (–Cu–S–) n plane in a metal–organic framework affords high electrical conductivity,” *Nat. Commun.*, vol. 10, no. 1, 2019, doi: 10.1038/s41467-019-09682-0.

- [24] R. Dong *et al.*, “High-mobility band-like charge transport in a semiconducting two-dimensional metal–organic framework,” *Nat. Mater.*, vol. 17, no. 11, pp. 1027–1032, 2018, doi: 10.1038/s41563-018-0189-z.
- [25] A. A. Talin *et al.*, “Tunable electrical conductivity in metal-organic framework thin-film devices,” *Science (80-. )*, vol. 343, no. 6166, pp. 66–69, 2014, doi: 10.1126/science.1246738.
- [26] M. Mon *et al.*, “Postsynthetic Approach for the Rational Design of Chiral Ferroelectric Metal-Organic Frameworks,” *J. Am. Chem. Soc.*, vol. 139, no. 24, pp. 8098–8101, 2017, doi: 10.1021/jacs.7b03633.
- [27] W. Zhang and R. Xiong, “Ferroelectric Metal À Organic Frameworks,” pp. 1163–1195, 2012.
- [28] M. Ding, X. Cai, and H. L. Jiang, “Improving MOF stability: Approaches and applications,” *Chem. Sci.*, vol. 10, no. 44, pp. 10209–10230, 2019, doi: 10.1039/c9sc03916c.
- [29] S. Yuan *et al.*, “Stable Metal–Organic Frameworks: Design, Synthesis, and Applications,” *Adv. Mater.*, vol. 30, no. 37, pp. 1–35, 2018, doi: 10.1002/adma.201704303.
- [30] E. A. Dolgoplova, A. M. Rice, C. R. Martin, and N. B. Shustova, “Photochemistry and photophysics of MOFs: Steps towards MOF-based sensing enhancements,” *Chem. Soc. Rev.*, vol. 47, no. 13, pp. 4710–4728, 2018, doi: 10.1039/c7cs00861a.
- [31] A. Karmakar, P. Samanta, A. V. Desai, and S. K. Ghosh, “Guest-Responsive Metal-Organic Frameworks as Scaffolds for Separation and Sensing Applications,” *Acc. Chem. Res.*, vol. 50, no. 10, pp. 2457–2469, 2017, doi: 10.1021/acs.accounts.7b00151.
- [32] B. Yan, “Lanthanide-Functionalized Metal-Organic Framework Hybrid Systems to Create

- Multiple Luminescent Centers for Chemical Sensing,” *Acc. Chem. Res.*, vol. 50, no. 11, pp. 2789–2798, 2017, doi: 10.1021/acs.accounts.7b00387.
- [33] R. B. Lin, S. Y. Liu, J. W. Ye, X. Y. Li, and J. P. Zhang, “Photoluminescent metal–organic frameworks for gas sensing,” *Adv. Sci.*, vol. 3, no. 7, pp. 1–20, 2016, doi: 10.1002/advs.201500434.
- [34] I. Stassen, N. Burtch, A. Talin, P. Falcaro, M. Allendorf, and R. Ameloot, “An updated roadmap for the integration of metal-organic frameworks with electronic devices and chemical sensors,” *Chem. Soc. Rev.*, vol. 46, no. 11, pp. 3185–3241, 2017, doi: 10.1039/c7cs00122c.
- [35] X. D. Wang and O. S. Wolfbeis, “Optical methods for sensing and imaging oxygen: Materials, spectroscopies and applications,” *Chem. Soc. Rev.*, vol. 43, no. 10, pp. 3666–3761, 2014, doi: 10.1039/c4cs00039k.
- [36] W.-T. Koo, J.-S. Jang, and I.-D. Kim, “Metal-Organic Frameworks for Chemiresistive Sensors,” *Chem*, vol. 5, no. 8, pp. 1938–1963, 2019, doi: 10.1016/j.chempr.2019.04.013.
- [37] W. P. Lustig, S. Mukherjee, N. D. Rudd, A. V. Desai, J. Li, and S. K. Ghosh, “Metal-organic frameworks: Functional luminescent and photonic materials for sensing applications,” *Chem. Soc. Rev.*, vol. 46, no. 11, pp. 3242–3285, 2017, doi: 10.1039/c6cs00930a.
- [38] Z. Hu, B. J. Deibert, and J. Li, “Luminescent metal-organic frameworks for chemical sensing and explosive detection,” *Chem. Soc. Rev.*, vol. 43, no. 16, pp. 5815–5840, 2014, doi: 10.1039/c4cs00010b.
- [39] L. E. Kreno, K. Leong, O. K. Farha, M. Allendorf, R. P. Van Duyne, and J. T. Hupp, “Metal-organic framework materials as chemical sensors,” *Chem. Rev.*, vol. 112, no. 2,

- pp. 1105–1125, 2012, doi: 10.1021/cr200324t.
- [40] B. Chen, L. Wang, F. Zapata, G. Qian, and E. B. Lobkovsky, “A luminescent microporous metal-organic framework for the recognition and sensing of anions,” *J. Am. Chem. Soc.*, vol. 130, no. 21, pp. 6718–6719, 2008, doi: 10.1021/ja802035e.
- [41] N. B. Shustova, A. F. Cozzolino, S. Reineke, M. Baldo, and M. Dincă, “Selective turn-on ammonia sensing enabled by high-temperature fluorescence in metal-organic frameworks with open metal sites,” *J. Am. Chem. Soc.*, vol. 135, no. 36, pp. 13326–13329, 2013, doi: 10.1021/ja407778a.
- [42] M. D. Allendorf *et al.*, “Stress-induced chemical detection using flexible metal-organic frameworks,” *J. Am. Chem. Soc.*, vol. 130, no. 44, pp. 14404–14405, 2008, doi: 10.1021/ja805235k.
- [43] O. Zybaylo *et al.*, “A novel method to measure diffusion coefficients in porous metal-organic frameworks,” *Phys. Chem. Chem. Phys.*, vol. 12, no. 28, pp. 8092–8097, 2010, doi: 10.1039/b927601g.
- [44] R. Ameloot, L. Stappers, J. Fransaer, L. Alaerts, B. F. Sels, and D. E. De Vos, “Patterned growth of metal-organic framework coatings by electrochemical synthesis,” *Chem. Mater.*, vol. 21, no. 13, pp. 2580–2582, 2009, doi: 10.1021/cm900069f.
- [45] E. Biemmi, A. Darga, N. Stock, and T. Bein, “Direct growth of  $\text{Cu}_3(\text{BTC})_2(\text{H}_2\text{O})_3 \cdot x\text{H}_2\text{O}$  thin films on modified QCM-gold electrodes - Water sorption isotherms,” *Microporous Mesoporous Mater.*, vol. 114, no. 1–3, pp. 380–386, 2008, doi: 10.1016/j.micromeso.2008.01.024.
- [46] D. M. D. Alessandro, J. R. R. Kanga, and J. S. Caddy, “Towards Conducting Metal-Organic Frameworks,” *Aust. J. Chem.*, vol. 64, pp. 718–722, 2011, [Online]. Available:

www.publish.csiro.au/journals/ajc.

- [47] L. Sun, M. G. Campbell, and M. Dinca, “Electrically Conductive Porous Metal – Organic Frameworks Angewandte,” *Angew.Chem.Int. Ed.*, vol. 55, pp. 3566–3579, 2016, doi: 10.1002/anie.201506219.
- [48] J. Lei, R. Qian, P. Ling, L. Cui, and H. Ju, “Design and sensing applications of metal-organic framework composites,” *TrAC - Trends Anal. Chem.*, vol. 58, pp. 71–78, 2014, doi: 10.1016/j.trac.2014.02.012.
- [49] Z. Qiao, Z. Wang, C. Zhang, S. Yuan, Y. Zhu, and J. Wang, “PVAm–PIP/PS composite membrane with high performance for CO<sub>2</sub>/N<sub>2</sub> separation,” *AIChE J.*, vol. 59, no. 4, pp. 215–228, 2012, doi: 10.1002/aic.
- [50] K. T. Butler, C. H. Hendon, and A. Walsh, “Electronic chemical potentials of porous metal-organic frameworks,” *J. Am. Chem. Soc.*, vol. 136, no. 7, pp. 2703–2706, 2014, doi: 10.1021/ja4110073.
- [51] S. K. Bhardwaj *et al.*, “An overview of different strategies to introduce conductivity in metal-organic frameworks and miscellaneous applications thereof,” *J. Mater. Chem. A*, vol. 6, no. 31, pp. 14992–15009, 2018, doi: 10.1039/c8ta04220a.
- [52] N. Jafari, S. Zeinali, and J. Shadmehr, “Room temperature resistive gas sensor based on ZIF-8/MWCNT/AgNPs nanocomposite for VOCs detection,” *J. Mater. Sci. Mater. Electron.*, vol. 30, no. 13, pp. 12339–12350, 2019, doi: 10.1007/s10854-019-01592-7.
- [53] N. Jafari and S. Zeinali, “Highly rapid and sensitive formaldehyde detection at room temperature using a zif-8/mwcnt nanocomposite,” *ACS Omega*, vol. 5, no. 9, pp. 4395–4402, 2020, doi: 10.1021/acsomega.9b03124.
- [54] L. Poretsky, *Principles of Diabetes Mellitus*. Boston, MA: Springer US, 2010.

- [55] V. Saasa, T. Malwela, M. Beukes, M. Mokgotho, C. P. Liu, and B. Mwakikunga, “Sensing technologies for detection of acetone in human breath for diabetes diagnosis and monitoring,” *Diagnostics*, vol. 8, no. 1, pp. 1–17, 2018, doi: 10.3390/diagnostics8020012.
- [56] (World Health Organization) WHO, “No Title,” *Global Report on Diabetes*, Available online:, 2023. <http://who.int/diabetes/en/>.
- [57] M. Masikini, M. Chowdhury, and O. Nemraoui, “Review—Metal Oxides: Application in Exhaled Breath Acetone Chemiresistive Sensors,” *J. Electrochem. Soc.*, vol. 167, no. 3, p. 037537, 2020, doi: 10.1149/1945-7111/ab64bc.
- [58] J. King *et al.*, “Measurement of endogenous acetone and isoprene in exhaled breath during sleep,” *Physiol. Meas.*, vol. 33, no. 3, pp. 413–428, 2012, doi: 10.1088/0967-3334/33/3/413.
- [59] A. Amann *et al.*, “The human volatilome: Volatile organic compounds (VOCs) in exhaled breath, skin emanations, urine, feces and saliva,” *J. Breath Res.*, vol. 8, no. 3, 2014, doi: 10.1088/1752-7155/8/3/034001.
- [60] J. King *et al.*, “Dynamic profiles of volatile organic compounds in exhaled breath as determined by a coupled PTR-MS/GC-MS study,” *Physiol. Meas.*, vol. 31, no. 9, pp. 1169–1184, 2010, doi: 10.1088/0967-3334/31/9/008.
- [61] C. Deng, J. Zhang, X. Yu, W. Zhang, and X. Zhang, “Determination of acetone in human breath by gas chromatography–mass spectrometry and solid-phase microextraction with on-fiber derivatization,” *J. Chromatogr. B*, vol. 810, no. 2, pp. 269–275, 2004, doi: 10.1016/j.jchromb.2004.08.013.
- [62] T. Ligor *et al.*, “The analysis of healthy volunteers’ exhaled breath by the use of solid-phase microextraction and GC-MS,” *J. Breath Res.*, vol. 2, no. 4, p. 046006, Dec. 2008,

doi: 10.1088/1752-7155/2/4/046006.

- [63] I.-D. Kim, S.-J. Choi, S.-J. Kim, and J.-S. Jang, *Smart Sensors for Health and Environment Monitoring*. Dordrecht: Springer Netherlands, 2015.
- [64] S. J. Young and Z. D. Lin, “Acetone gas sensors composed of carbon nanotubes with adsorbed Au nanoparticles on plastic substrate,” *Microsyst. Technol.*, vol. 24, no. 10, pp. 3973–3976, 2018, doi: 10.1007/s00542-017-3562-y.
- [65] J. C. Chiou, C. C. Wu, and T. M. Lin, “Sensitivity enhancement of acetone gas sensor using polyethylene glycol/multi-walled carbon nanotubes composite sensing film with thermal treatment,” *Polymers (Basel)*, vol. 11, no. 3, 2019, doi: 10.3390/polym11030423.
- [66] S. J. Choi, C. Choi, S. J. Kim, H. J. Cho, S. Jeon, and I. D. Kim, “Facile synthesis of hierarchical porous WO<sub>3</sub> nanofibers having 1D nanoneedles and their functionalization with non-oxidized graphene flakes for selective detection of acetone molecules,” *RSC Adv.*, vol. 5, no. 10, pp. 7584–7588, 2015, doi: 10.1039/c4ra13791d.
- [67] A. Rydosz, “Sensors for enhanced detection of acetone as a potential tool for noninvasive diabetes monitoring,” *Sensors (Switzerland)*, vol. 18, no. 7, pp. 1–14, 2018, doi: 10.3390/s18072298.
- [68] S. Homayoonnia and S. Zeinali, “Design and fabrication of capacitive nanosensor based on MOF nanoparticles as sensing layer for VOCs detection,” *Sensors Actuators, B Chem.*, vol. 237, pp. 776–786, 2016, doi: 10.1016/j.snb.2016.06.152.
- [69] S. Zeinali, S. Homayoonnia, and G. Homayoonnia, “Comparative investigation of interdigitated and parallel-plate capacitive gas sensors based on Cu-BTC nanoparticles for selective detection of polar and apolar VOCs indoors,” *Sensors Actuators, B Chem.*, vol. 278, no. June 2018, pp. 153–164, 2019, doi: 10.1016/j.snb.2018.07.006.

- [70] J. Kim, J. Lee, J. M. Lee, A. Facchetti, T. J. Marks, and S. K. Park, “Recent Advances in Low-Dimensional Nanomaterials for Photodetectors,” *Small Methods*, vol. 2300246, pp. 1–27, 2023, doi: 10.1002/smtd.202300246.
- [71] S. Huang *et al.*, “Black Silicon Photodetector with Excellent Comprehensive Properties by Rapid Thermal Annealing and Hydrogenated Surface Passivation,” *Adv. Opt. Mater.*, vol. 8, no. 7, pp. 1–7, 2020, doi: 10.1002/adom.201901808.
- [72] S. Yanikgonul *et al.*, “Integrated avalanche photodetectors for visible light,” *Nat. Commun.*, vol. 12, no. 1, pp. 1–8, 2021, doi: 10.1038/s41467-021-22046-x.
- [73] W. Yang, J. Chen, Y. Zhang, Y. Zhang, J. H. He, and X. Fang, “Silicon-Compatible Photodetectors: Trends to Monolithically Integrate Photosensors with Chip Technology,” *Adv. Funct. Mater.*, vol. 29, no. 18, 2019, doi: 10.1002/adfm.201808182.
- [74] H. Ren, J. De Chen, Y. Q. Li, and J. X. Tang, “Recent Progress in Organic Photodetectors and their Applications,” *Adv. Sci.*, vol. 8, no. 1, pp. 1–23, 2021, doi: 10.1002/advs.202002418.
- [75] N. S. Rohizat, A. H. A. Ripain, C. S. Lim, C. L. Tan, and R. Zakaria, “Plasmon-enhanced reduced graphene oxide photodetector with monometallic of Au and Ag nanoparticles at VIS–NIR region,” *Sci. Rep.*, vol. 11, no. 1, pp. 1–10, 2021, doi: 10.1038/s41598-021-99189-w.
- [76] Q. Gao *et al.*, “CuO Nanosheets for Use in Photoelectrochemical Photodetectors,” *ACS Appl. Nano Mater.*, vol. 6, no. 1, pp. 784–791, 2023, doi: 10.1021/acsanm.2c05270.
- [77] H. Wang *et al.*, “Self-Powered Sb<sub>2</sub>Te<sub>3</sub>/MoS<sub>2</sub> Heterojunction Broadband Photodetector on Flexible Substrate from Visible to Near Infrared,” *Nanomaterials*, vol. 13, no. 13, p. 1973, 2023, doi: 10.3390/nano13131973.

- [78] F. H. L. Koppens, T. Mueller, P. Avouris, A. C. Ferrari, M. S. Vitiello, and M. Polini, “Photodetectors based on graphene, other two-dimensional materials and hybrid systems,” *Nat. Nanotechnol.*, vol. 9, no. 10, pp. 780–793, 2014, doi: 10.1038/nnano.2014.215.
- [79] A. Zubair *et al.*, “Carbon nanotube woven textile photodetector,” *Phys. Rev. Mater.*, vol. 2, no. 1, 2018, doi: 10.1103/PhysRevMaterials.2.015201.
- [80] D. Shao, L. Qin, and S. Sawyer, “Near ultraviolet photodetector fabricated from polyvinyl-alcohol coated In<sub>2</sub>O<sub>3</sub> nanoparticles,” *Appl. Surf. Sci.*, vol. 261, pp. 123–127, 2012, doi: 10.1016/j.apsusc.2012.07.111.
- [81] S. H. Cheng, T. M. Weng, M. L. Lu, W. C. Tan, J. Y. Chen, and Y. F. Chen, “All carbon-based photodetectors: An eminent integration of graphite quantum dots and two dimensional graphene,” *Sci. Rep.*, vol. 3, pp. 1–7, 2013, doi: 10.1038/srep02694.
- [82] W. Wu *et al.*, “Ultrafast Carbon Nanotube Photodetectors with Bandwidth over 60 GHz,” *ACS Photonics*, 2022, doi: 10.1021/acsp Photonics.2c01626.
- [83] S. P. Chang and K. J. Chen, “Zinc oxide nanoparticle photodetector,” *J. Nanomater.*, vol. 2012, pp. 1–6, 2012, doi: 10.1155/2012/602398.
- [84] M. Scagliotti *et al.*, “Carbon nanotube film/silicon heterojunction photodetector for new cutting-edge technological devices,” *Appl. Sci.*, vol. 11, no. 2, pp. 1–15, 2021, doi: 10.3390/app11020606.
- [85] J. J. Wang, J. S. Hu, Y. G. Guo, and L. J. Wan, “Eco-friendly visible-wavelength photodetectors based on bandgap engineerable nanomaterials,” *J. Mater. Chem.*, vol. 21, no. 44, pp. 17582–17589, 2011, doi: 10.1039/c1jm12173a.
- [86] D. D. Wang *et al.*, “A sensitive red light nano-photodetector propelled by plasmonic copper nanoparticles,” *J. Mater. Chem. C*, vol. 5, no. 6, pp. 1328–1335, 2017, doi:

10.1039/c6tc05117k.

- [87] M. Spina *et al.*, “Microengineered CH<sub>3</sub>NH<sub>3</sub>PbI<sub>3</sub> Nanowire/Graphene Phototransistor for Low-Intensity Light Detection at Room Temperature,” *Small*, vol. 11, no. 37, pp. 4824–4828, 2015, doi: 10.1002/sml.201501257.
- [88] S. Cai, X. Xu, W. Yang, J. Chen, and X. Fang, “Materials and Designs for Wearable Photodetectors,” *Adv. Mater.*, vol. 31, no. 18, pp. 1–15, 2019, doi: 10.1002/adma.201808138.
- [89] S. Yu, C. Liu, and S. Han, “A New Strategy to Fabricate Nanoporous Gold and Its Application in Photodetector,” *Nanomaterials*, vol. 12, no. 9, pp. 1–10, 2022, doi: 10.3390/nano12091580.
- [90] Z. M. Wei and J. B. Xia, “Recent progress in polarization-sensitive photodetectors based on low-dimensional semiconductors,” *Wuli Xuebao/Acta Phys. Sin.*, vol. 68, no. 16, pp. 393–411, 2019, doi: 10.7498/aps.68.20191002.
- [91] C. Li, J. Li, Z. Li, H. Zhang, Y. Dang, and F. Kong, “High-performance photodetectors based on nanostructured perovskites,” *Nanomaterials*, vol. 11, no. 4, 2021, doi: 10.3390/nano11041038.
- [92] O. Abuzalat, S. Homayoonnia, D. Wong, H. R. Tantawy, and S. Kim, “Facile and rapid synthesis of functionalized Zr-BTC for the optical detection of the blistering agent simulant 2-chloroethyl ethyl sulfide (CEES),” *Dalt. Trans.*, vol. 50, no. 9, pp. 3261–3268, 2021, doi: 10.1039/d0dt04382f.
- [93] S. Homayoonnia, A. Phani, and S. Kim, “MOF/MWCNT-Nanocomposite Manipulates High Selectivity to Gas via Different Adsorption Sites with Varying Electron Affinity: A Study in Methane Detection in Parts-per-Billion,” *ACS Sensors*, vol. 7, no. 12, pp. 3846–

- 3856, 2022, doi: 10.1021/acssensors.2c01796.
- [94] M. H. Tran and J. Hur, “Ultra-high Stability of Wearable Photodetector Using Zirconium Metal-Organic Framework Enabling In Situ and Continuous Monitoring of Ultraviolet Radiation Risk,” *Adv. Opt. Mater.*, vol. 10, no. 1, pp. 1–14, 2022, doi: 10.1002/adom.202101404.
- [95] S. Homayoonnia and S. Kim, “ZIF-8/MWCNT-Nanocomposite Based-Resistive Sensor for Highly Selective Detection of Acetone in Parts-Per-Billion: Potential Noninvasive Diagnosis of Diabetes,” *Sensors Actuators B Chem.*, vol. 393, no. June, p. 134197, 2023, doi: 10.1016/j.snb.2023.134197.
- [96] D. Wong, A. Phani, S. Homayoonnia, S. S. Park, S. Kim, and O. Abuzalat, “Manipulating Active Sites of 2D Metal–Organic Framework Nanosheets with Fluorescent Materials for Enhanced Colorimetric and Fluorescent Ammonia Sensing,” *Adv. Mater. Interfaces*, vol. 9, no. 6, p. 2102086, 2022, doi: 10.1002/admi.202102086.
- [97] A. Huang *et al.*, “Design of an Arsine Gas Free Rapid Arsenic Detector Using a Novel Luminescent Metal-Organic Framework,” *ECS Meet. Abstr.*, vol. MA2020-01, no. 29, pp. 2201–2201, May 2020, doi: 10.1149/MA2020-01292201mtgabs.
- [98] Y. Park, S. Homayoonnia, S. Kim, and H. Woo, “In - situ fabrication of Cu - BDC on a quartz crystal microbalance for methane sensing at room temperature,” *J. Incl. Phenom. Macrocycl. Chem.*, vol. 101, no. 3, pp. 321–327, 2021, doi: 10.1007/s10847-021-01056-8.
- [99] F. Wang *et al.*, “High-sensitivity shortwave infrared photodetectors of metal-organic frameworks integrated on 2D layered materials,” *Sci. China Mater.*, vol. 65, no. 2, pp. 451–459, 2022, doi: 10.1007/s40843-021-1781-y.
- [100] H. Arora *et al.*, “Demonstration of a Broadband Photodetector Based on a Two-

- Dimensional Metal–Organic Framework,” *Adv. Mater.*, vol. 32, no. 9, 2020, doi: 10.1002/adma.201907063.
- [101] X. Shang *et al.*, “Micro-/nano-sized multifunctional heterochiral metal-organic frameworks for high-performance visible-blind UV photodetectors,” *J. Mater. Chem. C*, vol. 9, no. 23, pp. 7310–7318, 2021, doi: 10.1039/d1tc01333e.
- [102] S. Bachinin, A. Marunchenko, N. Zhestkij, E. Gunina, and V. A. Milichko, “Metal-organic framework single crystal infrared photodetector,” *Photonics Nanostructures - Fundam. Appl.*, vol. 55, no. April, p. 101145, 2023, doi: 10.1016/j.photonics.2023.101145.
- [103] T. M. H. Nguyen and C. W. Bark, “Self-Powered UVC Photodetector Based on Europium Metal-Organic Framework for Facile Monitoring Invisible Fire,” *ACS Appl. Mater. Interfaces*, vol. 14, no. 40, pp. 45573–45581, 2022, doi: 10.1021/acsami.2c13231.
- [104] G. Korotcenkov, “Gas response control through structural and chemical modification of metal oxide films: State of the art and approaches,” *Sensors Actuators, B Chem.*, vol. 107, no. 1 SPEC. ISS., pp. 209–232, 2005, doi: 10.1016/j.snb.2004.10.006.
- [105] G. Korotcenkov, “The role of morphology and crystallographic structure of metal oxides in response of conductometric-type gas sensors,” *Mater. Sci. Eng. R Reports*, vol. 61, no. 1–6, pp. 1–39, 2008, doi: 10.1016/j.mser.2008.02.001.
- [106] A. Tischner, A. Köck, T. Maier, C. Edtmaier, C. Gspan, and G. Kothleitner, “Tin oxide nanocrystalline films and nanowires for gas sensing applications,” *Microelectron. Eng.*, vol. 86, no. 4–6, pp. 1258–1261, 2009, doi: 10.1016/j.mee.2008.11.084.
- [107] R. Ionescu, A. Vancu, C. Moise, and A. Tomescu, “Role of water vapour in the interaction of SnO<sub>2</sub> gas sensors with CO and CH<sub>4</sub>,” *Sensors Actuators, B Chem.*, vol. 61, no. 1, pp.

- 39–42, 1999, doi: 10.1016/S0925-4005(99)00277-4.
- [108] P. Bhattacharyya, P. K. Basu, C. Lang, H. Saha, and S. Basu, “Noble metal catalytic contacts to sol-gel nanocrystalline zinc oxide thin films for sensing methane,” *Sensors Actuators, B Chem.*, vol. 129, no. 2, pp. 551–557, 2008, doi: 10.1016/j.snb.2007.09.001.
- [109] P. Bhattacharyya, P. K. Basu, H. Saha, and S. Basu, “Fast response methane sensor using nanocrystalline zinc oxide thin films derived by sol-gel method,” *Sensors Actuators, B Chem.*, vol. 124, no. 1, pp. 62–67, 2007, doi: 10.1016/j.snb.2006.11.046.
- [110] A. K. Prasad, S. Amirthapandian, S. Dhara, S. Dash, N. Murali, and A. K. Tyagi, “Novel single phase vanadium dioxide nanostructured films for methane sensing near room temperature,” *Sensors Actuators, B Chem.*, vol. 191, pp. 252–256, 2014, doi: 10.1016/j.snb.2013.09.102.
- [111] W. Li, J. Liang, J. Liu, L. Zhou, R. Yang, and M. Hu, “Synthesis and room temperature CH<sub>4</sub> gas sensing properties of vanadium dioxide nanorods,” *Mater. Lett.*, vol. 173, pp. 199–202, 2016, doi: 10.1016/j.matlet.2016.03.035.
- [112] G. K. Flingelli, M. M. Fleischer, and H. Meixner, “Selective detection of methane in domestic environments using a catalyst sensor system based on Ga<sub>2</sub>O<sub>3</sub>,” *Sensors Actuators, B Chem.*, vol. 48, no. 1–3, pp. 258–262, 1998, doi: 10.1016/S0925-4005(98)00054-9.
- [113] S. Barazzouk, R. P. Tandon, and S. Hotchandani, “MoO<sub>3</sub>-based sensor for NO, NO<sub>2</sub> and CH<sub>4</sub> detection,” *Sensors Actuators, B Chem.*, vol. 119, no. 2, pp. 691–694, 2006, doi: 10.1016/j.snb.2006.01.026.
- [114] N. M. Shaalan, M. Rashad, A. H. Moharram, and M. A. Abdel-Rahim, “Promising methane gas sensor synthesized by microwave-assisted Co<sub>3</sub>O<sub>4</sub> nanoparticles,” *Mater. Sci.*

- Semicond. Process.*, vol. 46, pp. 1–5, 2016, doi: 10.1016/j.mssp.2016.01.020.
- [115] Y. Zhou, Y. Fang, and R. P. Ramasamy, “Non-covalent functionalization of carbon nanotubes for electrochemical biosensor development,” *Sensors (Switzerland)*, vol. 19, no. 2, 2019, doi: 10.3390/s19020392.
- [116] P. Bondavalli, P. Legagneux, and D. Pribat, “Carbon nanotubes based transistors as gas sensors: State of the art and critical review,” *Sensors Actuators, B Chem.*, vol. 140, no. 1, pp. 304–318, 2009, doi: 10.1016/j.snb.2009.04.025.
- [117] Z. Xiao *et al.*, “Recent development in nanocarbon materials for gas sensor applications,” *Sensors Actuators, B Chem.*, vol. 274, no. July, pp. 235–267, 2018, doi: 10.1016/j.snb.2018.07.040.
- [118] S. S. Varghese, S. Lonkar, K. K. Singh, S. Swaminathan, and A. Abdala, “Recent advances in graphene based gas sensors,” *Sensors Actuators, B Chem.*, vol. 218, pp. 160–183, 2015, doi: 10.1016/j.snb.2015.04.062.
- [119] K. Toda, R. Furue, and S. Hayami, “Recent progress in applications of graphene oxide for gas sensing: A review,” *Anal. Chim. Acta*, vol. 878, pp. 43–53, 2015, doi: 10.1016/j.aca.2015.02.002.
- [120] B. Mayers, B. Gates, Y. Yin, and Y. Xia, “Functionalized carbon nanotubes for molecular hydrogen sensors,” *Adv. Mater.*, vol. 13, no. 18, pp. 1384–1386, 2001, doi: 10.1002/1521-4095(200109)13:18<1384::AID-ADMA1384>3.0.CO;2-8.
- [121] A. Goldoni, V. Alijani, L. Sangaletti, and L. D’Arsiè, “Advanced promising routes of carbon/metal oxides hybrids in sensors: A review,” *Electrochim. Acta*, vol. 266, pp. 139–150, 2018, doi: 10.1016/j.electacta.2018.01.170.
- [122] L. C. Wang *et al.*, “A single-walled carbon nanotube network gas sensing device,”

- Sensors*, vol. 11, no. 8, pp. 7763–7772, 2011, doi: 10.3390/s110807763.
- [123] Q. Zhao, M. B. Nardelli, W. Lu, and J. Bernholc, “Carbon nanotube-metal cluster composites: A new road to chemical sensors?,” *Nano Lett.*, vol. 5, no. 5, pp. 847–851, 2005, doi: 10.1021/nl050167w.
- [124] J. Zhao, A. Buldum, J. Han, and J. P. Lu, “Gas molecule adsorption in carbon nanotubes and nanotube bundles,” *Nanotechnology*, vol. 13, no. 2, pp. 195–200, 2002, doi: 10.1088/0957-4484/13/2/312.
- [125] M. Singh, S. K. Raghuvanshi, and O. Prakash, “Ultra-Sensitive Fiber Optic Gas Sensor Using Graphene Oxide Coated Long Period Gratings,” *IEEE Photonics Technol. Lett.*, vol. 31, no. 17, pp. 1473–1476, 2019, doi: 10.1109/LPT.2019.2932764.
- [126] R. Afrin and N. A. Shah, “Room temperature gas sensors based on carboxyl and thiol functionalized carbon nanotubes buckypapers,” *Diam. Relat. Mater.*, vol. 60, pp. 42–49, 2015, doi: 10.1016/j.diamond.2015.10.010.
- [127] Z. P. Li, Y. Guo, S. Z. Wu, S. M. Shuang, and C. Dong, “Methane sensor based on palladium/MWNT nanocomposites,” *Chinese Chem. Lett.*, vol. 20, no. 5, pp. 608–610, 2009, doi: 10.1016/j.ccllet.2008.12.031.
- [128] Z. Li, J. Li, X. Wu, S. Shuang, C. Dong, and M. M. F. Choi, “Methane sensor based on nanocomposite of palladium/multi-walled carbon nanotubes grafted with 1,6-hexanediamine,” *Sensors Actuators, B Chem.*, vol. 139, no. 2, pp. 453–459, 2009, doi: 10.1016/j.snb.2009.03.069.
- [129] K. C. Lam, B. Huang, and S. Q. Shi, “Room-temperature methane gas sensing properties based on in situ reduced graphene oxide incorporated with tin dioxide,” *J. Mater. Chem. A*, vol. 5, no. 22, pp. 11131–11142, 2017, doi: 10.1039/c7ta01293d.

- [130] S. Nasresfahani, M. H. Sheikhi, M. Tohidi, and A. Zarifkar, "Methane gas sensing properties of Pd-doped SnO<sub>2</sub>/reduced graphene oxide synthesized by a facile hydrothermal route," *Mater. Res. Bull.*, vol. 89, pp. 161–169, 2017, doi: 10.1016/j.materresbull.2017.01.032.
- [131] S. B. Naghadeh, S. Vahdatifar, Y. Mortazavi, A. A. Khodadadi, and A. Abbasi, "Functionalized MWCNTs effects on dramatic enhancement of MWCNTs/SnO<sub>2</sub> nanocomposite gas sensing properties at low temperatures," *Sensors Actuators, B Chem.*, vol. 223, pp. 252–260, 2016, doi: 10.1016/j.snb.2015.09.088.
- [132] Z. Wu *et al.*, "on Graphene Nanosheets / Polyaniline Nanocomposite Thin Film," vol. 13, no. 2, pp. 777–782, 2013.
- [133] S. K. Mishra, S. N. Tripathi, V. Choudhary, and B. D. Gupta, "Surface Plasmon Resonance-Based Fiber Optic Methane Gas Sensor Utilizing Graphene-Carbon Nanotubes-Poly(Methyl Methacrylate) Hybrid Nanocomposite," *Plasmonics*, vol. 10, no. 5, pp. 1147–1157, 2015, doi: 10.1007/s11468-015-9914-5.
- [134] H. Bai and G. Shi, "Gas sensors based on conducting polymers," *Sensors*, vol. 7, no. 3, pp. 267–307, 2007, doi: 10.3390/s7030267.
- [135] G. Xie, P. Sun, X. Yan, X. Du, and Y. Jiang, "Fabrication of methane gas sensor by layer-by-layer self-assembly of polyaniline/PdO ultra thin films on quartz crystal microbalance," *Sensors Actuators, B Chem.*, vol. 145, no. 1, pp. 373–377, 2010, doi: 10.1016/j.snb.2009.12.035.
- [136] S. Sattari, A. Reyhani, M. R. Khanlari, M. Khabazian, and H. Heydari, "Synthesize of polyaniline-multi walled carbon nanotubes composite on the glass and silicon substrates and methane gas sensing behavior of them at room temperature," *J. Ind. Eng. Chem.*, vol.

- 20, no. 4, pp. 1761–1764, 2014, doi: 10.1016/j.jiec.2013.08.029.
- [137] O. Abuzalat, D. Wong, S. S. Park, and S. Kim, “High-Performance, Room Temperature Hydrogen Sensing with a Cu-BTC/Polyaniline Nanocomposite Film on a Quartz Crystal Microbalance,” *IEEE Sens. J.*, vol. 19, no. 13, pp. 4789–4795, 2019, doi: 10.1109/JSEN.2019.2904870.
- [138] T. Sen, S. Mishra, S. S. Sonawane, and N. G. Shimpi, “Polyaniline/zinc oxide nanocomposite as room-temperature sensing layer for methane,” *Polym. Eng. Sci.*, vol. 58, no. 8, pp. 1438–1445, 2018, doi: 10.1002/pen.24740.
- [139] H. Y. Li, S. N. Zhao, S. Q. Zang, and J. Li, “Functional metal-organic frameworks as effective sensors of gases and volatile compounds,” *Chem. Soc. Rev.*, vol. 49, no. 17, pp. 6364–6401, 2020, doi: 10.1039/c9cs00778d.
- [140] J. A. Gustafson and C. E. Wilmer, “Optimizing information content in MOF sensor arrays for analyzing methane-air mixtures,” *Sensors Actuators, B Chem.*, vol. 267, pp. 483–493, 2018, doi: 10.1016/j.snb.2018.04.049.
- [141] J. A. Gustafson and C. E. Wilmer, “Intelligent Selection of Metal-Organic Framework Arrays for Methane Sensing via Genetic Algorithms,” *ACS Sensors*, vol. 4, no. 6, pp. 1586–1593, 2019, doi: 10.1021/acssensors.9b00268.
- [142] J. A. Gustafson and C. E. Wilmer, “Computational Design of Metal–Organic Framework Arrays for Gas Sensing: Influence of Array Size and Composition on Sensor Performance,” *J. Phys. Chem. C*, vol. 121, no. 11, pp. 6033–6038, 2017, doi: 10.1021/acs.jpcc.6b09740.
- [143] J. C. Cardenas, L. A. Castillo, W. Molano, C. A. Sierra, and A. Reiber, “Fluorescent post-synthetic modified MOFs for methane sensing,” *Adv. Mater. - TechConnect Briefs 2016*,

- vol. 2, pp. 88–91, 2016.
- [144] J. Devkota, K. J. Kim, P. R. Ohodnicki, J. T. Culp, D. W. Greve, and J. W. Lekse, “Zeolitic imidazolate framework-coated acoustic sensors for room temperature detection of carbon dioxide and methane,” *Nanoscale*, vol. 10, no. 17, pp. 8075–8087, 2018, doi: 10.1039/c7nr09536h.
- [145] R. Cao *et al.*, “Fiber optical sensor for methane detection based on metal-organic framework/silicone polymer coating,” in *Conference on Lasers and Electro-Optics (CLEO)*, 2018, pp. 1–2, [Online]. Available: <https://ieeexplore.ieee.org/document/8427422>.
- [146] T. Xiao *et al.*, “Highly sensitive and selective acetone sensor based on C-doped WO<sub>3</sub> for potential diagnosis of diabetes mellitus Dedicated to Prof. Xinquan Xin on the occasion of his 80th birthday.” *Sensors Actuators, B Chem.*, vol. 199, pp. 210–219, 2014, doi: 10.1016/j.snb.2014.04.015.
- [147] B. Çakıroğlu and M. Özacar, “Photoelectrochemical and Non-Enzymatic Glucose Sensor Based on Modified Fehling’s Test by Using Ti/TiO<sub>2</sub> NTs-rGO-Cu<sub>2</sub>O Electrode,” *J. Electrochem. Soc.*, vol. 166, no. 8, pp. B728–B734, 2019, doi: 10.1149/2.1201908jes.
- [148] S. J. Park, C. S. Park, and H. Yoon, “Chemo-electrical gas sensors based on conducting polymer hybrids,” *Polymers (Basel)*, vol. 9, no. 5, 2017, doi: 10.3390/polym9050155.
- [149] F. Usman, J. O. Dennis, A. Y. Ahmed, F. Meriaudeau, O. B. Ayodele, and A. A. S. Rabih, “A Review of Biosensors for Non-Invasive Diabetes Monitoring and Screening in Human Exhaled Breath,” *IEEE Access*, vol. 7, pp. 5963–5974, 2019, doi: 10.1109/ACCESS.2018.2887066.
- [150] E. Aparicio-Martínez, V. Osuna, R. B. Dominguez, A. Márquez-Lucero, E. A. Zaragoza-

- Contreras, and A. Vega-Rios, "Room Temperature Detection of Acetone by a PANI/Cellulose/WO<sub>3</sub> Electrochemical Sensor," *J. Nanomater.*, vol. 2018, 2018, doi: 10.1155/2018/6519694.
- [151] D. Jariwala, V. K. Sangwan, L. J. Lauhon, T. J. Marks, and M. C. Hersam, "Carbon nanomaterials for electronics, optoelectronics, photovoltaics, and sensing," *Chem. Soc. Rev.*, vol. 42, no. 7, pp. 2824–2860, 2013, doi: 10.1039/c2cs35335k.
- [152] Y. Zhang *et al.*, "Electron-Transport Layers Employing Strongly Bound Ligands Enhance Stability in Colloidal Quantum Dot Infrared Photodetectors," *Adv. Mater.*, vol. 34, no. 47, pp. 1–8, 2022, doi: 10.1002/adma.202206884.
- [153] R. Guo, M. Zhang, J. Ding, A. Liu, F. Huang, and M. Sheng, "Advances in colloidal quantum dot-based photodetectors," *J. Mater. Chem. C*, vol. 10, no. 19, pp. 7404–7422, 2022, doi: 10.1039/d2tc00219a.
- [154] X. Wei *et al.*, "Recent Advances in Structure Separation of Single-Wall Carbon Nanotubes and Their Application in Optics, Electronics, and Optoelectronics," *Adv. Sci.*, vol. 9, no. 14, pp. 1–42, 2022, doi: 10.1002/advs.202200054.
- [155] M. Zhao *et al.*, "Advances in Two-Dimensional Materials for Optoelectronics Applications," *Crystals*, vol. 12, no. 8, 2022, doi: 10.3390/cryst12081087.
- [156] C. Gong *et al.*, "2D Nanomaterial Arrays for Electronics and Optoelectronics," *Adv. Funct. Mater.*, vol. 28, no. 16, 2018, doi: 10.1002/adfm.201706559.
- [157] S. Sagadevan *et al.*, "Functionalized graphene-based nanocomposites for smart optoelectronic applications," *Nanotechnol. Rev.*, vol. 10, no. 1, pp. 605–635, 2021, doi: 10.1515/ntrev-2021-0043.
- [158] F. Zhang *et al.*, "Recent advances on graphene: Synthesis, properties and applications,"

- Compos. Part A Appl. Sci. Manuf.*, vol. 160, no. April, p. 107051, 2022, doi:  
10.1016/j.compositesa.2022.107051.
- [159] Z. Hu *et al.*, “Doping of Graphene Films: Open the way to Applications in Electronics and Optoelectronics,” *Adv. Funct. Mater.*, vol. 32, no. 42, 2022, doi:  
10.1002/adfm.202203179.
- [160] Q. H. Wang, K. Kalantar-Zadeh, A. Kis, J. N. Coleman, and M. S. Strano, “Electronics and optoelectronics of two-dimensional transition metal dichalcogenides,” *Nat. Nanotechnol.*, vol. 7, no. 11, pp. 699–712, 2012, doi: 10.1038/nnano.2012.193.
- [161] K. F. Mak and J. Shan, “Photonics and optoelectronics of 2D semiconductor transition metal dichalcogenides,” *Nat. Photonics*, vol. 10, no. 4, pp. 216–226, 2016, doi:  
10.1038/nphoton.2015.282.
- [162] S. Chen and G. Shi, “Two-Dimensional Materials for Halide Perovskite-Based Optoelectronic Devices,” *Adv. Mater.*, vol. 29, no. 24, pp. 1–31, 2017, doi:  
10.1002/adma.201605448.
- [163] Y. Zhang *et al.*, “Photonics and optoelectronics using nano-structured hybrid perovskite media and their optical cavities,” *Phys. Rep.*, vol. 795, pp. 1–51, 2019, doi:  
10.1016/j.physrep.2019.01.005.
- [164] H. Li *et al.*, “Two-Dimensional Metal-Halide Perovskite-based Optoelectronics: Synthesis, Structure, Properties and Applications,” *Energy Environ. Mater.*, vol. 4, no. 1, pp. 46–64, 2021, doi: 10.1002/eem2.12087.
- [165] Y. Yi, X. F. Yu, W. Zhou, J. Wang, and P. K. Chu, “Two-dimensional black phosphorus: Synthesis, modification, properties, and applications,” *Mater. Sci. Eng. R Reports*, vol. 120, pp. 1–33, 2017, doi: 10.1016/j.mser.2017.08.001.

- [166] P. C. Debnath, K. Park, and Y. W. Song, “Recent Advances in Black-Phosphorus-Based Photonics and Optoelectronics Devices,” *Small Methods*, vol. 2, no. 4, pp. 1–24, 2018, doi: 10.1002/SMTD.201700315.
- [167] Y. Zhang, J. Wu, M. Aagesen, and H. Liu, “III-V nanowires and nanowire optoelectronic devices,” *J. Phys. D: Appl. Phys.*, vol. 48, no. 46, 2015, doi: 10.1088/0022-3727/48/46/463001.
- [168] L. N. Quan, J. Kang, C. Z. Ning, and P. Yang, “Nanowires for Photonics,” *Chem. Rev.*, vol. 119, no. 15, pp. 9153–9169, 2019, doi: 10.1021/acs.chemrev.9b00240.
- [169] S. L. Choon *et al.*, “New potential materials in advancement of photovoltaic and optoelectronic applications: Metal halide perovskite nanorods,” *Renew. Sustain. Energy Rev.*, vol. 171, no. June 2022, 2023, doi: 10.1016/j.rser.2022.113037.
- [170] S. Nanot, E. H. Hároz, J. H. Kim, R. H. Hauge, and J. Kono, “Optoelectronic properties of single-wall carbon nanotubes,” *Adv. Mater.*, vol. 24, no. 36, pp. 4977–4994, 2012, doi: 10.1002/adma.201201751.
- [171] S. Aftab, M. Z. Iqbal, and Y. S. Rim, “Recent Advances in Rolling 2D TMDs Nanosheets into 1D TMDs Nanotubes/Nanoscrolls,” *Small*, vol. 19, no. 1, 2023, doi: 10.1002/sml.202205418.
- [172] A. P. Litvin, X. Zhang, E. V. Ushakova, and A. L. Rogach, “Carbon Nanoparticles as Versatile Auxiliary Components of Perovskite-Based Optoelectronic Devices,” *Adv. Funct. Mater.*, vol. 31, no. 18, 2021, doi: 10.1002/adfm.202010768.
- [173] J. Y. Kim, O. Voznyy, D. Zhitomirsky, and E. H. Sargent, “25th anniversary article: Colloidal quantum dot materials and devices: A quarter-century of advances,” *Adv. Mater.*, vol. 25, no. 36, pp. 4986–5010, 2013, doi: 10.1002/adma.201301947.

- [174] D. Ghosh, K. Sarkar, P. Devi, K. H. Kim, and P. Kumar, “Current and future perspectives of carbon and graphene quantum dots: From synthesis to strategy for building optoelectronic and energy devices,” *Renew. Sustain. Energy Rev.*, vol. 135, no. October 2020, p. 110391, 2021, doi: 10.1016/j.rser.2020.110391.
- [175] S. Miao and Y. Cho, “Toward Green Optoelectronics: Environmental-Friendly Colloidal Quantum Dots Photodetectors,” *Front. Energy Res.*, vol. 9, no. June, pp. 1–18, 2021, doi: 10.3389/fenrg.2021.666534.
- [176] L. Li, G. Wu, G. Yang, J. Peng, J. Zhao, and J. J. Zhu, “Focusing on luminescent graphene quantum dots: Current status and future perspectives,” *Nanoscale*, vol. 5, no. 10, pp. 4015–4039, 2013, doi: 10.1039/c3nr33849e.
- [177] D. K. Hwang *et al.*, “Ultrasensitive PbS quantum-dot-sensitized InGaZnO hybrid photoinverter for near-infrared detection and imaging with high photogain,” *NPG Asia Mater.*, vol. 8, no. 1, 2016, doi: 10.1038/am.2015.137.
- [178] J. Kim *et al.*, “A skin-like two-dimensionally pixelized full-color quantum dot photodetector,” *Sci. Adv.*, vol. 5, no. 11, 2019, doi: 10.1126/sciadv.aax8801.
- [179] J. Kim *et al.*, “Vertically Stacked Full Color Quantum Dots Phototransistor Arrays for High-Resolution and Enhanced Color-Selective Imaging,” *Adv. Mater.*, vol. 34, no. 2, pp. 1–9, 2022, doi: 10.1002/adma.202106215.
- [180] A. Escudero *et al.*, “Molecular bottom-up approaches for the synthesis of inorganic and hybrid nanostructures,” *Inorganics*, vol. 9, no. 7, 2021, doi: 10.3390/inorganics9070058.
- [181] C. P. Raptopoulou, “Metal-organic frameworks: Synthetic methods and potential applications,” *Materials (Basel)*, vol. 14, no. 2, pp. 1–32, 2021, doi: 10.3390/ma14020310.

- [182] M. Rubio-Martinez, C. Avci-Camur, A. W. Thornton, I. Imaz, D. Maspoch, and M. R. Hill, "New synthetic routes towards MOF production at scale," *Chem. Soc. Rev.*, vol. 46, no. 11, pp. 3453–3480, 2017, doi: 10.1039/c7cs00109f.
- [183] M. Safaei, M. M. Foroughi, N. Ebrahimpour, S. Jahani, A. Omid, and M. Khatami, "A review on metal-organic frameworks: Synthesis and applications," *TrAC - Trends Anal. Chem.*, vol. 118, pp. 401–425, 2019, doi: 10.1016/j.trac.2019.06.007.
- [184] N. A. Khan and S. H. Jung, "Synthesis of metal-organic frameworks (MOFs) with microwave or ultrasound: Rapid reaction, phase-selectivity, and size reduction," *Coord. Chem. Rev.*, vol. 285, pp. 11–23, 2015, doi: 10.1016/j.ccr.2014.10.008.
- [185] T. Friščić, "Metal-Organic Frameworks: Mechanochemical Synthesis Strategies," *Encycl. Inorg. Bioinorg. Chem.*, pp. 1–19, 2014, doi: 10.1002/9781119951438.eibc2202.
- [186] Z. Liu, J. Zhu, C. Peng, T. Wakihara, and T. Okubo, "Continuous flow synthesis of ordered porous materials: From zeolites to metal-organic frameworks and mesoporous silica," *React. Chem. Eng.*, vol. 4, no. 10, pp. 1699–1720, 2019, doi: 10.1039/c9re00142e.
- [187] H. Y. Cho, J. Kim, S. N. Kim, and W. S. Ahn, "High yield 1-L scale synthesis of ZIF-8 via a sonochemical route," *Microporous Mesoporous Mater.*, vol. 169, pp. 180–184, 2013, doi: 10.1016/j.micromeso.2012.11.012.
- [188] B. Seoane, J. M. Zamaro, C. Tellez, and J. Coronas, "Sonocrystallization of zeolitic imidazolate frameworks (ZIF-7, ZIF-8, ZIF-11 and ZIF-20)," *CrystEngComm*, vol. 14, no. 9, pp. 3103–3107, 2012, doi: 10.1039/c2ce06382d.
- [189] X. Huang, X. Qi, F. Boey, and H. Zhang, "Graphene-based composites," *Chem. Soc. Rev.*, vol. 41, no. 2, pp. 666–686, 2012, doi: 10.1039/c1cs15078b.
- [190] V. Singh, D. Joung, L. Zhai, S. Das, S. I. Khondaker, and S. Seal, "Graphene based

- materials: Past, present and future,” *Prog. Mater. Sci.*, vol. 56, no. 8, pp. 1178–1271, 2011, doi: 10.1016/j.pmatsci.2011.03.003.
- [191] N. Zhao *et al.*, “Hierarchical porous carbon with graphitic structure synthesized by a water soluble template method,” *Mater. Lett.*, vol. 87, pp. 77–79, 2012, doi: 10.1016/j.matlet.2012.07.085.
- [192] X. W. Liu, T. J. Sun, J. L. Hu, and S. D. Wang, “Composites of metal-organic frameworks and carbon-based materials: Preparations, functionalities and applications,” *J. Mater. Chem. A*, vol. 4, no. 10, pp. 3584–3616, 2016, doi: 10.1039/c5ta09924b.
- [193] C. Petit and T. J. Bandoz, “Engineering the surface of a new class of adsorbents: Metal-organic framework/graphite oxide composites,” *J. Colloid Interface Sci.*, vol. 447, pp. 139–151, 2015, doi: 10.1016/j.jcis.2014.08.026.
- [194] L. Ge, L. Wang, V. Rudolph, and Z. Zhu, “Hierarchically structured metal-organic framework/vertically-aligned carbon nanotubes hybrids for CO<sub>2</sub> capture,” *RSC Adv.*, vol. 3, no. 47, pp. 25360–25366, 2013, doi: 10.1039/c3ra44250k.
- [195] Y. Yang, L. Ge, V. Rudolph, and Z. Zhu, “In situ synthesis of zeolitic imidazolate frameworks/carbon nanotube composites with enhanced CO<sub>2</sub> adsorption,” *Dalt. Trans.*, vol. 43, no. 19, pp. 7028–7036, 2014, doi: 10.1039/c3dt53191k.
- [196] N. Stock and S. Biswas, “Synthesis of metal-organic frameworks (MOFs): Routes to various MOF topologies, morphologies, and composites,” *Chem. Rev.*, vol. 112, no. 2, pp. 933–969, 2012, doi: 10.1021/cr200304e.
- [197] M. C. McCarthy, V. Varela-Guerrero, G. V. Barnett, and H. K. Jeong, “Synthesis of zeolitic imidazolate framework films and membranes with controlled microstructures,” *Langmuir*, vol. 26, no. 18, pp. 14636–14641, 2010, doi: 10.1021/la102409e.

- [198] J. Yao, D. Dong, D. Li, L. He, G. Xu, and H. Wang, “Contra-diffusion synthesis of ZIF-8 films on a polymer substrate,” *Chem. Commun.*, vol. 47, no. 9, pp. 2559–2561, 2011, doi: 10.1039/c0cc04734a.
- [199] G. Lu and J. T. Hupp, “Metal-organic frameworks as sensors: A ZIF-8 based fabry-pérot device as a selective sensor for chemical vapors and gases,” *J. Am. Chem. Soc.*, vol. 132, no. 23, pp. 7832–7833, 2010, doi: 10.1021/ja101415b.
- [200] N. Chang, Z. Y. Gu, and X. P. Yan, “Zeolitic imidazolate framework-8 nanocrystal coated capillary for molecular sieving of branched alkanes from linear alkanes along with high-resolution chromatographic separation of linear alkanes,” *J. Am. Chem. Soc.*, vol. 132, no. 39, pp. 13645–13647, 2010, doi: 10.1021/ja1058229.
- [201] A. Demessence *et al.*, “Adsorption properties in high optical quality nanoZIF-8 thin films with tunable thickness,” *J. Mater. Chem.*, vol. 20, no. 36, pp. 7676–7681, 2010, doi: 10.1039/c0jm00500b.
- [202] J. M. Schnorr and T. M. Swager, “Emerging applications of carbon nanotubes,” *Chem. Mater.*, vol. 23, no. 3, pp. 646–657, 2011, doi: 10.1021/cm102406h.
- [203] M. G. Campbell and M. Dincă, “Metal–organic frameworks as active materials in electronic sensor devices,” *Sensors (Switzerland)*, vol. 17, no. 5, pp. 1–11, 2017, doi: 10.3390/s17051108.
- [204] D. Sheberla, L. Sun, M. A. Blood-forsythe, S. Er, C. R. Wade, and C. K. Brozek, “Department of Chemistry, Massachusetts Institute of Technology, Cambridge, Massachusetts 02139, United States Department of Chemistry and Chemical Biology, Harvard University, Cambridge, Massachusetts 02138, United States,” *J. Am. Chem. Soc.*, vol. 3, pp. 2–5, 2014.

- [205] M. G. Campbell, S. F. Liu, T. M. Swager, and M. Dincă, “Chemiresistive Sensor Arrays from Conductive 2D Metal-Organic Frameworks,” *J. Am. Chem. Soc.*, vol. 137, no. 43, pp. 13780–13783, 2015, doi: 10.1021/jacs.5b09600.
- [206] M. K. Smith, K. E. Jensen, P. A. Pivak, and K. A. Mirica, “Direct Self-Assembly of Conductive Nanorods of Metal-Organic Frameworks into Chemiresistive Devices on Shrinkable Polymer Films,” *Chem. Mater.*, vol. 28, no. 15, pp. 5264–5268, 2016, doi: 10.1021/acs.chemmater.6b02528.
- [207] F. Yao, P. Gui, Q. Zhang, and Q. Lin, “Molecular engineering of perovskite photodetectors: Recent advances in materials and devices,” *Mol. Syst. Des. Eng.*, vol. 3, no. 5, pp. 702–716, 2018, doi: 10.1039/c8me00022k.
- [208] K. W.A. Chee, “Introductory Chapter: Photodetectors,” in *Advances in Photodetectors - Research and Applications*, IntechOpen, 2019, pp. 3–8.
- [209] A. Pan and X. Zhu, “Optoelectronic properties of semiconductor nanowires,” in *Semiconductor Nanowires*, Elsevier, 2015, pp. 327–363.
- [210] R. Kumar and S. K. Mishra, “Luminescence and photodetection characteristics of rare earth-doped zinc oxide nanostructures,” in *Ceramic Science and Engineering*, Elsevier, 2022, pp. 263–294.
- [211] R. Srivastava, “Investigation on Temperature Sensing of Nanostructured Zinc Oxide Synthesized via Oxalate Route,” *J. Sens. Technol.*, vol. 02, no. 01, pp. 8–12, 2012, doi: 10.4236/jst.2012.21002.
- [212] P. Arabkhani, H. Javadian, A. Asfaram, and M. Ateia, “Decorating graphene oxide with zeolitic imidazolate framework (ZIF-8) and pseudo-boehmite offers ultra-high adsorption capacity of diclofenac in hospital effluents,” *Chemosphere*, vol. 271, p. 129610, 2021, doi:

- 10.1016/j.chemosphere.2021.129610.
- [213] Y. Zhang, Y. Jia, and L. Hou, "Synthesis of zeolitic imidazolate framework-8 on polyester fiber for PM2.5 removal," *RSC Adv.*, vol. 8, no. 55, pp. 31471–31477, 2018, doi: 10.1039/c8ra06414h.
- [214] S. Rawi, M. Amin, E. Kusriani, and N. Putra, "Characterization of shape-stabilized phase change material using beeswax and functionalized multi-walled carbon nanotubes," *IOP Conf. Ser. Earth Environ. Sci.*, vol. 105, no. 1, pp. 0–6, 2018, doi: 10.1088/1755-1315/105/1/012042.
- [215] V. H. Nguyen and J. J. Shim, "Green synthesis and characterization of carbon nanotubes/polyaniline nanocomposites," *J. Spectrosc.*, vol. 2015, no. April, 2015, doi: 10.1155/2015/297804.
- [216] R. Wang, J. Yue, R. Li, and Y. Sun, "Evaluation of Aging Resistance of Asphalt Binder Modified with Graphene Oxide and Carbon Nanotubes," *J. Mater. Civ. Eng.*, vol. 31, no. 11, p. 04019274, 2019, doi: 10.1061/(asce)mt.1943-5533.0002934.
- [217] S. Tanaka *et al.*, "Adsorption and Diffusion Phenomena in Crystal Size Engineered ZIF-8 MOF," *J. Phys. Chem. C*, vol. 119, no. 51, pp. 28430–28439, 2015, doi: 10.1021/acs.jpcc.5b09520.
- [218] J. Li *et al.*, "Synthesis and adsorption performance of La@ZIF-8 composite metal-organic frameworks," *RSC Adv.*, vol. 10, no. 6, pp. 3380–3390, 2020, doi: 10.1039/c9ra10548d.
- [219] A. Awadallah-F, F. Hillman, S. A. Al-Muhtaseb, and H. K. Jeong, "On the nanogate-opening pressures of copper-doped zeolitic imidazolate framework ZIF-8 for the adsorption of propane, propylene, isobutane, and n-butane," *J. Mater. Sci.*, vol. 54, no. 7, pp. 5513–5527, 2019, doi: 10.1007/s10853-018-03249-y.

- [220] H. Sun *et al.*, “Tuning n-Alkane Adsorption on Mixed-Linker Zeolitic Imidazolate Framework-8-90 via Controllable Ligand Hybridization: Insight into the Confinement from an Energetics Perspective,” *Ind. Eng. Chem. Res.*, vol. 58, no. 29, pp. 13274–13283, 2019, doi: 10.1021/acs.iecr.9b00941.
- [221] J. Mao *et al.*, “Constructing multifunctional MOF@rGO hydro-/aerogels by the self-assembly process for customized water remediation,” *J. Mater. Chem. A*, vol. 5, no. 23, pp. 11873–11881, 2017, doi: 10.1039/c7ta01343d.
- [222] M. K. Trivedi, A. B. Dahryn Trivedi, and G. N. Gunin Saikia, “Physical and Structural Characterization of Biofield Treated Imidazole Derivatives,” *Nat. Prod. Chem. Res.*, vol. 3, no. 5, pp. 2329–6836, 2015, doi: 10.4172/2329-6836.1000187.
- [223] T. Kavinkumar and S. Manivannan, “Synthesis, Characterization and Gas Sensing Properties of Graphene Oxide-Multiwalled Carbon Nanotube Composite,” *J. Mater. Sci. Technol.*, vol. 32, no. 7, pp. 626–632, 2016, doi: 10.1016/j.jmst.2016.03.017.
- [224] K. S. W. SING *et al.*, “Reporting Physisorption Data for Gas/Solid Systems with Special Reference to the Determination of Surface Area and Porosity (Recommendations 1984),” *Pure Appl. Chem.*, vol. 57, no. 24, pp. 603–619, 1985, doi: 10.1002/pola.26338.
- [225] C. E. Giusca, Y. Tison, and S. R. P. Silva, “Evidence for metal-semiconductor transitions in twisted and collapsed double-walled carbon nanotubes by scanning tunneling microscopy,” *Nano Lett.*, vol. 8, no. 10, pp. 3350–3356, 2008, doi: 10.1021/nl801782k.
- [226] J. González-Julián *et al.*, “Multi-scale electrical response of silicon nitride/multi-walled carbon nanotubes composites,” *Compos. Sci. Technol.*, vol. 71, no. 1, pp. 60–66, 2011, doi: 10.1016/j.compscitech.2010.10.004.
- [227] A. Peyvandi, P. Soroushian, N. Abdol, and A. M. Balachandra, “Surface-modified

- graphite nanomaterials for improved reinforcement efficiency in cementitious paste,” *Carbon N. Y.*, vol. 63, pp. 175–186, 2013, doi: 10.1016/j.carbon.2013.06.069.
- [228] C. C. Luhrs, M. Moberg, A. Maxson, L. Brewer, and S. Menon, “IF-WS<sub>2</sub>/nanostructured carbon hybrids generation and their characterization,” *Inorganics*, vol. 2, no. 2, pp. 211–232, 2014, doi: 10.3390/inorganics2020211.
- [229] M. Kotal, A. K. Thakur, and A. K. Bhowmick, “Polyaniline-carbon nanofiber composite by a chemical grafting approach and its supercapacitor application,” *ACS Appl. Mater. Interfaces*, vol. 5, no. 17, pp. 8374–8386, 2013, doi: 10.1021/am4014049.
- [230] R. A. Senthil, A. Selvi, P. Arunachalam, L. S. Amudha, J. Madhavan, and A. M. Al-Mayouf, “A sensitive electrochemical detection of hydroquinone using newly synthesized  $\alpha$ -Fe<sub>2</sub>O<sub>3</sub>-graphene oxide nanocomposite as an electrode material,” *J. Mater. Sci. Mater. Electron.*, vol. 28, no. 14, pp. 10081–10091, 2017, doi: 10.1007/s10854-017-6769-x.
- [231] Y. Yodi, I. W. K. Suryawan, and A. S. Afifah, “Estimation of Green House Gas (GHG) emission at Telaga Punggur landfill using triangular, LandGEM, and IPCC methods,” *J. Phys. Conf. Ser.*, vol. 1456, no. 1, p. 012001, 2020, doi: 10.1088/1742-6596/1456/1/012001.
- [232] W. Eugster and G. W. Kling, “Performance of a low-cost methane sensor for ambient concentration measurements in preliminary studies,” *Atmos. Meas. Tech.*, vol. 5, no. 8, pp. 1925–1934, 2012, doi: 10.5194/amt-5-1925-2012.
- [233] J. Norooz Oliiae *et al.*, “Development of a Sub-ppb Resolution Methane Sensor Using a GaSb-Based DFB Diode Laser near 3270 nm for Fugitive Emission Measurement,” *ACS Sensors*, vol. 7, no. 2, pp. 564–572, 2022, doi: 10.1021/acssensors.1c02444.
- [234] X. Liu, J. Yang, T. Ye, and Z. Han, “Establishment of analysis method for methane

- detection by gas chromatography,” *IOP Conf. Ser. Earth Environ. Sci.*, vol. 113, no. 1, p. 012023, 2018, doi: 10.1088/1755-1315/113/1/012023.
- [235] L. M. Dorojkine, “The non-catalytic thermal wave-based chemical gas sensor for methane and natural gas,” *Sensors Actuators, B Chem.*, vol. 89, no. 1–2, pp. 76–85, 2003, doi: 10.1016/S0925-4005(02)00431-8.
- [236] O. Abuzalat, D. Wong, M. Elsayed, S. Park, and S. Kim, “Sonochemical fabrication of Cu(II) and Zn(II) metal-organic framework films on metal substrates,” *Ultrason. Sonochem.*, vol. 45, no. December 2017, pp. 180–188, 2018, doi: 10.1016/j.ultsonch.2018.03.012.
- [237] T. Düren, L. Sarkisov, O. M. Yaghi, and R. Q. Snurr, “Design of new materials for methane storage,” *Langmuir*, vol. 20, no. 7, pp. 2683–2689, 2004, doi: 10.1021/la0355500.
- [238] N. Bârsan and U. Weimar, “Understanding the fundamental principles of metal oxide based gas sensors; the example of CO sensing with SnO<sub>2</sub> sensors in the presence of humidity,” *J. Phys. Condens. Matter*, vol. 15, no. 20, p. 8984, 2003, doi: 10.1088/0953-8984/15/20/201.
- [239] A. D. Smith *et al.*, “Graphene-based CO<sub>2</sub> sensing and its cross-sensitivity with humidity,” *RSC Adv.*, vol. 7, no. 36, pp. 22329–22339, 2017, doi: 10.1039/c7ra02821k.
- [240] J. Zhao, A. Buldum, J. Han, and J. P. Lu, “Gas molecule adsorption in carbon nanotubes and nanotube bundles,” *Nanotechnology*, vol. 13, no. 2, pp. 195–200, 2002, doi: 10.1088/0957-4484/13/2/312.
- [241] E. Contes-de Jesus *et al.*, “Platinum Electrodeposition on Unsupported Single Wall Carbon Nanotubes and Its Application as Methane Sensing Material,” *J. Electrochem.*

- Soc.*, vol. 160, no. 2, pp. H98–H104, 2013, doi: 10.1149/2.054302jes.
- [242] Z. Huang *et al.*, “Stable core – shell ZIF - 8 @ ZIF - 67 MOFs photocatalyst for highly efficient degradation of organic pollutant and hydrogen evolution,” *J. Mater. Res.*, vol. 36, no. 3, pp. 602–614, 2021, doi: 10.1557/s43578-021-00117-5.
- [243] K. T. Butler, C. H. Hendon, and A. Walsh, “Designing porous electronic thin-film devices: Band offsets and heteroepitaxy,” *Faraday Discuss.*, vol. 201, pp. 207–219, 2017, doi: 10.1039/c7fd00019g.
- [244] D. Shi, Z. Guo, and N. Bedford, *Nanomaterials and devices*. Elsevier, 2015.
- [245] K. Babooram, “Brief overview of polymer science,” in *Polymer Science and Nanotechnology*, E. Payne, Ed. Elsevier, 2020, pp. 3–12.
- [246] WHO Regional Office for Europe, “Chapter 5.5 Carbon monoxide,” *Air Qual. Guidel. - Second Ed.*, vol. 22, no. 8, pp. 1–15, Dec. 2000.
- [247] A. Esplugues *et al.*, “Indoor and outdoor concentrations and determinants of NO<sub>2</sub> in a cohort of 1-year-old children in Valencia, Spain,” *Indoor Air*, vol. 20, no. 3, pp. 213–223, 2010, doi: 10.1111/j.1600-0668.2010.00646.x.
- [248] W. E. Luttrell, “Nitrogen dioxide,” *J. Chem. Heal. Saf.*, vol. 21, no. 2, pp. 28–30, 2014, doi: 10.1016/j.jchas.2014.01.008.
- [249] L. Ampollini *et al.*, “Observations and Contributions of Real-Time Indoor Ammonia Concentrations during HOMEChem,” *Environ. Sci. Technol.*, vol. 53, no. 15, pp. 8591–8598, 2019, doi: 10.1021/acs.est.9b02157.
- [250] A. Sekar, G. K. Varghese, and M. K. Ravi Varma, “Analysis of benzene air quality standards, monitoring methods and concentrations in indoor and outdoor environment,” *Heliyon*, vol. 5, no. 11, p. e02918, 2019, doi: 10.1016/j.heliyon.2019.e02918.

- [251] WHO Regional Office for Europe, “Chapter 5.2 Benzene,” *Air Qual. Guidel. - Second Ed.*, vol. 3, no. 4, pp. 1–18, 2000, [Online]. Available:  
<http://scholar.google.com/scholar?hl=en&btnG=Search&q=intitle:Chapter+5.2#8>.
- [252] World Health Organization (WHO), “WHO - Toluene: Air quality guidelines,” *Air Qual. Guidel. - Second Ed.*, vol. 2, no. 7, pp. 1–20, 2000.
- [253] H. J. Kim and J. H. Lee, “Highly sensitive and selective gas sensors using p-type oxide semiconductors: Overview,” *Sensors Actuators, B Chem.*, vol. 192, pp. 607–627, 2014, doi: 10.1016/j.snb.2013.11.005.
- [254] H. Zhang and R. Q. Snurr, “Computational Study of Water Adsorption in the Hydrophobic Metal–Organic Framework ZIF-8: Adsorption Mechanism and Acceleration of the Simulations,” *J. Phys. Chem. C*, vol. 121, pp. 24000–24010, 2017, doi: 10.1021/acs.jpcc.7b06405.
- [255] L. A. Currie, “INTERNATIONAL UNION OF PURE NOMENCLATURE IN EVALUATION OF ANALYTICAL METHODS INCLUDING DETECTION Nomenclature in evaluation of analytical methods , including detect ion and quantification ca pa bi I it ies ’ ( IUPAC Recommendations 1995 ),” *Pure & Appl. Chem.*, vol. 67, no. 10, pp. 1699–1723, 1995.
- [256] J. G. Calvert, “INTERNATIONAL UNION OF PURE COMMISSION ON ATMOSPHERIC CHEMISTRY \* GLOSSARY OF,” *Pure & Appl. Chem*, vol. 62, no. 11, pp. 2167–2219, 1990.
- [257] X. Chong *et al.*, “Surface-Enhanced Infrared Absorption: Pushing the Frontier for On-Chip Gas Sensing,” *ACS Sensors*, vol. 3, no. 1, pp. 230–238, 2018, doi: 10.1021/acssensors.7b00891.

- [258] W. Dang *et al.*, “Methane adsorption rate and diffusion characteristics in marine shale samples from Yangtze Platform, South China,” *Energies*, vol. 10, no. 5, p. 626, 2017, doi: 10.3390/en10050626.
- [259] F. Coudert, “Molecular Mechanism of Swing Effect in Zeolitic Imidazolate Framework ZIF-8 : Continuous Deformation upon Adsorption,” *ChemPhysChem*, vol. 19, pp. 2732–2738, 2017, doi: 10.1002/cphc.201700463.
- [260] L. Zhang, G. Wu, and J. Jiang, “Adsorption and Diffusion of CO<sub>2</sub> and CH<sub>4</sub> in Zeolitic Imidazolate Framework-8 : Effect of Structural Flexibility,” *J. Phys. Chem. C*, vol. 118, p. 8788–8794, 2014.
- [261] D. Liu, Y. Wu, Q. Xia, and Z. Li, “Experimental and molecular simulation studies of CO<sub>2</sub> adsorption on zeolitic imidazolate frameworks : ZIF-8 and amine-modified ZIF-8,” *Adsorption*, vol. 19, pp. 25–37, 2013, doi: 10.1007/s10450-012-9407-1.
- [262] J. Canivet, J. Bonnefoy, C. Daniel, A. Legrand, B. Coasne, and D. Farrusseng, “Structure–property relationships of water adsorption in metal–organic frameworks,” *New J. Chem.*, vol. 38, no. June, p. 3102, 2014, doi: 10.1039/C4NJ00076E.
- [263] K. Zhang, R. P. Lively, C. Zhang, W. J. Koros, and R. R. Chance, “Investigating the Intrinsic Ethanol / Water Separation Capability of ZIF-8 : An Adsorption and Diffusion Study,” *J. Phys. Chem. C 2013*, vol. 117, p. 7214–7225, 2013, [Online]. Available: [dx.doi.org/10.1021/jp401548b](https://doi.org/10.1021/jp401548b).
- [264] M. Saharay and S. Balasubramanian, “Electron Donor - Acceptor Interactions in Ethanol - CO<sub>2</sub> Mixtures : An Ab Initio Molecular Dynamics Study of Supercritical Carbon Dioxide †,” *J. Phys. Chem. B*, vol. 110, pp. 3782–3790, 2006, [Online]. Available: [10.1021/jp053839f](https://doi.org/10.1021/jp053839f) CCC.

- [265] K. Zhang *et al.*, “Alcohol and water adsorption in zeolitic imidazolate frameworks,” *Chem. Commun.*, vol. 49, pp. 3245–3247, 2013, doi: 10.1039/c3cc39116g.
- [266] V. R. Naganaboina, M. Anandkumar, A. S. Deshpande, and S. G. Singh, “Single-phase high-entropy oxide-based chemiresistor: Toward selective and sensitive detection of methane gas for real-time applications,” *Sensors Actuators B Chem.*, vol. 357, no. January, p. 131426, 2022, doi: 10.1016/j.snb.2022.131426.
- [267] P. Shukla, P. Saxena, D. Madhwal, N. Bhardwaj, and V. K. Jain, “Electrostatically functionalized CVD grown multiwalled carbon nanotube/ palladium polymer nanocomposite (MWCNT/Pd) for methane detection at room temperature,” *Chem. Eng. Sci.*, vol. 264, p. 118191, 2022, doi: 10.1016/j.ces.2022.118191.
- [268] M. J. Bezdek, S. X. L. Luo, K. H. Ku, and T. M. Swager, “A chemiresistive methane sensor,” *Proc. Natl. Acad. Sci. U. S. A.*, vol. 118, no. 2, pp. 1–6, 2021, doi: 10.1073/pnas.2022515118.
- [269] D. Tests and F. O. R. Diabetes, “2. Classification and diagnosis of diabetes,” *Diabetes Care*, vol. 38, no. January, pp. S8–S16, 2015, doi: 10.2337/dc15-S005.
- [270] M. Righettoni, A. Tricoli, S. Gass, A. Schmid, A. Amann, and S. E. Pratsinis, “Breath acetone monitoring by portable Si:WO<sub>3</sub> gas sensors,” *Anal. Chim. Acta*, vol. 738, pp. 69–75, 2012, doi: 10.1016/j.aca.2012.06.002.
- [271] S. Salehi, E. Nikan, A. A. Khodadadi, and Y. Mortazavi, “Highly sensitive carbon nanotubes-SnO<sub>2</sub> nanocomposite sensor for acetone detection in diabetes mellitus breath,” *Sensors Actuators, B Chem.*, vol. 205, pp. 261–267, 2014, doi: 10.1016/j.snb.2014.08.082.
- [272] J. D. Fenske and S. E. Paulson, “Human breath emissions of VOCs,” *J. Air Waste Manag. Assoc.*, vol. 49, no. 5, pp. 594–598, 1999, doi: 10.1080/10473289.1999.10463831.

- [273] C. P. Weisel, “Benzene exposure: An overview of monitoring methods and their findings,” *Chem. Biol. Interact.*, vol. 184, no. 1–2, pp. 58–66, 2010, doi: 10.1016/j.cbi.2009.12.030.
- [274] E. Mansour *et al.*, “Measurement of temperature and relative humidity in exhaled breath,” *Sensors Actuators, B Chem.*, vol. 304, no. September 2019, p. 127371, 2020, doi: 10.1016/j.snb.2019.127371.
- [275] J. Cousinsaintremi *et al.*, “Biobutanol separation with the metal-organic framework ZIF-8,” *ChemSusChem*, vol. 4, no. 8, pp. 1074–1077, 2011, doi: 10.1002/cssc.201100261.
- [276] C. Yim *et al.*, “Adsorption and desorption characteristics of alcohol vapors on a nanoporous ZIF-8 film investigated using silicon microcantilevers,” *Chem. Commun.*, vol. 51, no. 28, pp. 6168–6171, 2015, doi: 10.1039/c5cc01315a.
- [277] M. Tu, S. Wannapaiboon, K. Khaletskaya, and R. A. Fischer, “Engineering Zeolitic-Imidazolate Framework (ZIF) Thin Film Devices for Selective Detection of Volatile Organic Compounds,” *Adv. Funct. Mater.*, vol. 25, no. 28, pp. 4470–4479, 2015, doi: 10.1002/adfm.201500760.
- [278] J. H. Ping Sun, Yadong Jiang, Guangzhong Xie, Junsheng Yu, Xiaosong Du, “Synthesis and Sensitive Properties of Poly- (bistriethylphosphine)-platinum-diethynylbenzene for Organic Vapor Detection,” *J. Appl. Polym. Sci.*, vol. 116, no. 5, pp. 562–567, 2010, doi: 10.1002/app.31506.
- [279] L. Xu, X. Hu, Y. Tze Lim, and V. S. Subramanian, “Organic vapor adsorption behavior of poly(3-butoxythiophene) LB films on quartz crystal microbalance,” *Thin Solid Films*, vol. 417, no. 1–2, pp. 90–94, 2002, doi: 10.1016/S0040-6090(02)00634-X.
- [280] E. Haghghi and S. Zeinali, “Nanoporous MIL-101(Cr) as a sensing layer coated on a

- quartz crystal microbalance (QCM) nanosensor to detect volatile organic compounds (VOCs),” *RSC Adv.*, vol. 9, no. 42, pp. 24460–24470, 2019, doi: 10.1039/c9ra04152d.
- [281] K. Zhang, R. P. Lively, C. Zhang, W. J. Koros, and R. R. Chance, “Investigating the intrinsic ethanol/water separation capability of ZIF-8: An adsorption and diffusion study,” *J. Phys. Chem. C*, vol. 117, no. 14, pp. 7214–7225, 2013, doi: 10.1021/jp401548b.
- [282] S. A. Hakim, Y. Liu, G. S. Zakharova, and W. Chen, “Synthesis of vanadium pentoxide nanoneedles by physical vapour deposition and their highly sensitive behavior towards acetone at room temperature,” *RSC Adv.*, vol. 5, no. 30, pp. 23489–23497, 2015, doi: 10.1039/c4ra16564k.
- [283] S. Shao *et al.*, “Highly crystalline and ordered nanoporous SnO<sub>2</sub> thin films with enhanced acetone sensing property at room temperature,” *J. Mater. Chem. C*, vol. 3, no. 41, pp. 10819–10829, 2015, doi: 10.1039/c5tc02188j.
- [284] D. Zhang, A. Liu, H. Chang, and B. Xia, “Room-temperature high-performance acetone gas sensor based on hydrothermal synthesized SnO<sub>2</sub>-reduced graphene oxide hybrid composite,” *RSC Adv.*, vol. 5, no. 4, pp. 3016–3022, 2015, doi: 10.1039/c4ra10942b.
- [285] B. Bhowmik, A. Hazra, K. Dutta, and P. Bhattacharyya, “Repeatability and stability of room-temperature acetone sensor based on TiO<sub>2</sub> nanotubes: Influence of stoichiometry variation,” *IEEE Trans. Device Mater. Reliab.*, vol. 14, no. 4, pp. 961–967, 2014, doi: 10.1109/TDMR.2014.2347376.
- [286] H. Ahn, Y. Wang, S. Hyun Jee, M. Park, Y. S. Yoon, and D. J. Kim, “Enhanced UV activation of electrochemically doped Ni in ZnO nanorods for room temperature acetone sensing,” *Chem. Phys. Lett.*, vol. 511, no. 4–6, pp. 331–335, 2011, doi: 10.1016/j.cplett.2011.06.045.

- [287] R. Jaisutti *et al.*, “Ultrasensitive Room-Temperature Operable Gas Sensors Using p-Type Na:ZnO Nanoflowers for Diabetes Detection,” *ACS Appl. Mater. Interfaces*, vol. 9, no. 10, pp. 8796–8804, 2017, doi: 10.1021/acsami.7b00673.
- [288] J. Liang, R. Yang, K. Zhu, and M. Hu, “Room temperature acetone-sensing properties of branch-like VO<sub>2</sub> (B)@ZnO hierarchical hetero-nanostructures,” *J. Mater. Sci. Mater. Electron.*, vol. 29, no. 5, pp. 3780–3789, 2018, doi: 10.1007/s10854-017-8313-4.
- [289] L. Liao *et al.*, “The characterization and application of p-type semiconducting mesoporous carbon nanofibers,” *Carbon N. Y.*, vol. 47, no. 7, pp. 1841–1845, 2009, doi: 10.1016/j.carbon.2009.03.029.
- [290] Y. Zhao, D. Jiang, and M. Zhao, “A spectrally selective self-powered photodetector utilizing a ZnO/Cu<sub>2</sub>O heterojunction,” *Appl. Surf. Sci.*, vol. 636, no. May, p. 157800, 2023, doi: 10.1016/j.apsusc.2023.157800.